DESIGNING ADVANCED LITHIUM-ION BATTERIES WITH NOVEL ARCHITECTURE, AND HIGH-PERFORMANCE CELL ELEMENTS WITH ENHANCED THERMAL SAFETY ASPECTS

by

Mihit Hitendra Parekh

A Dissertation

Submitted to the Faculty of Purdue University

In Partial Fulfillment of the Requirements for the degree of

Doctor of Philosophy

Davidson School of Chemical Engineering

West Lafayette, Indiana

December 2021

THE PURDUE UNIVERSITY GRADUATE SCHOOL

STATEMENT OF COMMITTEE APPROVAL

Dr. Vilas G. Pol, Chair

Davidson School of Chemical Engineering

Dr. Jeffery T. Miller

Davidson School of Chemical Engineering

Dr. Jeffery Greeley

Davidson School of Chemical Engineering

Dr. Edwin R. García

School of Materials Engineering

Approved by:

Dr. John A. Morgan

Dedicated to my Family, Teachers & Friends

ACKNOWLEDGMENTS

It is rightly said that Ph.D. is not a destination to reach but a long journey to pursue. With lots of ups and downs along the path, there are wonderful souls around to guide, support, motivate, and inspire the one. This thesis is the culmination of all the encouragement and wisdom imparted to me by a great number of people. I would like to thank people whose presence made this possible.

First and foremost, I would like to express my sincere gratitude towards my Ph.D. advisor, Prof. Vilas G. Pol, for his guidance and strong support throughout the past four years. His philosophy of out-of-box thinking and looking at the big picture really motivated me to find creative solutions to a variety of problems. I am grateful to him for accepting me under his tutelage as a graduate student. Long detailed discussions with him and the freedom to pursue research topics of my interest are something I would miss. He encouraged me to stay physically and mentally fit throughout and especially during the year 2020. His emphasis on utilizing the research time effectively helped me develop and publish various novel research ideas. I hope to be as enthusiastic, energized, and lively as he is someday.

I would like to thank my Ph.D. committee members, Prof. Edwin García, Prof. Jeffery T. Miller, and Prof. Jeffery Greeley for their valuable inputs, critiques, perspectives, and suggestions. Their valuable advice was helpful to my research. I am forever grateful to Prof. Ramakrishna Doraiswamy for giving me this incredible opportunity to join the Ph.D. Program at Davidson of Chemical of Engineering and Prof. Aniruddha Pandit for recommending me to him. Over the course of the past few years, I came across excellent researchers at ViPER Laboratories who provided me with research assistance, friendship, and support. Dr. Manikandan Palanisamy, Vihang Parikh, and Deep Jokhakar have been strong pillars in my learning curve of the battery field and have enjoyed hours and hours of discussions and arguments about research with them. I would also like to thank Dr. Patrick J. Kim, Dr. Jialiang Tang, Dr. Ryan A. Adams, Dr. Kyungho Kim for the valuable knowledge and training they provided to me during my early days as a researcher at ViPER. I am thankful to Harsha Rao, Daniel Gribble, Lt. Maria Carter, Abhimanyu Shekhar, and other members of the ViPER group, who have helped contribute to my research.

I am fortunate to have worked with numerous exceptional collaborators. I would like to acknowledge and thank Prof. Haiyan Wang, Prof. Murray Thomson, Prof. Jodie Lutkenhaus, Dr. Thomas Adams, Prof. Mukherjee, and Prof. Vikas Tomar, Dr. Bing Li, Dr. Anton Sedaiko, Suyash

Oka, Dr. Shikhar Misra, and Dr. Zhimin Qi for insights into unfamiliar discipline, supporting research with dedication and positivity. Special thanks to Dr. James Fleetwood, Battery Innovation Center for his knowledge-sharing spirit and for helping me scale up my research to pouch-cells. I am also grateful to Dr. Anaba Anani for hosting me at Brightvolt Inc. to provide hands-on pouch-cell experience. Dr. Christopher Gilpin, Purdue Agriculture always aided outside work-hour times for microscopy. I am grateful to him. I am thankful to my professors back in India, Prof. Kasi Sidambaram, Prof. Amol Kulkarni, Prof. Ravi Mariwala, Prof. Anand Patwardhan, Prof. Ashwin Patwardhan, Prof. Sunil Bhagwat, and others, who encouraged me towards this research career.

This road would not have been smooth without the support of the faculty and staff of Davidson School of Chemical Engineering. I am very grateful to Beverly Johnson, Robin Waling, and Jason Thorp for their wonderful assistance. I would like to thank the staff of the ChE Business office for their help. Nick Humphrey assisted in the laboratory setup, custom device fabrication and I am grateful for his support.

During the testing periods of a Ph.D., what really matters to one is having strong and enduring friendships. With my time at Purdue, I have realized many such treasures in form of Kritika Pradhan, Abhijit Talpade, Kaustabh Sarkar, *Crestview Boys:* Ranga Rohit Seemakurthi, Dishan Shah, Dhawal Chobisa and Yash Shah, Tarun Mutukuri, Deep Jokhakar, Vihang Parikh, Harshal Jawale, Swapnil Deshmukh, Shubhanshu Agrawal, Radhakrishna Tumbalam Gooty, Ishant Khurana, Ankita Morankar, Kaustubh Sawant, Gaurav Deshmukh, Varun Sundarkumar and many others. I would like to thank my friends from the *Hybrid Electric Vehicles* course for making the classroom experience so unforgettable. All of them have made this short journey a wonderful and memorable one. We have created some of the most amazing memories of our lives that I will continue to cherish forever.

Finally, my amazing family, the most basic energy source of my life back in India, who have provided unconditional support; sacrificed, and given up a lot for me to be at Purdue; despite not being able to meet them for years, they have rejoiced and cherished all my successes and great moments. They have believed in me and encouraged me to pursue my dreams and stood by my side whenever I needed it. I will forever be indebted to them. I believe that receiving this Ph.D. has been a worthwhile experience and an idea that learning never ends!

TABLE OF CONTENTS

LIST OF TABLES

LIST OF FIGURES

ABSTRACT

To compete with traditional hydrocarbon energy sources and meet the demands of battery applications, the next generation of lithium-ion batteries (LIBs) needs to have high specific energy, high energy density, low cost, and reliable safety characteristics. To improve electrochemical characteristics without sacrificing thermal safety, a deeper understanding of the material synthesis/ fabrication, interfacial behavior, and in situ thermochemical stabilities are vital. Along with these understandings, it is essential to understand the other limitations of LIBs in terms of lifetime, economic aspects, etc. With the boom of electric vehicles, high stress is applied to extract the extra juice out of the batteries to achieve a longer mile range. For electric vehicles, there is a unique requirement of greater than 240 Wh kg^{-1} energy density and a lifetime of more than ten years to ensure economic and longer driving distances. To overcome all these challenges, further developments are required in the (de)-intercalation reactions and the geometric design of LIBs. This thesis aims to provide a thorough understanding of the various challenges of LIBs, through a comprehensive experimental approach combining electrode synthesis, separator design or modifications, battery design, sensors, advanced material characterization, and electrochemical-analytical techniques.

Silicon anodes have over ten times more theoretical capacity (3579 mAh g^{-1}) than graphite anode (372 mAh g^{-1}), however, the alloyed Si, $Li_{3.75}Si$, swells in volume by about 320% during charging, which results in anode cracking, fracturing, loss of electrical contact (delamination), unstable solid electrolyte interface (SEI), and even catastrophic cell failure. Here, a novel composite graphite-carbon-silicon (GCSi) anode material with its formation mechanism established via in situ environmental transmission electron microscopy, and through a combination of ex-situ, and in situ characterizations, and cell performance testing–a complete picture of the silicon anode behavior, advantages, and drawbacks were obtained. During thermal runaway tests, silicon composite anode with lithium cobalt oxide cathode (LCO) demonstrated slightly lower heat generation per cell energy compared to the LCO/graphite chemistry. To further evaluate and predict the thermal stability of LIBs, in situ sensing of thermal signatures using an internal resistance temperature detector (RTD) was devised with an attempt to predict the thermal runaway prior to an external sensor. Sensing the temperature beneath the anode gave direct access to the heat liberated, including SEI decomposition-related heat generation. External short circuit (ESC)

and overcharge tests were conducted to trigger the thermal runaway event, and temperatures of 36.4 ℃ and 48.4 ℃ were recorded using internal RTDs, which were 9 ℃ and 20 ℃ higher than with external RTD, respectively. Interestingly, internal RTD has detection ability for 90% temperature rise 14 times faster. Using thermal signatures from RTD, an advanced battery management system can lead to conducive LIBs.

Separators influence the transport of Li^+ ions across the electrodes, safety aspects, energy density, cycle life, and economics of the batteries. Through the use of novel aramid nanofibers and modified microporous membrane separators, high-performance LIBs and lithium-sulfur chemistry have been realized at varied critical temperatures. Finally, to address the energy and power density challenges, there is an urgent need for innovation in the design of LIBs. With the development of high-capacity anode materials, there is a requirement to develop high-capacity cathodes. Various high-capacity cathodes viz., sulfur, or V_2O_5, do not contain Li^+ ions in their atomic framework, to begin with. Various strategies like pre-lithiation, blended cathodes, lithium-additives, and film-forming additives have been proposed, however, either they are not practical or alter the cell voltage behavior. Here, we proposed a novel configuration to LIBs called Reserve Lithium-ion Batteries (RLIBs), which utilizes a reservoir electrode to supplement Li^+ ions to lithium-deficient cathodes such as V_2O_5, S, FeS_2, etc. The tailored system enables LIBs with high energy density and lifetimes for realizing high energy requirement systems in space, transportation, military applications, etc.

1. INTRODUCTION TO ENERGY STORAGE SYSTEMS: BATTERIES

1.1 Energy Storage Technologies

In the 21st century, there has been a paradigm shift from fossil fuels towards alternative, sustainable energy to leave the world in a better place for our future generations.[1, 2] Fossil fuels used by automobiles, industries, and power plants on burning release toxic gases and impurities to the environment and causes widespread pollution of the pristine resources. Dangerous emissions of greenhouse gases have slowly but steadily led to global warming and climate change, which threatens the existence of all the living organisms on Earth. If these existing trends continue without any intervention, then our planet would be rendered inhabitable in the near-sighted future.[1-4]

Energy, at the same time, is vital for our survival as we extract valuable work from it. Everything exists and sustains because of energy. It is found around in a variety of forms and the shift towards renewable energies is critical for recuperating the damages done so far. The renewable energy, in which everyone is heavily invested are solar, wind, geo-thermal, hydro-thermal, biofuels, tidal, etc. However, most of the time the energy is available in one form and desired in another. For this purpose, we require a converter or transducer, which can store and transport energy to the place of importance. The energy storage devices store the energy that can be delivered to perform useful work when called upon.[5] There are different types of energy storage technologies that exist today. They can be broadly classified as follows:

1. Electromagnetic: *Superconducting materials*
2. Thermal: *Phase-change materials, solar ponds, eutectic systems, molten salt storage*
3. Mechanical: *Pumped storage, flywheels, compressed air energy storage, spring*
4. Chemical: *Biofuels, Hydrogen-storage*
5. Electrochemical: *Batteries, Fuel cells, supercapacitors*

Each of these technologies has its pros and cons in terms of the scale of operation, energy-density, power, storage cost ($ kWh^{-1}), efficiency, and thus making each of them suitable for specific applications.[6, 7] Amongst all the technology, batteries have had a major impact on human

lives. The development of batteries dates back to 1748 when Benjamin Franklin coined the term 'Battery' and Alessandro Volta inventing the first-ever battery in 1800. Various chemistries of batteries have been developed since then viz., lead-acid, Zn-MnO_2, Ni-Cd, Ni-MH, Lithium-ion batteries (LIBs). These chemistries made it possible to realize portable electronics, such as radio, mobile phones, calculators, laptops, watches, etc. Lead-acid batteries and primary dry-cells are robust technologies, which reached a state of maturity with a long course of history. However, the coming of the age LIBs has been challenged these age-old technologies, with their high performances, light-weightiness, high energy-density, and power.

1.2 Lithium-ion Batteries

The evolution of LIBs though a recent technology, about four decades old, has a rich history of its development since invented as a Li-TiS_2 system in Prof. Stanley Whittingham's Exxon laboratory in 1978. In the early 1980s, Prof. John Goodenough experimented with lithium-cobalt oxide and observed significant improvement in battery potential by a factor of two. A few years later, Prof. Akira Yoshino swapped lithium metal anode with petroleum coke, making batteries safer and establishing the prototype of modern-day lithium-ion batteries. The professors were awarded the Nobel Prize in Chemistry for their discoveries in 2019, which led to the foundation of a wireless and fossil-fuel-free society.[8] There have been a variety of advances in terms of its configurations, electrolyte, lithium-salt, membranes, binders, etc. thus, making it possible to achieve the goal of electric vehicles (EVs).[9]

Modern-day LIBs exhibit the following characteristics: high energy density (up to 220 Wh kg^{-1}), high cell-voltage (~4.4 V), long shelf life (8–10 years), stable cycle lifetimes, low storage cost (~\$100 kWh^{-1}), and coulombic efficiencies (>99%). Typical LIB cells consist of four key components: cathode, anode, separator, and electrolyte.[4, 10] A schematic displaying a typical LIB is shown in Fig. 1.1. They demonstrate exceptionally high energy densities due to the low atomic weight and redox potential of lithium [E^0 (Li^+/Li = 3.04 V)].[4, 11, 12] On account of their intercalation mechanism, LIBs are known to be rechargeable for an extended duration of time. This mechanism is called the "rocking chair" mechanism as the lithium ions shuttle back and forth between two host materials, leading to low hysteresis and high cycle efficiency.[11] Lithium cobalt oxide ($LiCoO_2$) layered material cathode and graphite anode are the typical constituents of the

electrodes.[2, 4, 10, 13] During the charging process, Li ions are moved from the cathode to anode as given in the equation below:

$$LiCoO_2 \leftrightarrow Li_{1-x}CoO_2 + xLi^+ + x\,e^- \; (x \leq 0.6) \quad (160\ mAh\ g^{-1}) \tag{1.1}$$

$$Li^+ + e^- + 6C \leftrightarrow LiC_6 \quad (372\ mAh\ g^{-1}) \tag{1.2}$$

The reverse reactions illustrate the discharge process.

Sudden charge transfer between electrodes is prevented by the presence of a physical barrier known as the separator, which is a microporous polymer thin film. The separator serves as a conductor of Li-ions through its pores. They play a critical role in terminating cell operation during thermal runaway events by melting down and blocking the pores to dramatically increase the cell resistance.[11] They are generally multilayer structures of polyethylene (PE), and polypropylene (PP).

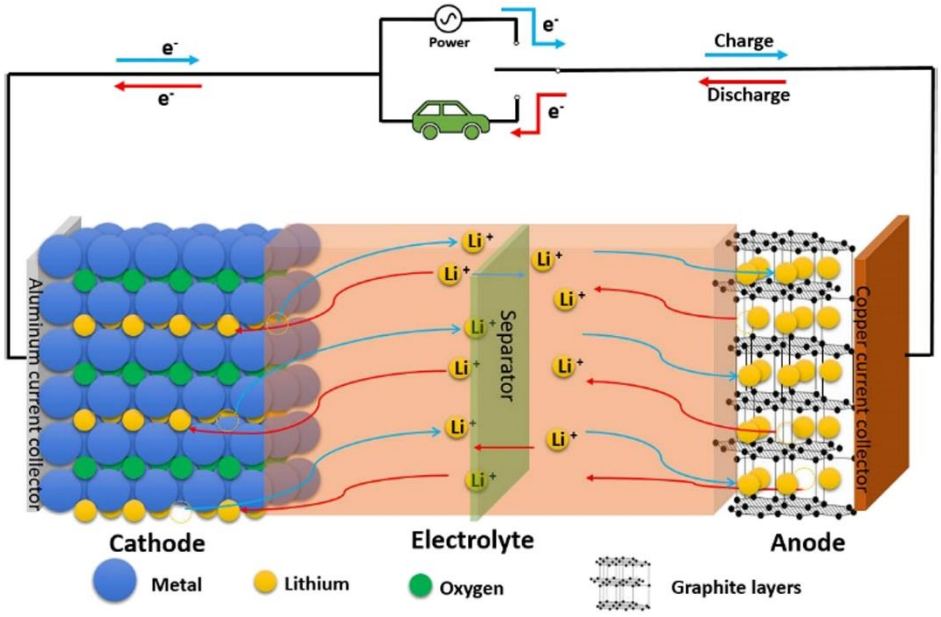

Figure 1.1: A typical lithium-ion battery representation. Reprinted from [14] with permission.

The electrolyte is an electronically insulating and ionically conductive medium, shuttling lithium-ions between the electrodes.[15] Commercial electrolytes have an inorganic lithium salt (e.g., $LiPF_6$) dissolved in an organic solvent blend (e.g., diethyl carbonate, DEC; and ethylene carbonate, EC) with additives (e.g., Fluoroethylene carbonate, FEC). These electrolytes face

partial decomposition on an anodic surface to form a polymeric/inorganic interface, which is a passivation layer called a solid electrolyte interphase (SEI).[15, 16] Favorably, the SEI has a low electron conductivity and high Li-ion conductivity that protects the anode from exfoliation, enables reversible lithium-ion diffusion, and prevents further SEI formation during cycling.[16] Unfortunately, SEI depletes the cathode capacity and energy density of the battery due to consumption of electrochemically-active lithium.[15] An uncontrolled buildup of SEI results in capacity loss and greater impedance that may eventually terminate electrochemical performance.[17] The SEI layer consists of multiple layers, specifically the interior layer made up of insoluble inorganic compounds like LiF, Li_2CO_3, Li_2O, and the exterior layer consisting of the low stable polymeric and organic compounds such as ROLi, ROCOOLi, and polycarbonates.[15] The particular properties of SEI are highly dependent upon the material properties of the electrodes, the electrolyte composition, and cell cycling parameters. Electrolyte additives (e.g. Fluoroethylene carbonate, FEC; propargyl-methylsulfone, PMS; vinylene carbonate (VC)) are known to have improved cycling stability of LIBs.[13]

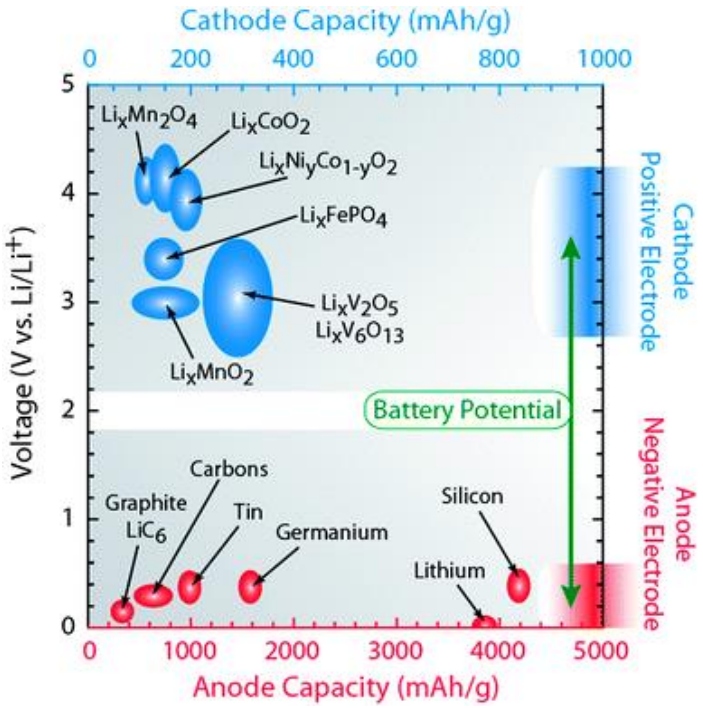

Figure 1.2: Diagram illustrating the lithium-ion capacity and electrochemical reduction potentials with respect to lithium metal for conventional anode (red axis) and cathode materials (blue axis). The battery potential is the relative difference between the voltage of the selected positive electrode materials (blue ovals) and the voltage of the corresponding negative electrode material (red ovals). Reprinted from [18] with permission from RSC Publications.

Since the last thirty years of commercialization of LIBs, the electrochemical field has seen substantial improvement in different aspects viz, capacity, charging rate, and lifetimes. Nevertheless, a few key factors that still has scope for improvement are the capacity, battery life, and safety of LIBs.[19] To improve these parameters, it is critical to understand the basic building blocks of batteries i.e., electrodes. Figure 1.2 shows the diagram of the capacity of electrodes for lithium-ion batteries versus voltage (V vs. Li^+/Li). Most of the cathodes have a capacity below 400 mAh g^{-1}, whereas Li (3860 mAh g^{-1}) or Si (3579 mAh g^{-1}) have a capacity exceeding about ten times that of the cathode.[20] The usage of these anodes as is or in form of composite would lead to a higher capacity anode and improving the energy density of LIBs. Thus, to realize reliable cycle stability and enhanced specific capacity, there is significant momentum towards fabricating new anode materials. Alloying type anodes have garnered a lot of attention. The atomic framework of Sn, Ge, or Si does not constrain the reaction with lithium resulting in high specific capacity than intercalation materials.[21] For example, Si alloys with Li in the reaction as follows:

$$15\ Li + Si \leftrightarrow Li_{15}Si_4 \quad (3579\ mAh\ g^{-1}) \tag{1.3}$$

Table 1 shows the comparison of the specific capacities amongst graphite and a few other alloying elements. However, volume expansion and contraction of the alloy materials during the alloying and dealloying steps, respectively, result in severe crack development, fracture, and pulverization of particles. Due to surface renewal of the particles, the re-formation of SEI occurs that consumes large quantities of electrolyte. Subsequently, delamination of electrode takes place resulting in degradation of the battery capacity and reduced cycle life.

Table 1.1: Comparison of specific capacities & volume changes for different anode materials.

Anode material	Specific capacity (mAh g^{-1})	Volume change (%)
LiC_6	372	10%
$Li_{13}Sn_5$	990	252%
$Li_{15}Si_4$	3579	320%
Li_9Al_4	2235	604%

For cathodes such as $LiFePO_4$ and $LiNi_xMn_yCo_zO_2$ (x+y+z =1), the SEI formation depletes their energy density and storage capacity. Consequently, the formation cycles lead to LIBs devoid of 15–25% less than their total energy density and full-cell capacity. And so, the graphite vs. Ni-rich $LiNi_{0.76}Mn_{0.14}Co_{0.10}O_2$ full cell delivers about 160 mAh g^{-1} than the potential capacity of 215 mAh g^{-1}. To control the substantial Li^+ ion reduction, a variety of strategies have been investigated, viz., cathodes with lithium additives,[22] prelithiating graphite,[23] blending of cathodes,[24] excessively loaded cathode mass (balancing 10–15% extra cathode capacity),[25] and film-forming additives.[26] Unfortunately, these measures modify the cell potential on account of the occurrence of empty Li^+ ion voids in the cathode, Though prelithiating graphite forms SEI layer and provides the initial Li^+ ions losses, it is a complex, costly process, which may not reasonable to scale up for industrial applications. An important point to note is that none of these methodologies completely minimizes the irreversible capacity loss. Additionally, there is a constant capacity fade (due to the reaction of electrolyte with Li^+ ion) leaving energy-depleted batteries within 4–5 years of usage. Hence, the development of extended life cycles for the current LIBs is crucial for energy-demanding applications.

Another component of the LIBs that has a significant influence on the performance and energy density is the separator. Separator influences ion transport across the electrodes, and its inherent physicochemical properties affect the interfacial interactions with solvent and electrodes, concentration polarization, and overpotentials of the cell. During some instances when the safety and mechanical integrity of the LIBs are compromised, separators can play an important role in preventing an internal short circuit. For Li-S chemistry, separators may help mitigate the shuttling of polysulfides across them. Some applications may require the batteries to be operated at elevated temperatures, and it becomes critical to ensure the structural and morphological stability of the separators. Polyolefins at elevated temperatures tend to become flimsy and affect the homogenous transport of ions. With enhanced kinetics and solvent interactions, it is required to develop more separator systems that tackle different issues of varied chemistries.

Any safety related incidents of LIBs can damage and pose a threat for the battery businesses and industries.[27, 28] Although the number of LIBs' safety-related events is 1 in million, there is room for improvement to match up the semiconductor industries.[29, 30] The major challenges encountered while monitoring as well as controlling the states for the LIBs are the State of Charge (SoC), State of Health (SoH), and temperature profile. Ineffective control and monitoring can

reduce battery performance, lifetimes, or cause mishaps like explosions and fires. The thermal stability of the battery can be deconvoluted with the fluctuations in the battery temperature. Thus, the development of a monitoring system for improved detection and mitigation strategy becomes inevitable.

1.3 Dissertation Overview

This thesis is motivated by the surge in the interest towards LIBs, especially in EVs. Keeping up with the demands requires upgradation in the components of the batteries and enhancing the safety features to avoid undesirable mishaps. Chapter 2 encompasses my work on the development of a ternary composite of silicon with graphite and amorphous carbon through pyrolysis. This resulted in enhanced physical and electrical interactions of encapsulated silicon with graphite through starch-derived amorphous carbon. The presence of the buffer layer of amorphous carbon around silicon nanoparticles accommodated the Si volume expansion during lithiation. The evolution of the composite was in situ observed using environmental transmission electron microscopy (ETEM) from 50 ℃ to 600 ℃. Through the use of advanced multimodule calorimetry (MMC), I derived the thermal signature of the full–cell of LCO cathode – Si-composite anode by heating from 25 ℃ to 300 ℃. The in-situ ETEM was performed in collaboration with Dr. Anton Sedaiko and Dr. Murray Thomson from the University of Toronto, Ontario, Canada.

Chapter 3 presents work on discovering a novel configuration for LIBs called Reserve lithium-ion batteries (RLIBs). With RLIBs, in situ lithiation of lithium-ion free cathode and anode is made possible. Here, I showed the RLIB system comprising of V_2O_5 cathode and mesocarbon microbeads anode with lithium reservoir electrode. Reservoir provided the Li^+ ions necessary for in situ construction of full–cell ($Li_2V_2O_5$ vs. MCMB). The reservoir helped construct the SEI layer across MCMB anode. I explored various modes of operating RLIB to establish various important key results of indirect and direct lithiation. I also scaled this technology up through the assembly of the pouch cells. The concept discussion was made with Dr. Manikandan Palanisamy.

Chapter 4 describes my work on the elucidation of the electrochemical performance of the critical point dried–aramid nanofibers (CPD-ANF) separators, which possess huge potential to substitute conventional polypropylene separators. I observed long-stable cycling at 25 ℃, 40 ℃, and 50 ℃ for lithium-iron phosphate half–cell. Full–cell study was demonstrated with LFP–MCMB. Thermal safety analyses were compared with polypropylene separators via

thermogravimetric analysis (TGA), differential scanning calorimetry (DSC), and MMC. This project was performed in collaboration with Suyash Oka and Dr. Jodie Lutkenhaus from Texas A&M University, TX, USA, where they developed the CPD-ANF and tested its mechanical properties compared to PP at varied temperatures.

Chapter 5 explores the hypothesis of enhancing the performance of Li-S batteries through the development of a modified microporous membrane by suppressing the shuttling of polysulfide across the separator. The tailored separator consisted of a PP separator modified with a polydopamine layer, which was further coated with a thin graphene layer. With this separator, I attempted to solve three critical problems of lithium-sulfur chemistry viz., polysulfides shuttling, lithium-dendrite formation, and enhance the conductivity of sulfur cathode. Deep Jokhakar, Brightvolt Inc., IN, USA supported us to scale up the system into single-layer pouch cells for testing their performance.

Chapter 6 discusses our work on operando sensing of internal temperature of LIBs via internal sensors. This work was done in collaboration with Dr. Bing Li and Dr. Vikas Tomar at Purdue University, IN, USA. I constructed the LIBs with an internal resistance temperature detector (RTD) and tested their performance in a harsh acidic electrolytic environment. We hypothesized that if the sensor was placed beneath the electrode current collector, then it wouldn't interfere with the electrochemical reactions and carry the thermal signature rapidly of LIB. Notably, the designed construction operated efficiently and detected thermal runaway situations in quite advance.

Chapter 7 briefly summarizes the major findings of this Ph.D. dissertation and provides a potential scope of research for the future. While novel silicon composite was designed and tested for its material safety aspects through MMC experiments, construction of pouch cells or 18650 format configurations could explain its practical feasibilities. Detailed modeling simulation could provide further insights into the thermal degradation, Si expansion, and possibilities of different engineering methods to addressing these concerns. From my thesis, we understand various potential uses for RLIBs that could revolutionize the LIBs market for numerous applications. Due to RLIBs being an unexplored system, there are numerous studies to elucidate thermal safety aspects, cathode degradation, detailed energy density calculations, ideal scaled-up format for RLIBS, stability of reservoir on prolonged usage of batteries. Electrochemical impedance analyses remain a critical technique to further comprehend the formation of the SEI layer in this novel

system. Separators play a critical role despite being an inactive components in the batteries. They affect the transport of ions across the electrodes, act as electrolyte reservoir and safety net in case of thermal runaway situations, dependent on the interfacial interactions with electrolyte. Mechanistically elucidating these behaviors via DFT and MD simulations, could provide various answers to tailored and novel separator systems. As observed from my work on the RTD sensors, they are an effective way to predict thermal accidents in advance and the use of an advanced battery management system would help mitigate them. The practicality of this sensor on module level and in different cell configurations is yet to be analyzed. The presence of such devices could help detect, predict and prevent thermal runaway situations. All these further studies will help in the progress of the electrochemistry field with widespread of the batteries in a variety of applications.

1.4 References

1. Y. Nishi, *Journal of Power Sources* **2001**, 100: p. 101-106.
2. J.M. Tarascon and M. Armand, *Nature* **2001**, 414(6861): p. 359-367.
3. T. Kojima, T. Ishizu, T. Horiba, and M. Yoshikawa, *Journal of Power Sources* **2009**, 189(1): p. 859-863.
4. J.B. Goodenough and Y. Kim, *Chemistry of Materials* **2010**, 22(3): p. 587-603.
5. M. Armand and J.M. Tarascon, *Nature* **2008**, 451(7179): p. 652-657.
6. S. Goriparti, E. Miele, F. De Angelis, E. Di Fabrizio, R. Proietti Zaccaria, and C. Capiglia, *Journal of Power Sources* **2014**, 257: p. 421-443.
7. U. Kasavajjula, C. Wang, and A.J. Appleby, *Journal of Power Sources* **2007**, 163(2): p. 1003-1039.
8. *The Nobel Prize in Chemistry 2019*. 2019 [cited 2019 12-09-2019]; Available from: https://www.nobelprize.org/prizes/chemistry/2019/summary/.
9. L.H.J. Raijmakers, D.L. Danilov, R.A. Eichel, and P.H.L. Notten, *Applied Energy* **2019**, 240: p. 918-945.
10. M.S. Whittingham, *Chemical Reviews* **2004**, 104(10): p. 4271-4302.
11. V. Mathew, S. Kim, J. Kang, J. Gim, J. Song, J.P. Baboo, W. Park, D. Ahn, J. Han, L. Gu, Y. Wang, Y.-S. Hu, Y.-K. Sun, and J. Kim, *NPG Asia Materials* **2014**, 6(10): p. e138-e138.
12. J.B. Goodenough and K.-S. Park, *Journal of the American Chemical Society* **2013**, 135(4): p. 1167-1176.

13. V. Etacheri, R. Marom, R. Elazari, G. Salitra, and D. Aurbach, *Energy & Environmental Science* **2011**, 4(9).
14. S. Liang, W. Yan, X. Wu, Y. Zhang, Y. Zhu, H. Wang, and Y. Wu, *Solid State Ionics* **2018**, 318: p. 2-18.
15. E. Peled and S. Menkin, *Journal of The Electrochemical Society* **2017**, 164(7): p. A1703-A1719.
16. E. Peled, *Journal of The Electrochemical Society* **1979**, 126(12): p. 2047-2051.
17. S.J. An, J. Li, C. Daniel, D. Mohanty, S. Nagpure, and D.L. Wood, *Carbon* **2016**, 105: p. 52-76.
18. B.J. Landi, M.J. Ganter, C.D. Cress, R.A. DiLeo, and R.P. Raffaelle, *Energy & Environmental Science* **2009**, 2(6).
19. J. Deng, C. Bae, J. Marcicki, A. Masias, and T. Miller, *Nature Energy* **2018**, 3(4): p. 261-266.
20. M.H. Parekh, V.P. Parikh, P.J. Kim, S. Misra, Z. Qi, H. Wang, and V.G. Pol, *Carbon* **2019**, 148: p. 36-43.
21. J.-Y. Li, Q. Xu, G. Li, Y.-X. Yin, L.-J. Wan, and Y.-G. Guo, *Materials Chemistry Frontiers* **2017**, 1(9): p. 1691-1708.
22. G. Gabrielli, M. Marinaro, M. Mancini, P. Axmann, and M. Wohlfahrt-Mehrens, *Journal of Power Sources* **2017**, 351: p. 35-44.
23. J. Zhao, Z. Lu, H. Wang, W. Liu, H.-W. Lee, K. Yan, D. Zhuo, D. Lin, N. Liu, and Y. Cui, *Journal of the American Chemical Society* **2015**, 137(26): p. 8372-8375.
24. S.B. Chikkannanavar, D.M. Bernardi, and L. Liu, *Journal of Power Sources* **2014**, 248: p. 91-100.
25. J. Kasnatscheew, T. Placke, B. Streipert, S. Rothermel, R. Wagner, P. Meister, I.C. Laskovic, and M. Winter, *Journal of The Electrochemical Society* **2017**, 164(12): p. A2479-A2486.
26. K. Ciosek Högström, S. Malmgren, M. Hahlin, H. Rensmo, F. Thébault, P. Johansson, and K. Edström, *The Journal of Physical Chemistry C* **2013**, 117(45): p. 23476-23486.
27. J. Mullen. *Samsung shares plummet as Note 7 debacle deepens*. 2016 [cited 2019 12/09/2019].
28. D. Seetharaman. *Tesla shares drop 6 percent after report of Model S fire*. 2013 [cited 2019 12/09/2019].

29. *Safety Concerns with Li-ion*. 2019 [cited 2019 12/09/2019]; Available from: https://batteryuniversity.com/learn/article/safety_concerns_with_li_ion.
30. Q. Wang, P. Ping, X. Zhao, G. Chu, J. Sun, and C. Chen, *Journal of Power Sources* **2012**, 208: p. 210-224.

2. SILICON ANODE: ITS IN SITU MECHANISTIC ELUCIDATION OF ENCAPSULATION, NETWORKING, AND THERMAL SAFETY ASPECTS

A version of this chapter has been previously published as journal articles: Mihit H. Parekh, Anton D. Sediako, Ali Naseri, Murray J. Thomson, and Vilas G. Pol. *In Situ Mechanistic Elucidation of Superior Si-C-Graphite Li-Ion Battery Anode Formation with Thermal Safety Aspects*. Ad. Energy Mat. 2019, 1902799; and Mihit H. Parekh, Vihang P. Parikh, Patrick J. Kim, Shikhar Misra, Zhimin Qi, Haiyan Wang, Vilas G. Pol. *Encapsulation and networking of silicon nanoparticles using amorphous carbon and graphite for high-performance Li-ion batteries*. Carbon. 2019, 148, p. 36-43. It is reproduced here with permission from Wiley and Elsevier. The main journal articles and supporting information have been merged, and the text and figures have been modified where appropriate. Dr. Anton D. Sediako, Ali Naseri, Dr. Murray J. Thomson performed and analyzed environmental transmission electron microscopy (ETEM) in Ad. Energy Mat. publication. Dr. Shikhar Misra, Dr. Zhimin Qi, and Dr. Haiyan Wang performed and analyzed high-resolution transmission electron microscopy in Carbon publication. Dr. Patrick Kim and Vihang Parikh provided their insights on the project. Manuscript preparation was performed by Mihit H. Parekh and Anton D. Sedaiko for Ad. Energy. Mat. and by Mihit H. Parekh for Carbon journal.

Ad. Energy Mat. DOI: 10.1002/aenm.201902799
Carbon DOI: 10.1016/j.carbon.2019.03.037

2.1 Overview

A composite anode material synthesized using silicon nanoparticles, micrometer-sized graphite particles and starch-derived amorphous carbon (GCSi) offer scalability and enhanced electrochemical performance when compared to the existing graphite anodes. Mechanistic elucidation of the formation steps of tailored GCSi composite was achieved with in situ Environmental Transmission Electron Microscopy (ETEM) and thermal safety aspects of the composite anode were studied for the first time using specially designed multimode calorimetry for coin cell studies. Electrochemical analysis of the composite anode delivered a high initial discharge capacity (1126 mAh g^{-1}) and yielded high coulombic efficiency of 83% in the first charge cycle. At applying current density of 500 mA g^{-1}, the anode composite retains 448 mAh g^{-1} specific capacity after 100 cycles. Achieved cycling stability is a result of the improved interfacial binding made possible by the interconnected architecture of wheat-derived amorphous carbon, thereby enhancing the electrochemical kinetics and decreases the inherent issues associated with volume expansion and pulverization of pristine Si electrodes. Comparing the energy released during

thermal runaway, per the specific capacity of the full cell, the GCSi composite released slightly lesser heat than the conventional graphitic anode, suggesting a synergistic effect of each ingredient of the GCSi composite to yield a safer anode.

2.2 Introduction

To compete with traditional hydrocarbon energy sources and meet the demands of battery applications, the next generation of lithium-ion batteries (LIBs) needs to have high specific energy, high energy density, low cost, and reliable safety characteristics.[1, 2] In order to improve electrochemical characteristics without sacrificing thermal safety, a deeper understanding of the material synthesis/fabrication, interfacial behavior, and thermal—chemical stabilities are vital.[3] Amongst the electrodes used in LIBs, graphite anode has been the mainstay of the industry since the 1980s. Conventional graphite has high electrical conductivity (3×10^5 S m^{-1}) and mechanical strength but is limited by low theoretical capacity (372 mAh g^{-1}). Nearly 30 years since then, researchers are now brushing up against its limitations.[4] There has been a huge thrust in fabricating new anode materials for the LIBs with enhanced specific capacity and reliable cycle stability. As a possible solution, alloys have received much attention.[5, 6] The alloys of Si, Ge, or Sn have higher specific capacity than intercalation materials due to their atomic framework which does not constrain the reaction. Among all the emerging materials, Si is considered promising due to its environmentally benign properties, large availability, excellent theoretical capacity (3589 mAh g^{-1}, 9780 mAh cm^{-3} for $Li_{15}Si_4$ alloy at room temperature), and attractive operating potential.[7]

Problematically, the intercalated Si, $Li_{3.75}Si$, swells in volume by about 320% during charging (Lithiation). Such huge volumetric expansion causes large material stresses, resulting in anode cracking, fracturing, loss of electrical contact (delamination), unstable SEI, and even catastrophic cell failure.[8-10] Naturally, this is unacceptable for practical and industrial applications. To overcome the capacity limitations of carbon, and the mechanical limitations of silicon, manufacturers have moved into composite materials - with the primary structure consisting of graphitic carbon, with silicon nanoparticles implanted within. First reported by Yoshio *et al.* in 2002, the C/Si composites did improve capacity, but the silicon nanoparticles were difficult to merge with the carbon bulk.[11] After repeated cycling, it was found that the particles separate and capacity drops.[12] Zhang *et al.* prepared core-shell structure (Si@C) using silicon nanoparticles

(Si-NPs) and emulsion polymerization of acrylonitrile, followed by pyrolysis. The composite retained only half of its initial capacity after 20 cycles.[13] Recently, Zhou *et al.* conducted a study on the Si/graphite@N-doped carbon core-shell composite. The composite preparation involved liquid mixing, spray drying, coating by oxidative self-polymerization of dopamine and pyrolysis. The composite delivered an initial reversible capacity of 741 mAh g^{-1} at 300 mA g^{-1} and 611 mAh g^{-1} after 100th cycles.[14] Studies by Li *et al* surpassed this performance further by encapsulating the Si nanoparticles inside "multilayer graphene" structures, which retained 90% of their capacity after 100 cycles.[15] While this dramatically boosted cycling capacity and stability, the use of graphene required multiple days of complex fabrication with high-risk oxidizing agents; large-scale, commercial synthesis of such materials remains cost-prohibitive.

The proposed composite anode material can be synthesized through low-cost industrial methods, and as such are scalable to large-scale production. Through embedding Si nanoparticles (Si-NPs) in a graphitic carbon matrix connected by amorphous soft carbon - this composite material promises enhanced capacity, lifespan, and stability. Specifically, it must be shown that the cells fabricated undergo low energy losses in the course of charge and discharge cycling, maintain high performance, and meet environmental standards for production and disposal. The major aim of this work is to tailor a composite, with double the capacity of graphite. A capacity higher than double would require thicker cathodes, which come with several critical issues: higher impedance for electrons in the solid phase and mass transfer of lithium ions in the electrolyte phase. The overall capacity of the cell drops due to higher over potentials upon charging and discharging within fixed voltage limits.[16] Concurrently, for thick electrodes, the geometric current density in the separator is higher, which creates additional overpotential. During charging, this could lead to lithium plating on graphite in proximity to the separator.[16] Finally, this work aims to understand and validate the new composite material and cell behavior is crucial for new LIB designs- as the demanding applications and catastrophic consequences of failure provide a little margin for error. To date, however, the mechanistic elucidation of GCSi formation as a function of increasing temperature during synthesis remains unknown. Moreover, to date, no studies have been performed on the thermal safety behavior of GCSi, a crucial step before any new materials can be implemented for practical use.

In this report, we present a novel composite GCSi anode material with its formation mechanism established via *in situ* ETEM. Moreover, the thermal safety analysis of the GCSi

material is benchmarked against a reference graphite anode for the first time, employing *in situ* multimode calorimetry. Multimode calorimetry directly studies thermal runaway events using a whole coin cell (comprising an anode, cathode, electrolyte, separator, etc.) either in the charge or discharge state as a function of increasing temperature. This mechanistic elucidation and thermal safety studies are highly important steps in the advancement of Si-based composite anodes for the next generation of LIBs. Through a combination of *ex situ, in situ,* and cell performance testing - a complete picture of the anode behavior, advantages, and drawbacks are obtained.

2.3 Experimental Methods

Material synthesis focuses on the scalable production process of combining graphitic carbon, wheat starch, and silicon nanoparticles into a homogeneous powder via ball milling. After treatment, this powder is then heat-treated and visualized in situ as the material anneals to better understand the process.

2.3.1 Material Preparation:

Graphite powder was obtained from MSE Supplies and used as received. Si-NPs (diameter around 100 nm), Carboxyl Methyl Cellulose (CMC), Fluoroethylene carbonate (FEC), 1M $LiPF_6$ solution in Ethylene Carbonate (EC)/Diethyl Carbonate (DEC) (50/50 v/v) were sourced from Sigma Aldrich. The starch material source is wheat flour, purchased from Ashirvaad ITC Ltd. Super P carbon black (SP) was sourced from TIMCAL.

2.3.2 Electrode and Cell Fabrication:

Si nanoparticles were added to the starch powder in the optimized ratio of 2:3 and ball milled for 20 minutes at 15 Hz. Graphite was then added with a 4:5 ratio and milled again. In presence of Argon gas, the final precursor was baked at 600 °C for 2 hours. The final material is labeled GCSi and has a Si loading of 30.58 wt. %. Electrodes using the GCSi composite were prepared using 80 wt% GCSi, 10 wt% CMC, 10 wt% SP in deionized water. Using the Thinky mixer, the slurry was uniformly mixed and homogenized for 10 minutes. The homogenized slurry was cast onto the Copper current collector by the doctor blade technique. Once laminated, it was

dried at 80 °C overnight in a vacuum oven. The dried laminate was calendered before punching the electrode discs from it. The loading mass of the electrodes is ca. 2 mg cm^{-2}.

2.3.3 Electrochemical Characterization:

Electrodes of 15.5 mm were punched from the dried laminate and dried in a vacuum oven before using them in making CR2032 coin cells (MTI Corporation) for determining the electrochemical performance. The cells were prepared in the glove box having an inert (99.998% argon) atmosphere with H_2O and O_2 concentration <1 ppm. Cells were assembled containing the composite electrodes, Celgrad 2500 separators, and electrolyte. The electrolyte consisted of 5 vol.% FEC in 1M $LiPF_6$ dissolved in EC/DEC solution. Galvanostatic cycling was conducted employing Arbin cycler within voltage ranges of 0.01 – 2.0 V and current densities of 50, 100, 200, 500, and 1000 mA g^{-1}. To determine the cycle stability of the composite, the constant current density of 500 mA g^{-1} was applied. Cell-specific capacities were calculated using the active mass (excluding the mass of binder and Super P carbon black) of the electrodes. Cyclic voltammetry (CV) was collected using the Gamry-600 reference system at a scan rate of 0.1 mV s^{-1} from 10 mV to 2 V. Electrochemical impedance spectroscopy (EIS) measurements were also conducted by Gamry-600 reference system with data collected at 0.1 V after 1^{st}, 10^{th} and 100^{th} cycle. AC voltage perturbation of 10 mV amplitude was applied over the frequency range 1MHz — 0.01 Hz. Potentials mentioned are versus Li^+/Li.

2.3.4 Bulk Sample Characterization:

Thermal Gravimetric Analyzer-i1000 (TGA-i1000, Instrument Specialists Incorporated) was utilized for the determination of the material weight loss. The X-ray powder diffraction pattern was recorded with the Rigaku SmartLab XRD having a Cu Kα radiation source, which scanned at the rate of 2-degree min^{-1} from 10° to 90° two theta. Thermo Scientific DXR 2 Raman Microscope equipped with a 633-nm laser (3 mW) was used to generate the Raman spectra. Multiple Module Calorimetry MMC 274 Nexus (Netzsch Gerätebau GmbH, Germany) was used to conduct calorimetry experiments of the cells from room temperature to 300 °C.

2.3.5 *In situ* Electron Microscopy Analysis:

All electron microscopy was performed on a Hitachi HF3300 Environmental Transmission Electron Microscope. The HF3300 ETEM employed in this study provided an exceptional platform for fully characterizing the material on one instrument pre and post pyrolysis – instead of requiring multiple other specialized instruments. By using the controlled environment, heating holder, and detectors on the ETEM, sample handling was kept to a minimum, and we were able to track the evolution of the same particle. This allowed us to achieve high repeatability and have confidence that the observed changes were the result of underlying material mechanisms.[18] To achieve stable *in situ* heating experiments, a micro-electro-mechanical-system (MEMS) heating substrates (pn: HTN-0101) from Norcada Inc was used, shown in Figure A.1-A. The MEMS substrates were mechanically coated with the sample as (Supporting Information 1). The MEMS heating substrates are then fitted into a Hitachi Higher Technologies Gas Injection / Heating holder (shown in Figure 2.1), which provides voltage for heating and an injection port for gases during imaging. The holder is then inserted into the electron beam path inside the ETEM. Together, the ETEM, the holder, and the MEMs substrate provide a stable infrastructure for heating the sample up to 1200°C.

The sample is then imaged, requiring a specific set of conditions for the studies. Each of the *in-situ* tests required a sample with all three of the composite components intersecting inside the approximately 2µm viewing windows of the MEMS chip. The intersecting area also needed to be thin enough for high-resolution imaging. Each test is only run once on the MEMS substrate – as the GCSi sample evolved non-reversibly during heating. Each of the image sets and videos are shown is for a new sample and location. For all microscopy images, EDS elemental mapping (Bruker XFlash 6 | 60 EDS Detector) was performed before and after the experiments to confirm the observed elements. ETEM imaging was performed using a GATAN Orious TEM Camera, as well as scanning transmission electron microscopy (STEM) using secondary electron (SE), a direct image of the cross-section (BF), and dark field (DF) detectors. The TEM cameras provide an ultra-high-resolution image of a cross-section of the sample. The SE detectors raster the beam across the sample and collect the generated electrons from the surface layer. This provides a high-resolution, 3D, topographical analysis crucial for commenting on any potential surface reactions. The DF collects the diffracted signal by the sample generating a cross-sectional image. The BF

and DF images are sensitive to the elements present and clearly show different elements with different brightness.

2.4 Results & Discussion

Figure 2.1 demonstrates a schematic representation of the development of a composite, comprising of Si, graphite, and wheat flour, at elevated temperatures using *in-situ* ETEM coupled with thermal safety analysis using multimode calorimetry (MMC). ETEM studies reveal the formation of a bridge between Si and graphite through an amorphous carbon network. Achieved GCSi composite was used to fabricate a LIB anode, which was used to assemble coin cells. In addition to studying the electrochemical performance of these coin cells, we have studied multimode calorimetry (MMC) for the first time for testing the thermal safety aspects of the tailored GCSi composite. MMC recorded thermal signature (heat flux) of whole coin cell at elevated temperature helps in understanding the thermal safety behavior of these advanced LIBs. The four primary stages describing the overall study are: 1) *in situ* thermal treatment characterization during material synthesis, 2) cell fabrication utilizing composite anode, 3) detailed electrochemical analysis, and 4) thermal safety analysis.

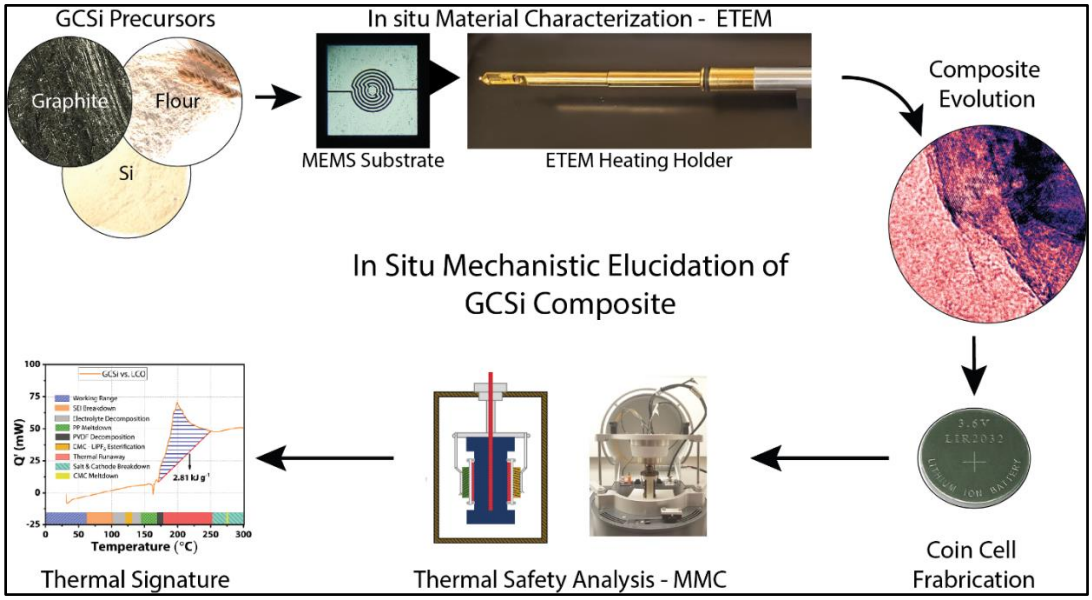

Figure 2.1: The loading of precursors, in situ GCSi composite formation during the heat treatment in ETEM, resulting in composite evolution, coin cell fabrication, thermal safety studies, and the overall safety outcome.

Material synthesis focuses on combining graphitic carbon, wheat starch, and silicon nanoparticles into a uniform powder followed by *in situ* ETEM visualization during heat treatment to understand the process synthesis mechanism. Initially, electron microscopy imaging was performed on the individual components, which make up the composite anode material, depicted in Fig. 2.2. It can be seen that the silicon particles are primarily spherical. The graphitic carbon appears as sharp sheets, while the amorphous starch appears as disordered "soft" clusters. Pielichowski and Njuguna identified two primary stages during thermal decomposition of starches below 500 °C.[19] The first, occurring below 300 °C, is the loss of water content and physical dehydration. This depends on the initial water content of the starch and ends at 120 °C.[19] Above this temperature, dehydrogenation and breakdown begin to occur in the glucose rings, with the formation of C=C bonds. The formation of C=C bonds then drives the conversion from hydroxyl groups losing the OH bond and transitioning to benzene and furan-like structures.[19] This transition continues through 500 °C and ultimately results in uniform amorphous carbon structures. In this study, it is crucial to understand this transition in a composite anode formation. Heating experiments were run with the starch employed for the GCSi mixture- as the primary transition is expected to occur from 400-500 °C. To directly observe this transition, the electron microscopy for this work was performed using the Hitachi HF3300 operating at 300kV, in the Scanning Transmission Electron Microscopy (STEM) mode. This operational setting allowed full characterization of the same GCSi sample clusters with cross-sectional imaging (Bright Field, BF, and Dark Field, DF), surface imaging (SE), and elemental analysis (EDS). Experiments were also conducted on the individual sample "ingredients", as well as the GCSi anode composite to demonstrate how each component evolved over time, as well as how the components interact during heating.

In situ imaging shown in Fig. 2.2 – Starch Under Heating, illustrates how the starch changes over the course of the heating ramp. As the temperatures increase, the starch releases the small amount of water it had absorbed (< 2%) below 100 °C and carbonizes. Thermo-gravimetric analysis (TGA) tests (Figure 2.2: TGA) were performed for all the ingredients as well as the mixture. With the starch, the TGA showed a clear and dramatic transition and loss of mass from 300 to 400 °C, with an 81% mass loss occurs during this heating transition. *In situ* electron microscopy studies of the material, shown in Fig. 2.2 shows a 41% shrinkage in surface area of the particle observed when the images are analyzed with threshold area analysis. These

observations are consistent with the dehydrogenation and second stage transition studies observed by Pielichowski and Njuguna, where the starch transitions from disordered and disconnected hydroxyl carbon groups to the mostly uniform and amorphous aromatic species.[19] It was also observed that the silicon and graphite ingredients remained unchanged during TGA heating, while the GCSi mixture lost 38% of its mass, consistent with its addition.

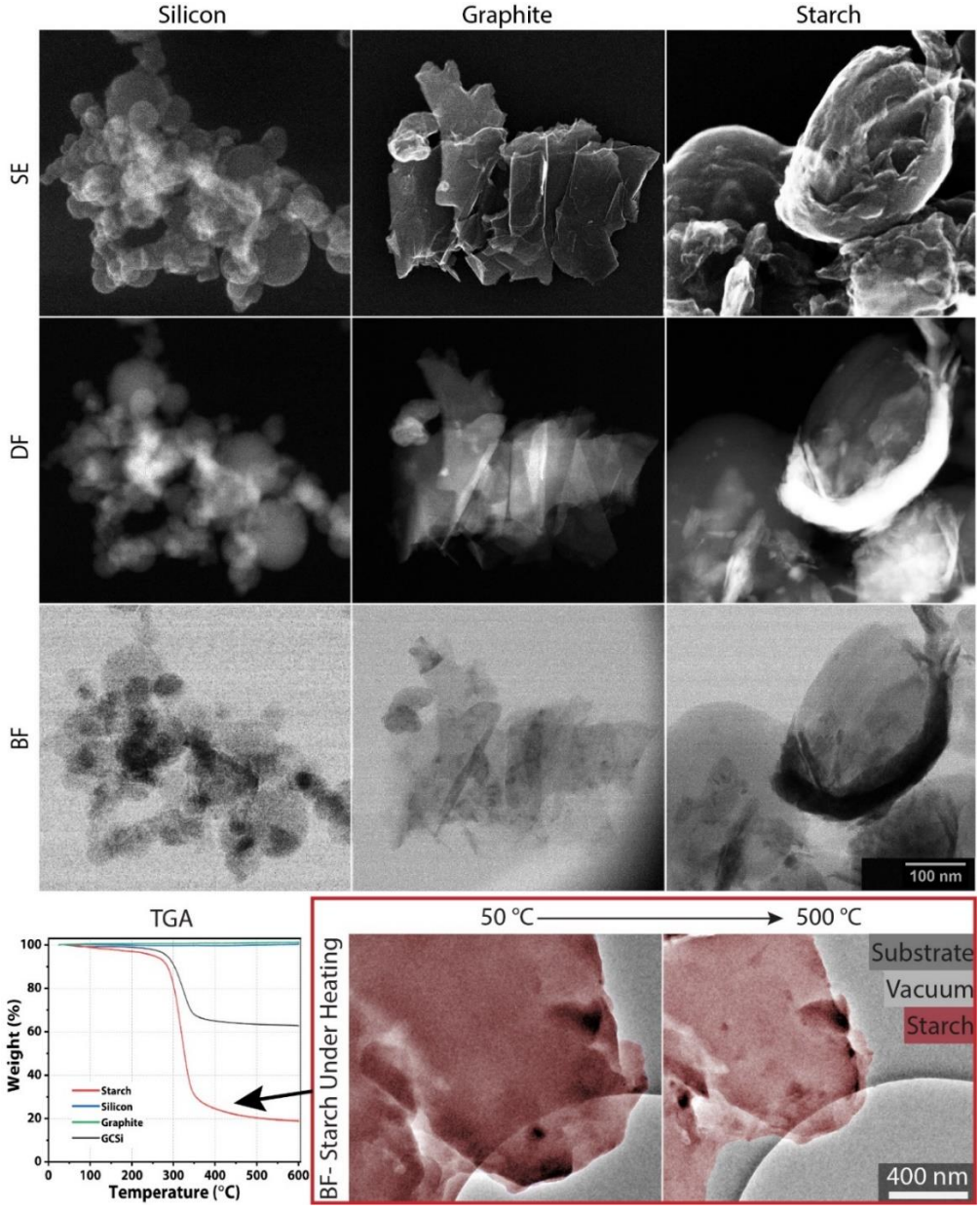

Figure 2.2: SE, DF, BF images of components, which make up the composite anode material (Scale bar = 100nm for all the images). TGA: TGA analysis of the GCSi ingredients, as well as the GCSi mixture. Graphite and silicon do not change or lose mass at temperatures under 600 °C, while starch loses up to 80% of its mass during heating. RED: ETEM imaging of the starch carbonization.

Samples of the GCSi anode material were then prepared where Graphite, Starch, and Silicon overlapped. The silicon particles were buried in a cluster of starch. This cluster sat on top of a sheet of graphite -all suspended over vacuum on the ETEM MEMS heating substrate. As the composite sample was heated, the STEM images show that the starch undergoing carbonization and merging with the surrounding material as sharp disconnected edges on the surface are smoothed out. The transition and homogenization can be seen in Fig. 2.3 SE-Zoom frames.

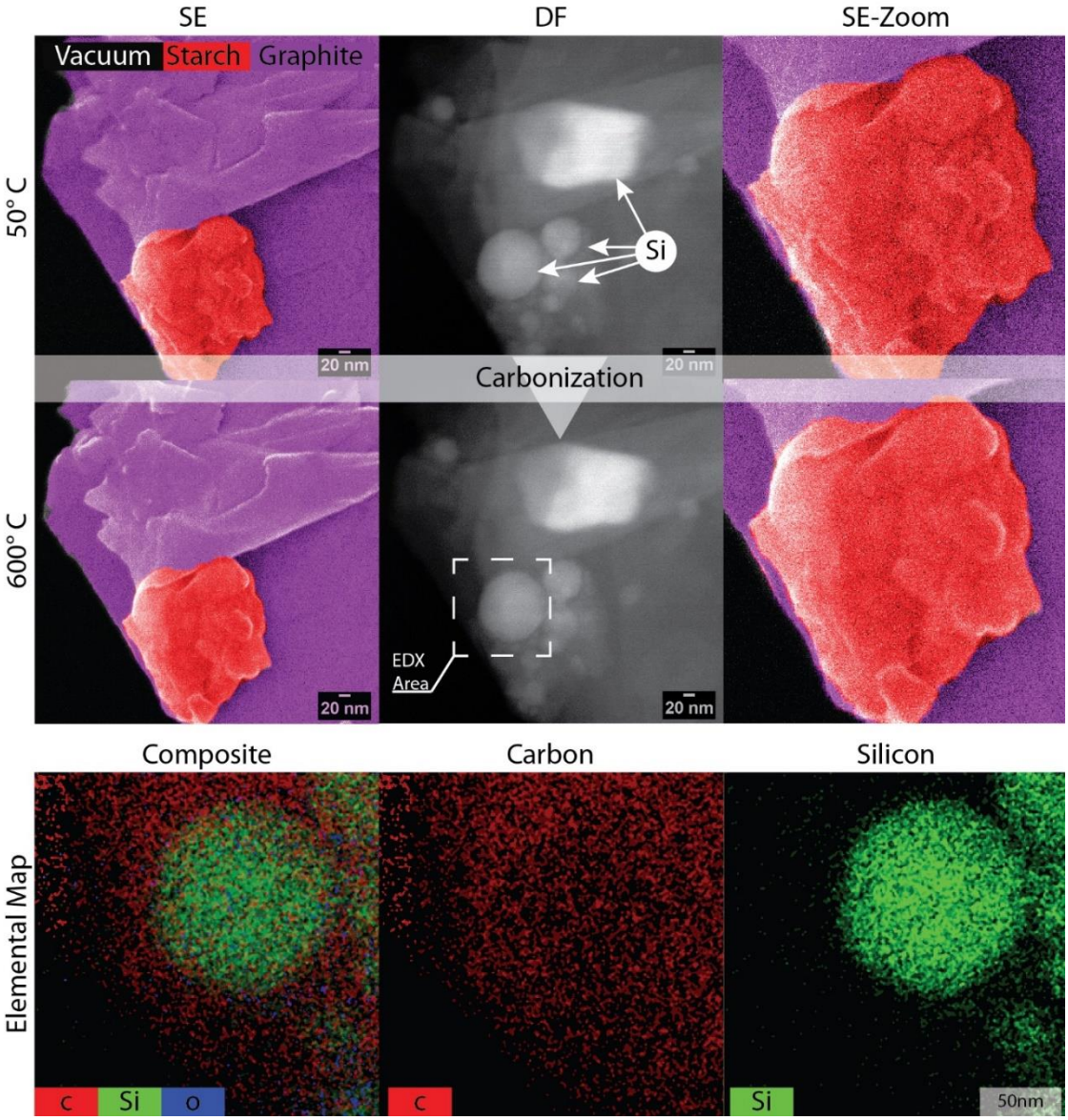

Figure 2.3: STEM, DF, and elemental map of anode material transformation. The starch can be seen to shrink and carbonize, with the surface sharp edges softening and fusing into a homogeneous mixture. EDS analysis confirms the elements observed are carbon and silicon.

Further analysis was also conducted with high-resolution TEM imaging on two new samples, with the TEM sample shown in Fig. 2.4 A-C and the HRTEM sample in Fig. 2.4 D-F. The strains of nonhomogeneous carbon inside the starch merged bit by bit, shrank, and eventually homogenized into a continuous mass. This homogenization increases the interfacial contact between the three components, with fewer fractures and disjointed atomic planes shown in Fig. 2.4-C and Fig. 2.4-E, binding the Si particles in a "cage" of carbon, and connecting all components at the atomic level. This process thus allows for higher conductivity and performance as shown by electrochemical studies in Fig. 2.5.

Following the *in-situ* imaging, XRD and Raman spectroscopy were performed for graphite, silicon, and post-annealing GCSi samples in order to study the phase purity and crystallinity of the ingredients and mix. Figure 2.3-H shows the XRD patterns for graphite and GCSi. As previous studies have found,[20, 21] pure graphite has a hexagonal crystal structure and its primary XRD peak at 26.4° two-theta. When combined with silicon nanoparticles, characteristic 2 peaks of cubic crystal structured Si are observable at 28.4°, 47.4°, 56.1°, 69.1°, and 76.3°. Raman spectra analysis (Figure 2.3-G) of graphite shows two characteristic bands, at 1575 cm^{-1} and 1328 cm^{-1}. These bands result from the G-band and D-band resonance.[22] The ratio (*R*) of the areas under these bands (D-band: G-band) quantitatively measures the ratio of graphitic to amorphous carbon. The high and narrow peak of the G band in the graphite shows that the sample is, as expected, entirely graphitic in structure. When mixed with Si nanoparticles and the amorphous starch, the GCSi composite sample shows a Raman pattern of all present elements; the G peak widens while the D peak grows, showing the effect of the starch-derived carbon in the mixture. A small peak from the silicon particle can be seen at 518 cm^{-1},[23] suggesting the particles generating the signal are buried under clusters of carbon, as seen in the ETEM images.

2.4.1 Electrochemical performance of the tailored composite GCSi anode

To quantify the performance of the tailored GCSi anode, electrochemical studies were conducted in conjunction with Multiple Mode Calorimetry (MMC) thermal safety tests. Cyclic Voltammetry (CV) and Electrochemical Impedance Spectroscopy (EIS) analysis were carried out between 0.01 and 2.0 V at 0.1 mV s^{-1} and 1 MHz to 10 mHz at 25 °C, respectively. During the CV tests, shown in Fig. 2.5-A, oxidation peaks were observed at 0.2, 0.25, and 0.48 V and a reduction

peak at 0.16 V. The 0.2 V peak is characteristic of graphite delithiation. Numerous scientific reports reveal delithiation of Si happens via two peaks below 0.5 V.[24-26]

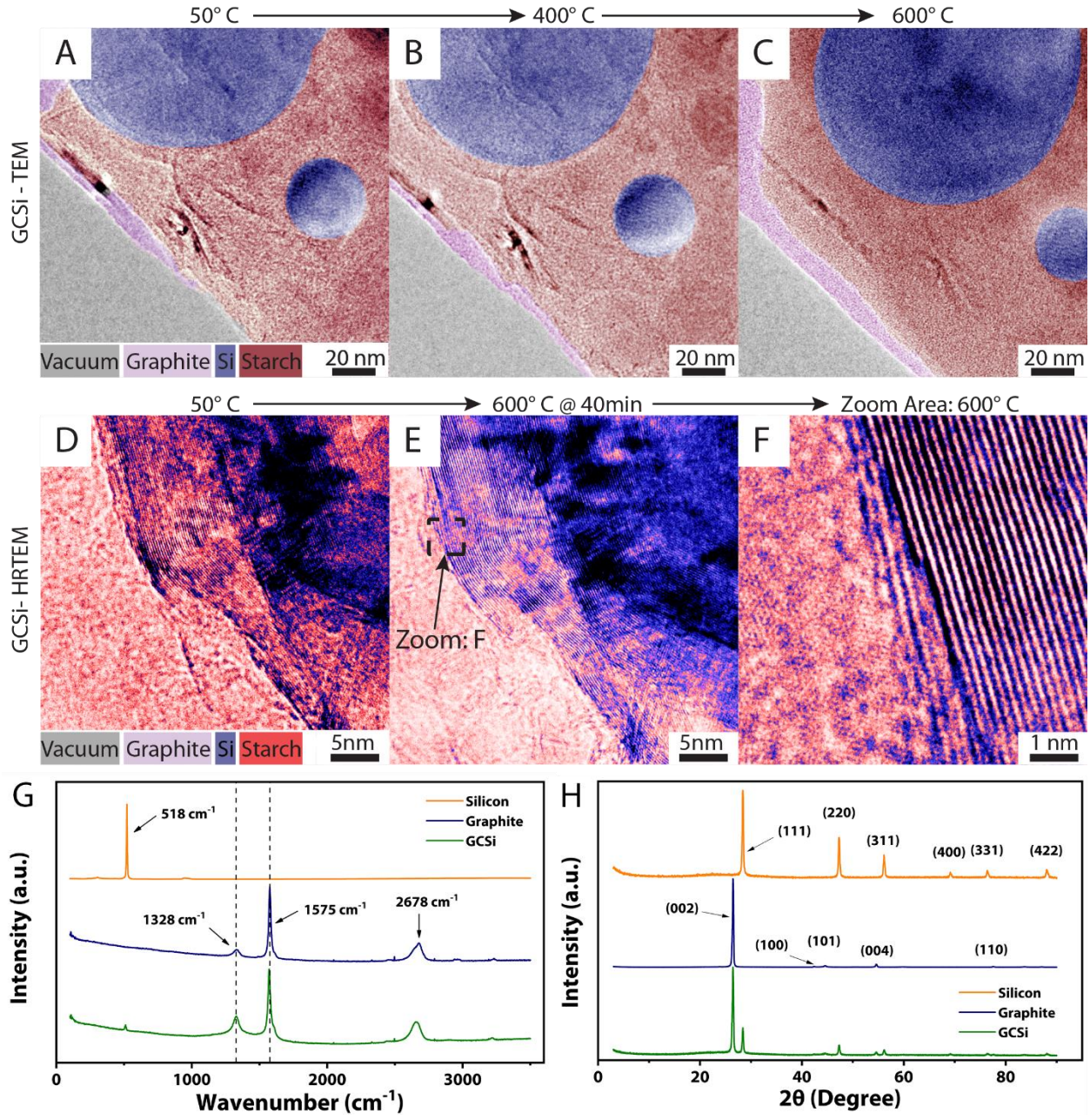

Figure 2.4: TEM micrograph of composite anode material transformation. A: Initial mixture of disordered starch, graphite, and Si particles over the vacuum. B: At 400 °C the starch is seen shrinking and carbonizing C: At 600 °C, the starch is almost fully converted to a continuous amorphous sheet. D: High-resolution micrograph of the highly disordered interface between Si and starch. E: The following heating at 600 °C, the starch is uniform, and the interface has merged. F: HRTEM shows the amorphous aromatic carbon next to the Si atomic planes. G: Raman Spectra of graphite, silicon, and GCSi. H: XRD patterns of graphite, silicon, and GCSi

Here, two characteristic peaks are observed at 0.25 V and 0.48 V. Notably, during the reduction process the active species response for Si and graphite, merged together and revealed itself as a single reduction peak at 0.16 V. The formation of the solid electrolyte interface (SEI) also occurs gradually, with a shoulder developing from 0.12V to 0.35V.[26-28] Since Si-NPs are coated with a network of carbon, there are no sharp SEI peaks at 0.4 V, implying there is suppressed SEI formation on this novel composite anode.

Figure 2.5-B shows voltage profiles for GCSi composite cycled at 50 mA g^{-1} for the initial two cycles followed by 500 mA g^{-1} for the rest of the cycles. The presence of silicon and carbon causes two lithiation and delithiation plateaus in the profile. Silicon and graphite lithiates around 0.2 V and 0.1 V, and they delithiates around 0.44 V and 0.2 V, respectively. The sloping behavior arises due to the presence of amorphous carbon in the composite. Interestingly, most of the capacity is obtained below 1.5V, this is very important for the ideal industrial anodes. Figure 2.5-C shows rate studies of GCSi anode composite indicating the gravimetric capacities. Multiple rate galvanostatic cycling of the cell are exhibited at different rates between 50 mA g^{-1} to 1000 mA g^{-1}. GCSi exhibits a high capacity of about 980, 960, 890, 705, and 610 mAh g^{-1} at current densities of 50, 100, 200, 500, and 1000 mA g^{-1}, respectively. This is much higher when compared to that reported for commercial graphite. Etacheri *et. al.* reported capacities of 330, 250, 70 mAh g^{-1} at current densities of C/10, C/5, and 1C for commercial graphite material.[29] Hence, we see the composite provides much robust and high specific capacities compared to commercial graphite.

In Fig. 2.5-D, an ideal Nyquist plot of LIBs shows two semicircles with 45° linear drift of diffusion. The first high-frequency semicircle is due to the formation of SEI film and the middle frequency semicircle is due to charge transfer resistance at the interface of electrode and electrolyte and double-layer capacitance.[30] The straight line indicates the diffusion of lithium ions. For a better understanding of the composite system, EIS was performed on the fully delithiated cell. As shown in Fig. 2.5-D, the series resistance (R_s) for the freshly constructed cell was 2.5Ω, which remained consistent even after the 1st cycle. As the cycles progressed, the Rs increased due to conductivity loss, which arises mainly due to either current collector corrosion or binder decomposition, leading to additional impedance.[31] The Rs after 100th cycle was 5.8Ω. The charge transfer resistance (R_{CT}) for the first cycle was found to be 21Ω, whereas after 10th cycle it was 12Ω. After 100th cycle, the charge transfer resistance was 14Ω. The initial reduction in charge transfer resistance is observed mainly because the volume expansion of silicon causes a build-up

of stress inside the electrode.[32] Such phenomena lead to the formation of well-developed pores in the electrode and better contact between particles, and current collector facilitating the better charge movement across the electrode. After 100 cycles, there is a slight increase in R_{CT}, which arises due to possible stress in the overall electrode that might have developed from continuous long cycling of the electrode.[32, 33] However, in the current scenario, the presence of an amorphous carbon network around Si-NPs prevents them from delaminating. Hence, a significant increase in R_{CT} is not observed, thus explaining the importance of tortuosity in the electrodes.[33]

As shown in Fig. 2.5-E, the first-cycle gravimetric discharge capacity of GCSi composite was 1126 mAh g^{-1} with a high coulombic efficiency of 83%. This is higher compared to 78.3%,[34] 80.3%,[35] and 79.9%[36] recently reported in the literature for silicon anodes. There is an initial, irreversible capacity loss of 284 mAh g^{-1}. The main cause of this initial capacity fade is the formation of an SEI layer on the composite anode.[37, 38] The 1st and 2nd cycles are formation and stabilization cycles. During these two cycles, the applied current is 50 mA g^{-1} and helps in stable SEI formation and proper structural network development of the composite. After the completion of the first two cycles, the GCSi electrode demonstrates highly stable electrochemical performance at a higher current density of 500 mA g^{-1}. GCSi shows an average discharge capacity of 540 mAh g^{-1}.

For a bare silicon electrode, there is a huge capacity fade mainly due to the unstable SEI layer, which depletes the available lithium ions. However, in the presence of a protective carbon cage around Si-NPs further strengthened by graphite particles, issues of pulverization and delamination are reduced to a greater extent. Loss of lithium ions is prevented inside the system, which helps in achieving high capacity for GCSi. One thing to be noted is that the tremendous volume change of Si-NPs during lithiation can sometimes lead to an inevitable volume change of the carbon shell. This induces cracks on the carbon shell and exposes Si to the electrolyte causing SEI layer formation and a breakdown of the electrode structure.[39] Hence, bolstering the Si-NPs-carbon network setup with graphite particles provide excellent mechanical property to the electrode. Eventually, it also suppresses the volume expansion of the core Si, so as to form a more stable interface between particles and minimize cracking and fracturing of the SEI layer.

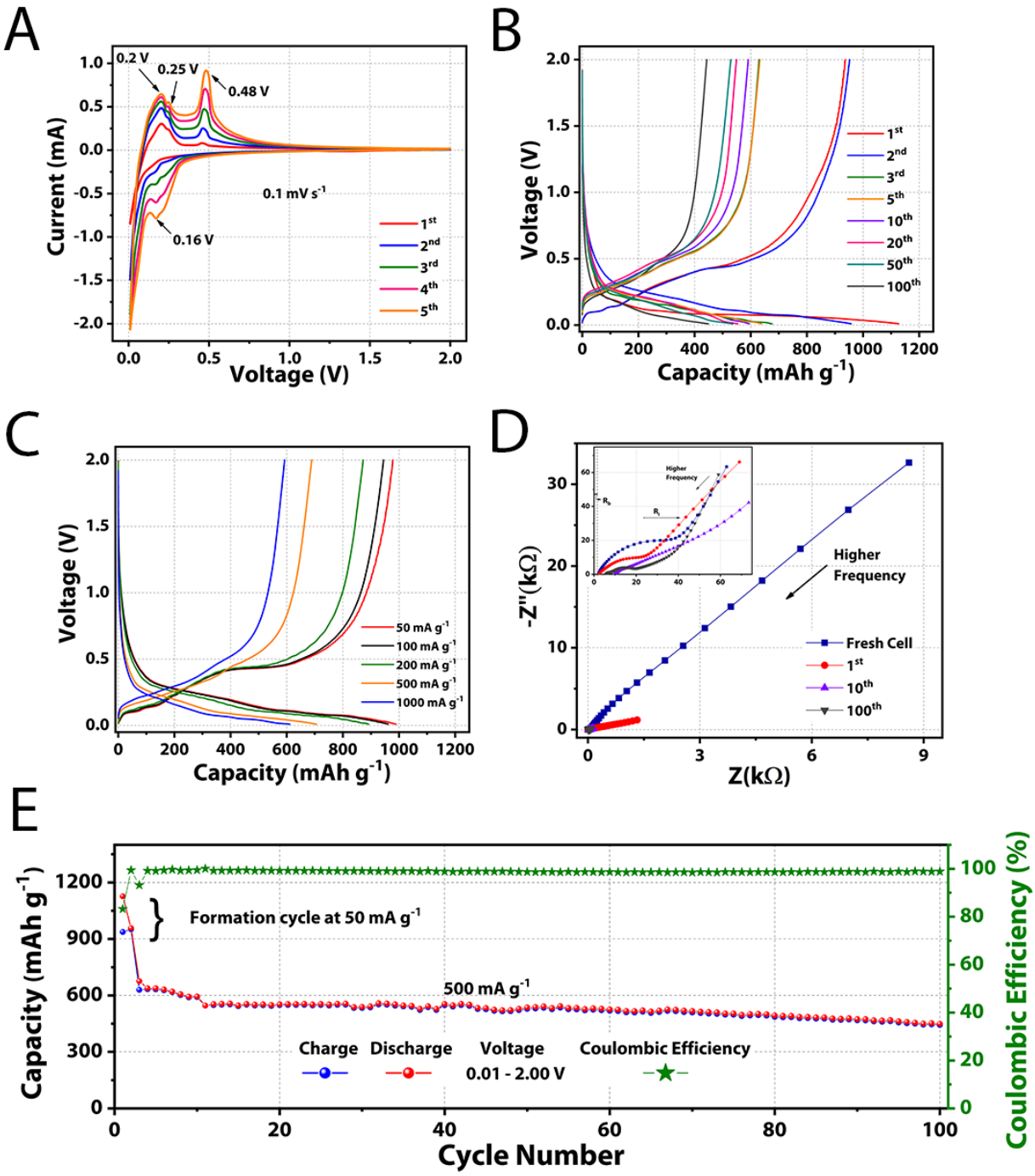

Figure 2.5: Electrochemical characterization of the synthesized GCSi composite A: CV curves of the first five cycles obtained at 0.1 mV s^{-1} in the range of 0.01 – 2.0 V. B: Voltage profiles for 1st to100th cycle. C: The corresponding rate performance. D: The changes in the electrochemical impedance before and after activation and after 100 cycles at 500 mA g^{-1}. E: Charge–discharge cycling test of GCSi electrode at a current density of 500 mA g^{-1}

The thickness of the pristine electrodes was measured using a thickness gauge (Mitutoyo). The thickness of graphite, G-Si, and GCSi on an average were found to be 36.78, 34.43, and 37.23 μm. As shown in Fig. 2.6, the cross-sectional view of electrodes was observed by SEM to directly compare the length change of each electrode before and after lithiation. As shown in Table 2, for graphite, G-Si, and GCSi, we observed 10%, 35%, and 19% increase in the height of the electrode, respectively. The G-Si showed the largest change in the height amongst all the electrodes, which is even larger than the GCSi electrode. This result directly supports that the starch-derived carbon in the GCSi composite helps to suppress the volume change of the G-Si electrode and thus leads to stable electrochemical performance.

Table 2.1: Percent change in the height of electrodes

Sample	Lithiated Thickness (μm)	Delithiated Thickness (μm)	% Change
Graphite	41.08	37.17	10.52%
G-Si	47.61	35.22	35.18%
GCSi	45.02	37.82	19.03%

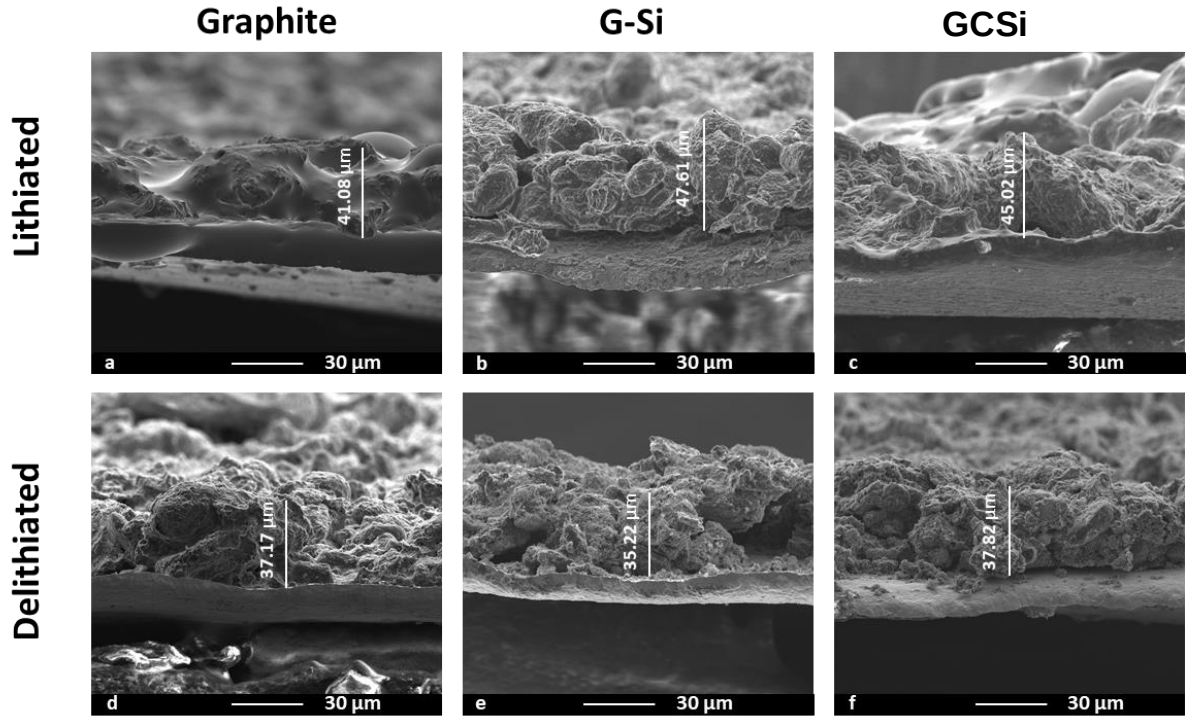

Figure 2.6: Cross-sectional SEM images of graphite, G-Si, and GCSi electrodes after lithiation and delithiation.

To benchmark, the cell stability, and thermal safety, multiple CR-2032 coin cells were prepared using GCSi anode, reference graphite anode, lithium cobalt oxide cathode, polypropylene separator with 5% FEC (v/v) with 1M $LiPF_6$ dissolved in 1:1 EC:DEC electrolyte in full-cell configuration to conduct multiple module calorimetry (MMC) studies. Typically, researchers use Differential Scanning Calorimetry (DSC) to study SEI breakdown chemical reactions, electrolyte salt decomposition, the reaction of electrolyte with an electrode material, and the thermal properties of the materials.[3, 40] However, the scale of operation (sample size) is very small (milligrams), and it could generate some artifacts. Hence, for a better understanding of the dynamics of the batteries, there is a requirement for more sophisticated characterization systems. MMC creates a synergy of DSC and Accelerated Rate Calorimetry (ARC) wherein it measures chemical reactions, specific heat phase changes like a DSC and, runs adiabatic tests to check process safety analogous to an ARC. The major difference is the size of the operation (i.e. MMC can perform these tests on gram-size samples and on whole coin cells). Also, MMC can easily be plugged into an external battery cycler and used for isothermal cycling to check performance under different charge-discharge rates. The heat flux during cycling can be measured with high accuracy to determine cell efficiency for different battery chemistries. The MMC's unique capabilities allowed the *in-situ* study of thermal runaway and the measurement of heat changes during electrochemical reactions of the cells.

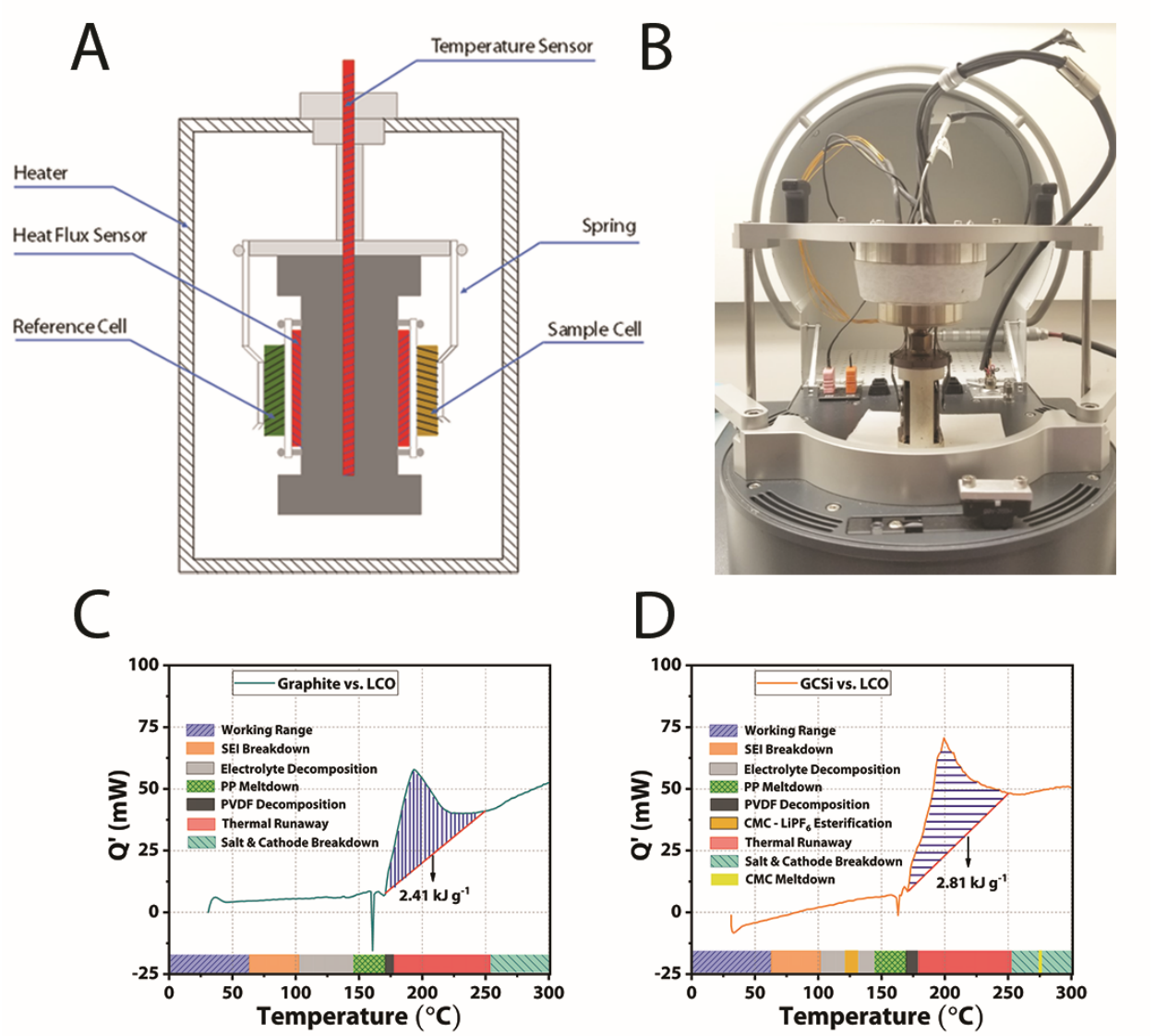

Figure 2.7: Multiple Mode Calorimetry studies A: Schematic depicting MMC Instrument. B: Actual Photograph of MMC. C: Graphite with lithium cobalt oxide cathode in full cell configuration data. D: GCSi with lithium cobalt oxide cathode in full cell configuration data.

For studying the thermal behavior of the different materials in a typical LIB, the cells were cycled at 20 mA g^{-1} between 0.01 V to 2.0 V, near the anode theoretical max capacity values. The cells were charged to 100% SOC before initiating calorimetry studies; heating from room temperature till 300 °C at the rate of 0.5 K min^{-1}. Temperatures below 300 °C are critical for the initiation of the thermal runaway event and hence are of primary focus in the current study.[41] Figure 2.7-A shows the schematic of MMC. It consists of a chamber in which the sample coin cell

is tested against a reference cell. The chamber also contains a temperature sensor and a heat flux sensor. The whole chamber is surrounded by a heater for conducting a variety of experiments such as isothermal cycling, calorimetry, etc. The actual photograph of the MMC is shown in Fig. 2.7-B. Multiple mode calorimetry data for graphite and GCSi electrodes when coupled in full cell configuration, respectively is shown in Fig 2.7-C & D. 25°C is considered as the optimal working temperature for batteries and 60 °C being the upper threshold for functioning. Around 80°C, the SEI layer starts degenerating and decomposing and the exotherm slope begins as shown in Fig. 2.7-A & B. Around 110 – 130 °C, electrolyte breakdown occurs and generates gases inside the cell.[42] Also, there is an exothermic esterification reaction between CMC binder with $LiPF_6$ around 125 °C.[41] The system remains stable until the polypropylene begins to melt causing an internal short circuit. It is observed that between 155 – 165 °C there is an endothermic peak that results from the melting of the polypropylene (PP) separator and gasket of the coin cell.[43] Melting of the PP separator results in a short-circuited cell which leads to a thermal runaway situation. Around 170 – 175 °C, binder meltdown and reaction with lithiated material occurs,[44] generating very high exothermic peaks observed after 180 °C. Thermal runaway also results from a reaction between the electrolyte and intercalated Li inside the electrode material.[40] These exothermic peaks are observed between 180 – 250 °C. Above 200 °C, it has been reported that the electrolyte $LiPF_6$ salt melts, absorbing the heat supplied to it.[43, 45] CMC binder in composite electrode melts around 270 °C. As observed, a major contributor for initiation of thermal runaway situation comes from anode, electrolyte, and separator however, with temperature rise, the delithiated cathode contributes towards the sustenance of runaway condition. As Li is removed from the lattice of LCO, it increases the oxidation potential, causing more solvent decomposition at the solvent-crystal interface. Also, it leads to a high possibility of PVDF polymer-solvent interaction.[44] These phenomena are observed above 200 °C.[44]

From the obtained plots for the graphite and GCSi anode in full cell configuration, the energy released per specific capacity of the cell during the thermal runaway event was determined. From multiple cells tested, about 2.41 kJ g^{-1} of heat is released from graphite anode, which is less than that of GCSi (2.81 kJ g^{-1}), during thermal runaway. One crucial observation is the change in the thermal runaway onset. There is a single broad exothermic peak for graphite, which appears around 194 °C. In the case of GCSi anode, exothermic peaks are observed at 194 °C and 200 °C. Also, there is a slight delay in the onset of the main thermal runaway event in the composite compared

to graphite.[45] Comparing the energy released per specific capacity of the full cell, it is found that GCSi was 20.89 kJ Ah^{-1} compared to 21.56 kJ Ah^{-1}. The heat released from the composite is lesser than the heat released by graphite material. Possible reasoning for lower heat generation for composite is that lithium is stored in graphite in the form of LiC_6, where the electron cloud exists above the carbon ring structure. The bonding between lithium atoms in graphite is loose compared to that in Si, where they are bonded in form of alloy, which has stronger bonds. Removal of Li (delithiation) from Li_xSi occurs at a higher potential ~ 0.44 V vs Li/Li^+ compared from Li_xC_6, which is ~0.15 V. Study by Jiang and Dahn has shown that this should lead to ~10% lesser enthalpy reaction for the reaction of electrolyte with lithiated silicon compared to graphite.[45] Secondly, amorphous carbon due to the absence of long-range graphitic boundaries is not susceptible to exfoliation by electrolyte intercalation. It is shown to be used as a potential Li^+ storage material at a higher temperature compared to graphite anodes, which have SEI decomposition at a temperature beyond 60- 80 ºC.[46] Mainly, silicon has a buildup of thicker LiF layer and other reaction products on its surface and for similar capacities, silicon composite will have lesser contact area with electrolyte, which leads to slower reaction.[46] It is also reported that compared to conventional graphite with similar moles of lithium, the lithiated silicon shows lower reactivity between 100 and 350 ˚C.[41, 46, 47] This suggests that the synergistic effect of each ingredient of the composite results in lowering the exothermic heat released during thermal runaway reactions. It appears that the composite material is slightly safer to use as a battery anode compared to the age-old graphite material.

2.5 Conclusion

The field of batteries does not follow Moore's Law,[48] however, with the rise in demand for high performance, new electrode materials are required which can deliver enhanced energy density, safety, and stability. A new composite anode material, containing 25 wt % Si-NPs interfaced to graphite with starch-derived carbon is proposed. To overcome the early life capacity losses which are associated with the swelling behavior of silicon, the composite is annealed at 600 °C for 120 minutes. This annealing step, observed by *in situ* ETEM, helps in homogenizing the composite structure, encapsulating the silicon nanoparticles, and binding the nanoparticles to the bulk of the graphite. The designed GCSi composite architecture delivered a high initial capacity of 1126 mAh g^{-1} with a superior coulombic efficiency of 83%. After the formation cycles were completed, the

GCSi material delivered a capacity of 638 mAh g^{-1} and retained 448 mAh g^{-1} capacity at a current density of 500 mA g^{-1} after 100 cycles. This stable and high performance could be related to the well-entangled network of the starch-derived amorphous carbon, thereby imparting improved electrochemical kinetics and enhanced structural stability to the well-baked anode. This proposed approach of incorporating amorphous carbon into the silicon-graphite composites reduces the critical inherent issues of silicon electrodes and provides a dramatic boost in the storage capacity without the fall off and instabilities of the silicon anodes. Calorimetry studies performed indicate good cell stability, with a multiple-stage thermal runaway observed during testing. Overall, the heat generated from the use of composite as an anode was 20.89 kJ Ah^{-1} compared to 21.56 kJ Ah^{-1} from the graphite anode. This suggests it is an intrinsically safer, higher capacity anode material for battery systems compared to the commercially used graphite. However, this thermal performance study recommends that thermal stability is the critical issue that needs to be focused on before silicon becomes a viable substitute. In all, the GCSi composite offers high capacity, high stability, and safer material for the next generation of lithium-ion cells.

2.6 Acknowledgement

The authors acknowledge the Natural Sciences and Engineering Research Council of Canada (Award No. PGSD2-518773-2018) for their financial support of this project. All microscopy and characterization were performed at the Ontario Center for Characterization of Advanced Materials (OCCAM) at the University of Toronto. The authors would like to acknowledge Dr. Stas Dogel for their invaluable technical assistance with this project. The authors would also like to thank Hitachi Higher Technologies Canada, and Norcada Inc for their assistance with the *in-situ* microscopy studies. Authors acknowledges Davidson School of Chemical Engineering, Purdue University for their financial support in this project. Authors also, express their gratitude to the Office of Naval Research under NEPTUNE for supporting this work under the grant N00014-18-1-2397. Authors would also like to thank Kyungho Kim for his help with cross-sectional SEM imaging and Dr. Manikandan Palanisamy for his support and help throughout the experiments. Purdue authors thanks to NETZSCH company for MMC 274 Multi-Module Calorimeter with special technical support from Peter Ralbovsky and Peter Vichos.

2.7 References

1. M.M. Thackeray, C. Wolverton, and E.D. Isaacs, *Energy & Environmental Science* **2012**, 5(7).
2. G.E. Blomgren, *Journal of The Electrochemical Society* **2016**, 164(1): p. A5019-A5025.
3. R.A. Adams, A. Varma, and V.G. Pol, *Journal of Power Sources* **2019**, 410-411: p. 124-131.
4. S. Goriparti, E. Miele, F. De Angelis, E. Di Fabrizio, R. Proietti Zaccaria, and C. Capiglia, *Journal of Power Sources* **2014**, 257: p. 421-443.
5. U. Kasavajjula, C. Wang, and A.J. Appleby, *Journal of Power Sources* **2007**, 163(2): p. 1003-1039.
6. W.-J. Zhang, *Journal of Power Sources* **2011**, 196(1): p. 13-24.
7. J.-Y. Li, Q. Xu, G. Li, Y.-X. Yin, L.-J. Wan, and Y.-G. Guo, *Materials Chemistry Frontiers* **2017**, 1(9): p. 1691-1708.
8. M.J. Chon, V.A. Sethuraman, A. McCormick, V. Srinivasan, and P.R. Guduru, *Phys Rev Lett* **2011**, 107(4): p. 045503.
9. M. Nie, D.P. Abraham, Y. Chen, A. Bose, and B.L. Lucht, *The Journal of Physical Chemistry C* **2013**, 117(26): p. 13403-13412.
10. H. Wu and Y. Cui, *Nano Today* **2012**, 7(5): p. 414-429.
11. N. Dimov, S. Kugino, and M. Yoshio, *Electrochimica Acta* **2003**, 48(11): p. 1579-1587.
12. P. Zuo, G. Yin, and Y. Ma, *Electrochimica Acta* **2007**, 52(15): p. 4878-4883.
13. T. Zhang, L. Fu, J. Gao, L. Yang, Y. Wu, and H. Wu, *Pure and Applied Chemistry* **2006**, 78(10): p. 1889-1896.
14. R. Zhou, H. Guo, Y. Yang, Z. Wang, X. Li, and Y. Zhou, *Journal of Alloys and Compounds* **2016**, 689: p. 130-137.
15. X. Li, M. Wu, T. Feng, Z. Xu, J. Qin, C. Chen, C. Tu, and D. Wang, *RSC Adv.* **2017**, 7(76): p. 48286-48293.
16. M. Singh, J. Kaiser, and H. Hahn, *Journal of The Electrochemical Society* **2015**, 162(7): p. A1196-A1201.
17. A.D. Sediako, C. Soong, J.Y. Howe, M.R. Kholghy, and M.J. Thomson, *Proceedings of the Combustion Institute* **2017**, 36(1): p. 841-851.
18. K. Pielichowski and J. Njuguna, *Thermal degradation of polymeric materials*. **2005**: Rapra Technology Limited.

19. Z.-J. Fan, W. Kai, J. Yan, T. Wei, L.-J. Zhi, J. Feng, Y.-m. Ren, L.-P. Song, and F. Wei, *ACS Nano* **2011**, 5(1): p. 191-198.
20. B. Kartick, S.K. Srivastava, and I. Srivastava, *J Nanosci Nanotechnol* **2013**, 13(6): p. 4320-4.
21. V.G. Pol and M.M. Thackeray, *Energy Environ. Sci.* **2011**, 4(5): p. 1904-1912.
22. J.H. Parker, D.W. Feldman, and M. Ashkin, *Physical Review* **1967**, 155(3): p. 712-714.
23. W. Ren, Y. Wang, Z. Zhang, Q. Tan, Z. Zhong, and F. Su, *Journal of Materials Chemistry A* **2016**, 4(2): p. 552-560.
24. Z. Sun, S. Tao, X. Song, P. Zhang, and L. Gao, *Journal of The Electrochemical Society* **2015**, 162(8): p. A1530-A1536.
25. J. Tang, A.D. Dysart, D.H. Kim, R. Saraswat, G.M. Shaver, and V.G. Pol, *Electrochimica Acta* **2017**, 247: p. 626-633.
26. M.H. Parekh, V.P. Parikh, P.J. Kim, S. Misra, Z. Qi, H. Wang, and V.G. Pol, *Carbon* **2019**, 148: p. 36-43.
27. K. Yang, Z. Yu, C. Yu, M. Zhu, L. Yang, H. Chen, and F. Pan, *Energy Technology* **2019**, 7(7).
28. V. Etacheri, C.N. Hong, and V.G. Pol, *Environ Sci Technol* **2015**, 49(18): p. 11191-8.
29. R.A. Adams, J.M. Syu, Y. Zhao, C.T. Lo, A. Varma, and V.G. Pol, *ACS Appl Mater Interfaces* **2017**, 9(21): p. 17872-17881.
30. C. Pastor-Fernández, K. Uddin, G.H. Chouchelamane, W.D. Widanage, and J. Marco, *Journal of Power Sources* **2017**, 360: p. 301-318.
31. Q. Huang, M.J. Loveridge, R. Genieser, M.J. Lain, and R. Bhagat, *Scientific Reports* **2018**, 8(1): p. 1386.
32. J. Landesfeind, M. Ebner, A. Eldiven, V. Wood, and H.A. Gasteiger, *Journal of The Electrochemical Society* **2018**, 165(3): p. A469-A476.
33. T. Ma, H. Xu, X. Yu, H. Li, W. Zhang, X. Cheng, W. Zhu, and X. Qiu, *ACS Nano* **2019**, 13(2): p. 2274-2280.
34. X. Dou, M. Chen, J. Zai, Z. De, B. Dong, X. Liu, N. Ali, T. Tadesse Tsega, R. Qi, and X. Qian, *Sustainable Energy & Fuels* **2019**, 3(9): p. 2361-2365.
35. F. Zhang, G. Zhu, K. Wang, X. Qian, Y. Zhao, W. Luo, and J. Yang, *Journal of Materials Chemistry A* **2019**, 7(29): p. 17426-17434.

36. Y.E. Eli, *Electrochemical Solid-State Letters* **1999**, 2: p. 212.
37. E. Peled, *Journal of The Electrochemical Society* **1979**, 126: p. 2047.
38. Y. Jin, B. Zhu, Z. Lu, N. Liu, and J. Zhu, *Advanced Energy Materials* **2017**, 7(23).
39. R.A. Adams, A. Varma, and V.G. Pol, *Journal of Power Sources* **2018**, 375: p. 131-137.
40. I.A. Profatilova, T. Langer, J.P. Badillo, A. Schmitz, H. Orthner, H. Wiggers, S. Passerini, and M. Winter, *Journal of The Electrochemical Society* **2012**, 159(5): p. A657-A663.
41. G. Gachot, S. Grugeon, G.G. Eshetu, D. Mathiron, P. Ribière, M. Armand, and S. Laruelle, *Electrochimica Acta* **2012**, 83: p. 402-409.
42. Q. Wang, P. Ping, X. Zhao, G. Chu, J. Sun, and C. Chen, *Journal of Power Sources* **2012**, 208: p. 210-224.
43. E.P. Roth and G. Nagasubramanian, *Journal of the Electrochemical Society* **2000**: p. SAND2000-0345J.
44. Q. Wang, J. Sun, X. Chen, G. Chu, and C. Chen, *Materials Research Bulletin* **2009**, 44(3): p. 543-548.
45. H. Zheng, Q. Qu, L. Zhang, G. Liu, and V.S. Battaglia, *RSC Advances* **2012**, 2(11).
46. Q. Wang, J. Sun, X. Yao, and C. Chen, *Thermochimica Acta* **2005**, 437(1-2): p. 12-16.
47. F. Schlachter, *Proc Natl Acad Sci U S A* **2013**, 110(14): p. 5273.

3. RESERVE SECONDARY BATTERIES: NOVEL CONFIGURATION FOR LITHIUM-ION BATTERIES FOR MULTIPURPOSE APPLICATIONS

Mihit H. Parekh, Manikandan Palanisamy, Vilas G. Pol

This work is under peer-review process. The conceptualization and electrochemical testing were carried out by Mihit H. Parekh and Dr. Manikandan Palanisamy. Characterizations and manuscript preparation were performed by Mihit. H. Parekh.

3.1 Overview

One of the major challenges in the development of next-generation lithium-ion batteries is the discrepancy in the capacity between electrodes. Vanadium pentoxide is recognized as a potential candidate for cathode owing to attractively high theoretical capacity. Due to the lack of Li^+ ions in its crystal lattice, V_2O_5 has always remained far away from practical realization. Various strategies viz., pre-lithiation, blended cathodes have been studied for Li^+ ion free cathodes with no commercial interests. We report the development of reserve lithium-ion batteries (RLIBs) for Li^+ ion free V_2O_5 cathode with graphitic anode, which delivered a high charge capacity of 264 mAh g^{-1}, attained by the in-situ lithiation process. Through the different operational modes of RLIB, the V_2O_5 cathode's intrinsic voltage characteristics with MCMB anode were achieved during the full-cell cycling studies. The mechanistic elucidation of RLIBs has been conducted using impedance spectroscopy and boundary conditions of Fick's law of diffusion could be observed in the different modes. Pouch cell configuration exhibited stable cycling performance for 300 cycles at 0.5C rate. The development of the RLIBs offers the potential to unlock the usage of various Li^+ ion free cathodes viz., vanadium oxides, sulfur, FeS_2, MnO_2, etc. for the realization of high capacity and energy-dense applications.

3.2 Introduction

Lithium-ion batteries, a Nobel Prize-winning technology has been hailed as a contender to meet the energy expectations for a sustainable world.[1] The sales of electric vehicles have skyrocketed from 2011 to 2020 by almost 20 times, which implies tremendous demand for lithium-ion batteries (LIBs).[2] With the demand, the cost of cobalt, one of the critical elements of the cathode, has doubled in the same period. To keep up with the growing demand and economic

feasibility, shortcomings of LIBs need to be addressed, which can be majorly attributed to the cathode and architecture of the batteries.[3] Troubleshooting these two challenges would bring about a synergistic effect on the key parameter of batteries: *Energy Density*. With better development of cathode and anode materials, the LIBs' energy density has improvised from 80 Wh kg^{-1} (1990) to presently, 300 Wh kg^{-1}.[4] However, EVs demand even higher energy densities than 500 Wh kg^{-1}, at the cell level. To enhance energy density of the conventional LIBs, we replenished the Li^+ ions losses that incur due to solid electrolyte interface (SEI) formation using lithium replenishment electrode and achieved a high energy density of 455 Wh kg^{-1}.[5] Next-generation batteries are being developed with Li-sulfur, Li-air chemistries, and safer solid-state batteries with lithium metal to tackle this herculean task. Various lithium-rich cathodes with high specific capacity have been developed viz., $Li[Li_{0.2}Ni_{0.2}Mn_{0.6}]O_2$, $Li_4Mn_2O_5$, $Li_{1.2}Ni_{0.15}Co_{0.1}Mn_{0.55}O_2$, etc. [6-8] The irreversible formation cycle capacity loss, poor rate capabilities, and capacity decay, and potential drop during cycling keep such materials from practical use. High voltage nickel-rich cathodes ($LiNi_xMn_yCo_{1-x-y}O_2$, $x \geq 0.5$) have been developed as they have high discharge capacity (~220 mAh g^{-1}) and increased energy density (~800 Wh kg^{-1}). However, these materials tend to convert to spinel (cycled between 3.0–4.5V) and cubic (cycled between 3.0–4.8 V) phases, which are lithium-deficient, ion-insulating and releases O_2 into the system, leading to unsafe environment for batteries. Also, on excess delithiation (>70%) leads to surface reconstruction resulting in cation mixing and reduction in Li^+ insertion sites. At higher voltages, due to electrolyte decomposition acidic components are released that aggravated NMC dissolution. This pose a threat for anode of electrodeposition, for electrolyte of solvent reduction via catalysis, and for growth of resistive inorganic SEI layer.[9] At the expense of high capacity and energy density, these materials suffer from severe capacity attenuation and structural instability. These developments are still in their primitive years and have years of research left in them before which they can be commercialized. Hence, there is a need for a higher capacity cathode material with the capability to insert multiple lithium ions.

Vanadium pentoxide (V_2O_5) is one such material that has garnered huge attention in diverse fields including LIBs, supercapacitors, catalysis, flow batteries, and electrochromic devices. It is one of the promising cathode materials because of its rich chemistry, high capacity, economical value, morphology, crystallinity, and facile synthesis techniques.[10] The presence of layered structure induces high interlayer spaces, which enables Li^+ ions distribution and mobility. Being

cathode material, it theoretically delivers a high capacity of 294 mAh g^{-1} with de-/intercalation of 2 Li^+ ions, much higher compared to conventional $LiCoO_2$, $LiCo_xMn_yNi_zO_2$ (x+y+z = 1), and $LiFePO_4$.[11, 12] Also, V_2O_5 has a higher energy density of >800 Wh kg^{-1} compared to the conventional, Li-rich, Ni-rich, and Mn-rich cathodes.[6, 8, 13, 14] The V_2O_5 cathode has been synthesized with different types of morphologies, which have shown it to be promising cathode material for LIBs.[15-17] Compounds without lithium in their lattice rarely have been used as positive electrodes in lithium-ion full-cells due to the requirement of Li^+ ion for the charge-discharge cycling process. V_2O_5 cathode is as such lithium-ion free system i.e., does not contain Li^+ ions in its structure, and this prevents its practical usage in a full-cell application, although it provides higher energy density (>800 Wh kg^{-1}) than the other cathode system. This formidable hindrance will prevail as long as the growth of dendrites from lithium metal anode lingers around. Thus, the insertion of lithium into V_2O_5 cathode is inevitable in order to achieve high capacity and an energy-dense lithium-ion battery.

There is an urgent requirement for the development of a facile technique to supplement Li^+ ion to the lithium-free cathodes such as V_2O_5, sulfur, MnO_2, CuF_2, FeS_2, FeF_3, etc with the graphitic anode.[4, 18, 19] These materials demonstrate tremendously high specific capacities and high operating voltages for possibly realizing advanced next-generation batteries. To practically realize them, it is pertinent to address the lithiation strategies, namely pre-lithiation of the anode, and blended cathodes.[20, 21] These methods result in modification of cell voltage on account of Li^+ ion voids in the cathode, whereas pre-lithiation of anode compensates initial consumption of Li^+ ions. Nonetheless, the pre-lithiation procedure is a distinct technique associated with the complicated, multistep, moisture-sensitive, and expensive process, which are not feasible in commercial applications. Thus, the development of *in situ* lithiation of cathode or anode is required to unlock longer lasting, and energy dense rechargeable batteries.

There is a class of batteries called '*Reserve Batteries*', which uses a highly active component in the batteries that is isolated from the remainder until upon activation. During the inactive period, chemical reactions between the components are prevented and the cell is capable of long-term storage. Reserve design is typically activated by adding the missing part just before the usage. Some examples of such types are: Electrolyte-, Gas-, Heat-, and Water-activated batteries.[22] Based on our understanding of the reserve batteries and multi-Li^+ ions insertion

cathodes, lithium, a valuable resource, can be made to reserve inside the battery and activated through a circuit upon the requirement of the system.

In this study, we report tailored architecture of Reserve Lithium-ion Batteries (RLIBs) for in situ lithiation of lithium-free/deficient cathode, comprising of V_2O_5, assembled full-cell with MCMB anode to realize high capacity, energy-dense LIBs. In situ lithiation of the electrodes is achieved using a lithium reservoir, which stays inactive for a major portion of the electrochemical cycling studies and prevents the development of dendritic crystals. This system is analogous to the reservoirs formed by dams, which restrict or allow the flow of water from them. The primary aim is to develop in situ full–cell of V_2O_5 cathode and MCMB anode for the progress of long lasting secondary batteries and unlock Li^+ ion free/deficient cathode chemistries. The electrochemical measurements of the architecture suggest excellent performance and the potential of facile scale-up for large commercial applications.

3.3 Experimental Methods

3.3.1 Materials and Characterizations

Commercial-grade electrode materials of MCMB (MSE Supplies), Vanadium Pentoxide (Sigma Aldrich), PVdF (Arkema), and C-65(TIMCAL) were used after preheating at 80 °C for 24 h in a vacuum oven. 1 M $LiPF_6$ electrolyte was used with the 1:1 volume ratio of ethylene carbonate (EC)/diethyl carbonate (DEC) solvents (Sigma Aldrich). Thermal Gravimetric Analyzer-i1000 of Instrument Specialists Inc. was used to determine materials' degradation temperature. The physical properties such as crystallinity and phase purity of MCMB and V_2O_5 were recorded using Rigaku SmartLab powder X-ray diffractometer having a Cu Kα radiation source and scanned from 10° to 90° 2θ, at the rate of 2° min^{-1}. Energy dispersive elemental Analyses of MCMB, and V_2O_5 electrode materials, and high-resolution scanning microscopy to capture the particle size, and morphology were visualized by Nova NanoSEM 200, a high-resolution scanning electron microscope.

3.3.2 Electrode preparation and cells assembly

RLIBs was constructed in CR-2032 coin cell configuration with a reservoir electrode, V_2O_5 cathode and MCMB anode. The V_2O_5 cathode and MCMB anode were prepared by doctor-blade

coating method with MTI laminate coating machine. For cathode, the slurry consisted of 70% V_2O_5, 20% SuperP and 10% PVdF, dissolved in N-methyl-2-pyrrolidone (for anode, 80% MCMB, 10% SuperP and 10% PVdF), homogeneously mixed using Thinky mixer at 2000 rpm, coated on aluminum foil (12 µm thickness) for cathode, Cu foil (9 µm thickness) for anode. The electrodes were dried out at 80 °C under vacuum for 24 h and then calendered. The average active loading weights of cathode ~5.5 mg (V_2O_5), and anode ~3.3 mg (MCMB) were used for half–cells. For full–cells, N/P ratio was kept at ~1.03 and cathode loading of ~5.5 mg was used. For RLIBs, porous Cu mesh was taken to coat MCMB for allowing Li^+ ion exchange through both the cathode and lithium electrode sides. All the electrodes size were in the range of ~14 mm diameter. Lithium foils used for half–cell and RLIBs were 14 mm diameter with the wt. of ~12 mg.

Half–cells of V_2O_5 and MCMB were prepared using lithium as the reference electrode. For the full–cell studies, MCMB anode cells were lithiated using reference lithium electrode and used with V_2O_5 cathode to assemble full–cells. The cells were assembled using 1 M $LiPF_6$ salt in 1:1 (v/v ratio) EC:DEC solvents and Celgard® poly propylene used as separator. For RLIBs, V_2O_5, double-sided MCMB and lithium electrodes were connected externally with smart-grid circuit. Each of the electrodes were separated from each other by polypropylene separator. All the cells were constructed inside the argon (99.998%) filled glovebox (NEXUS II Vacuum Atmospheres Co.) with H_2O and O_2 <1 ppm and <5 ppm concentration levels, respectively. RLIBs were prepared in pouch cell configurations similar to CR2032 coin cell. Loading for cathode and anode was 5.6 mg cm^{-2} and 5.8 mg cm^{-2}, respectively. Electrolyte was added about 0.3 µL mg^{-1}. Multiple half–cells, full–cells, and RLIBs were prepared, which yielded similar results with small deviation.

3.3.3 Electrochemical measurements

Electrochemical characterizations were conducted to the constructed CR-2032 cells, viz., cyclic voltammetry (CV), electrochemical impedance spectroscopy (EIS) and galvanostatic cycling studies. The Faradaic redox reactions were achieved through CV studies using half–cells of MCMB and V_2O_5, each scanned at 0.2 mV s^{-1} in the voltage range 0.01–1.5 V (Li/MCMB) and 2.0–4.0 V (Li/V_2O_5), respectively using Gamry-600 reference system for 5 cycles. EIS measurements were carried out by Gamry-600+ reference system and data were collected for half–cells, full cells, RLIBs. For RLIBs, there are three different modes of measurement viz., Li/MCMB, MCMB/V_2O_5, and Li/V_2O_5. 10 mV amplitude AC voltage perturbation was applied over frequency

range 1 MHz – 10 mHz. All the potentials mentioned are versus Li^+/Li. From EIS the kinetics features of Li^+ ions diffusion path and deintercalation/intercalation through the electrodes can be investigated with the fitted circuit components. Eventually, Galvanostatic discharge–charge studies have been conducted for the constructed CR 2032 cells using an BT2043 Arbin cycler at room temperature with different rates and voltage window. The RLIB discharge-charge cycling studies were performed by anode lithiation (RLIB–Li vs MCMB), full–cell (RLIB–MCMB vs V_2O_5) with a wide voltage range from 0.01 to 4.0 V at different rates (0.05C, 0.06 C, and 0.2 C).

3.4 Results and discussions

3.4.1 Modules of reserve lithium-ion batteries

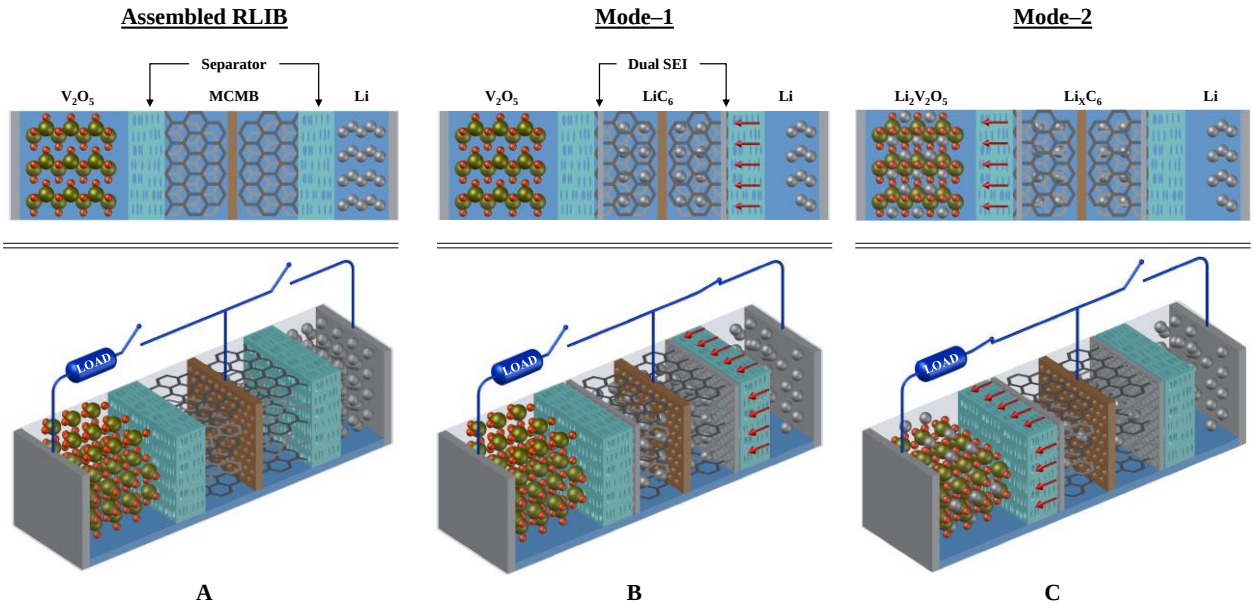

Figure 3.1: Different modes of RLIB (Top and Isometric views) A: Assembled RLIB, B: Circuit between MCMB and lithium electrode (Mode–1), and C: Circuit between lithiated MCMB anode and V_2O_5 cathode (Mode–2).

Thin lithium used as a reservoir electrode in RLIBs and provides Li^+ ions during pre-lithiation/formation cycles, as shown in Fig. 3.1. The operational modes of pre-lithiation (reservoir vs MCMB) and lithium-ion full-cell cycling studies (MCMB vs V_2O_5) are implemented as marked in Mode-1 and Mode-2. After assembling the RLIB (Fig. 1A), on the left is the vanadium pentoxide

cathode (Green-Red layered spheres), which is separated from MCMB anode by a polypropylene separator. MCMB anode (seen as hexagonal rings) is coated on Cu mesh current collector, which ensures the movement of Li^+ ions across the current collector. To the right of the anode is the reservoir lithium electrode (Silver spheres), which provides Li^+ ions as per the requirement to the system. MCMB anode is again separated from the lithium electrode by PP separator. The system is soaked in the electrolyte (light blue color) for the conduction of Li^+ ions. The circuit across the RLIB functions as a dam, which allows or restricts the flow of Li^+ ions from the lithium reserve electrode to the anode and cathode. During the 1st mode of operation, the MCMB anode is electronically connected to the reservoir lithium electrode (Fig. 3.1B). This allows for the movement of Li^+ ions from the reservoir to MCMB anode. Since, the MCMB anode has dual surface exposure, i.e., towards the cathode as well as the reservoir, dual solid electrolyte interface layer formation takes place on the surfaces of MCMB anode. During, this period, Li^+ ions are consumed from the reservoir in forming SEI layers as well as supplements for the lithium-free vanadium pentoxide cathode. Once the MCMB anode is lithiated, the reservoir is electronically disconnected from the system. Simultaneously, the V_2O_5 cathode is electronically connected to the lithiated MCMB anode for conventional cycling to extract work out of the system (Fig. 3.1C). There is possible scope for the replenishment of Li^+ ions, which comes into the act, once the capacity fade occurs beyond a tolerable limit. This simplistic novel architecture of RLIB can unlock various potential applications, which have not been realized by the conventional LIBs.

3.4.2 XRD and SEM Analysis of V_2O_5 cathode and MCMB anode

The phase purity and crystallinity of the V_2O_5 and MCMB were confirmed by the XRD patterns, as shown in Fig. 3.2A. All the diffraction peaks of V_2O_5 agree well with the standard spectrum of the pure orthorhombic V_2O_5 phase (JCPDS # 89-0612) and that of MCMB agree well with the spectrum of pure hexagonal graphitic phase (JCPDS# 00-008-0415) and no other impurities were present. Four stronger diffraction peaks, i.e., (001), (110), (301), and (200) were observed for the vanadium pentoxide powder. An intense peak (002) was observed for MCMB anode at 26.62°. Interplanar distances (d) for graphite particles are in the range of 3.35 Å – 3.44 Å and this was confirmed using Bragg's Law for 2nd order in the equation $n\lambda = 2d\sin\theta$. For λ = 1.54 Å (Cu-Kα radiation), interplanar distance turned out to be 3.44 Å. Another characteristic peak (004) was observed too. The morphologies of the V_2O_5 and MCMB were confirmed by FESEM

characterization. As seen in Fig. 3.2B, the fused layered structure of V_2O_5 can be observed, which offers favorable intercalation of Li^+ ions, making it a promising cathode material. The particles of V_2O_5 are irregular cubic aggregates typically 5–10 μm, as demonstrated in Fig. B.1 in Appendix B: Supporting Information (SI). The morphology of MCMB particles is flaky aggregated in nature and the average particle size distribution varies from 2–8 μm, as shown in Fig. 3.2C and B.1E, SI. The energy dispersive X-ray (EDX) spectra and elemental mapping reveal the presence of vanadium and oxygen without any other elements for the V_2O_5 cathode (Figure B.1B–D) and carbon in MCMB anode (Figure B.1F,G). The Brunauer Emmett Teller (BET) specific surface area of V_2O_5 was found to be 4.086 $m^2\ g^{-1}$ and MCMB was observed to be 1.84 $m^2\ g^{-1}$ (as shown in Fig. B.2). Porosity in the materials of RLIBs enhances the kinetics of redox reactions to a large extent.

The structure of vanadium pentoxide is atypical and comprises distorted trigonal bipyramids of VO_5 units sharing edges with others to form zig-zag double chains.[23] Vanadium pentoxide undergoes a phase transformation from V_2O_5 to $Li_xV_2O_5$ via the formation of α, ε, δ, γ, and ω depending on the number of electron transfer reaction. Table 3.1 below describes the phases formed upon intercalation of lithium into V_2O_5 interlayers. The phase ω is irreversible by nature, thus restricting the lithiation of the V_2O_5 to two Li^+ ions for practical application purposes. Beyond two ions lithiation, severe distortion occurs in the crystal structure, which must be stable in a typical cathode. Li^+ ions get hosted in the interlayers of V_2O_5 crystal structure shaped by the VO_5 octahedral unit cells.[24]

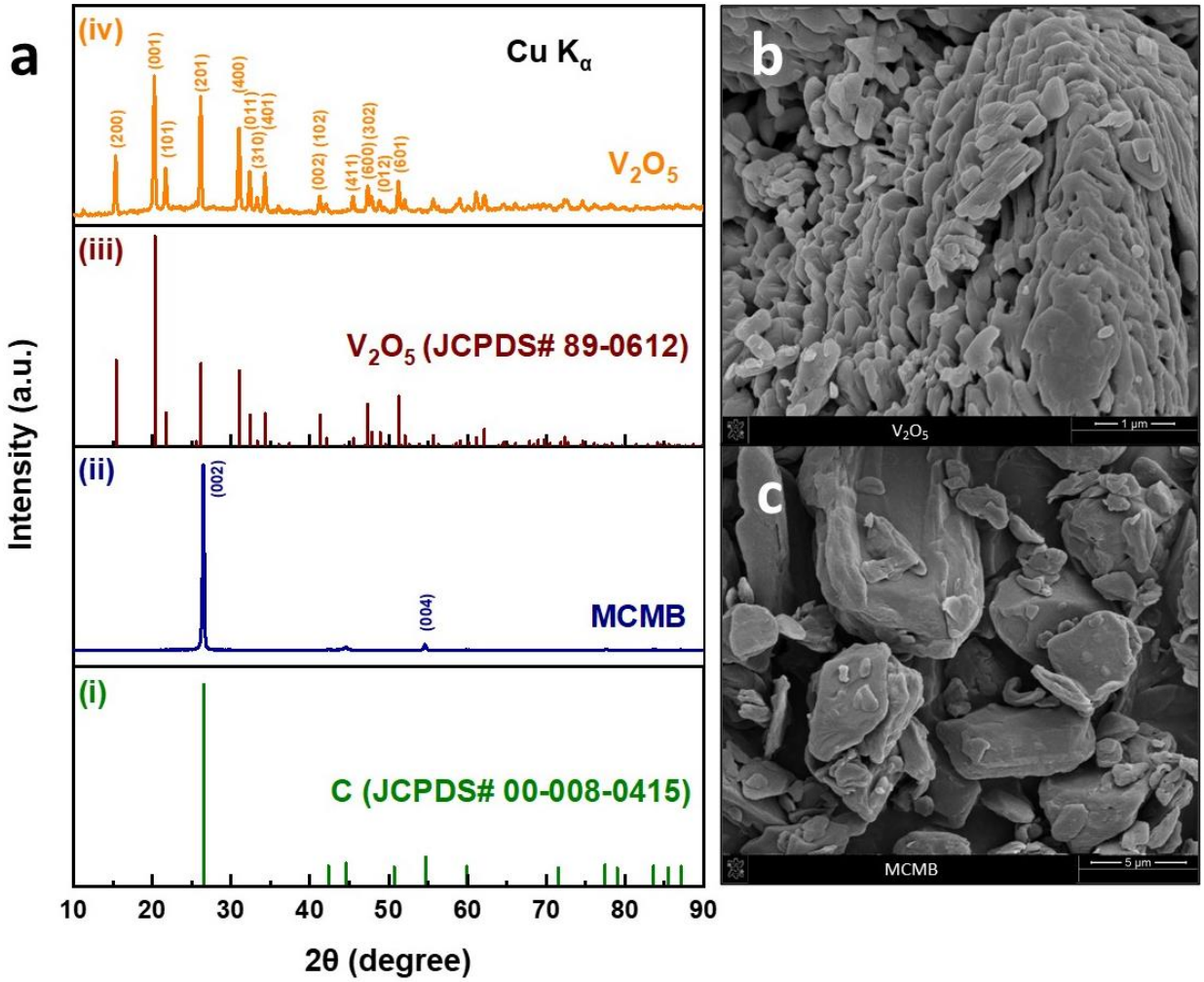

Figure 3.2: A: XRD patterns of MCMB (blue) and V_2O_5 (orange) compared with the standard XRD patterns of C, JCPDS# 00-008-0415 (wine), and V_2O_5, JCPDS# 89-0612 (green). FESEM images of B: V_2O_5 cathode material, and C: MCMB anode material.

Table 3.1: Phase formation resulting from multiple electron transfer reactions

Phase	**α**	**ε**	**δ**	**γ**	**ω**
'x' in $Li_xV_2O_5$	< 0.1	0.35 – 0.7	1	1 – 2	> 2

The advantage of V_2O_5 cathode over lithium iron phosphate (LFP) is in terms of the lithium migration pathways. V_2O_5 offers a 2D pathway compared to 1D of LFP for Li^+ ion diffusion and conductivity in the lithium plane. The lithiation process for the cathode can be understood from the reaction mechanism given below:

$$\alpha\text{–}V_2O_5 + 0.5\ Li^+ + 0.5\ e^- \rightarrow \varepsilon\text{–}Li_{0.5}V_2O_5 \quad (3.1)$$

$$\varepsilon\text{–}Li_{0.5}V_2O_5 + 0.5\ Li^+ + 0.5\ e^- \rightarrow \delta\text{–}LiV_2O_5 \quad (3.2)$$

$$\delta\text{–}LiV_2O_5 + Li^+ + e^- \rightarrow \gamma\text{–}Li_2V_2O_5 \quad (3.3)$$

$$\gamma\text{–}Li_2V_2O_5 + Li^+ + e^- \rightarrow \omega\text{–}Li_3V_2O_5 \quad (3.4)$$

Reactions 3.1 & 3.2 occur when voltage is restricted to 2.5 V during the lithiation process. Reaction 3.3 occurs when voltage is further brought down to 2.0 V. And <2.0 V, reaction 3.4 proceeds to form the irreversible, ω–phase.[25] These reactions can be clearly understood from the cyclic voltammogram (CV) recorded for Li vs. V_2O_5 half–cell between 2.0 V to 4.0 V at 0.2 mV s^{-1} (Fig. 3.3A). During the cathodic scan, multiple peaks occurred between 3.60 V to 2.95 V that signify the phase transformation from α– V_2O_5 → ε–$Li_{0.5}V_2O_5$ → δ–LiV_2O_5. Another peak appears at 2.18V, which signifies transformation from δ –LiV_2O_5 → γ–$Li_2V_2O_5$. Similar corresponding peaks were observed in the (de)lithiation process, during the anodic scan, which indicates excellent reversibility of electrode material. Though the peak intensities reduced, the positions and shape of the CV for subsequent cycles have remained similar, insinuating the stability of the material. It is important to indicate that cathodic electrolyte interphase (CEI) may have been formed on the surface of the V_2O_5 cathode due to the decomposition of carbonate solvents (EC/DEC). This may impede Li^+ ion diffusion into the active ingredients.[26]

Lithium anode in continuous cycling is known to form dendrites, which comes with associated challenges of low coulombic efficiencies, and safety risks of rupturing the separator to short-circuit the system causing thermal runaway event. This has impeded the usage of metallic lithium in the industrial battery market.[27] To avoid this condition, various other options are available at disposal viz., alloy-based negative anodes like Si, Ge, or Sn or conversion types viz., metal oxides (Fe_2O_3, Fe_3O_4, Co_3O_4), phosphides, sulfides, nitrides.[28, 29] However, with alloy-type materials, there is a critical issue of volumetric expansion during lithiation, which causes pulverization, delamination, SEI layer fragmentation, and Li^+ ions consumption. Conversion type anodes have issues of unstable SEI layer formation, poor cycle life, large potential hysteresis, and low capacity retention.[30] Thus, conventional graphite MCMB anode has been used for studying this novel architecture of RLIBs. Cyclic voltammograms of MCMB anode show the cathodic peak at 0.16 V and the anodic peak at 0.26 V, as depicted in Fig. 3.3B. During first-cycle discharge, a

small peak is observed around 0.7 V, which refers to the SEI layer formation due to the decomposition of carbonate solvents on the surface of anode material. The peak disappears after the first cycle indicating the formation of a stable SEI. This irreversible SEI layer is also the reason for energy loss in the first cycle i.e. low coulombic efficiencies. From the CVs of V_2O_5 (Figure 3.3A) and MCMB (Figure 3.3B), the chemical diffusion coefficients (D_{Li^+}) of Li^+ ions into the materials can be determined using Randles-Sevcik equation i.e.,

$$i_p = 0.4463\, nFAC \left(\frac{nF\nu D}{RT}\right)^{1/2} \tag{3.5}$$

where, i_p = current maximum in amps, n = number of electrons transferred in the redox event, A = electrode area in cm^2, F = Faraday Constant in C mol^{-1}, D = diffusion coefficient in $cm^2\ s^{-1}$, C = concentration in mol cm^{-3}, ν = scan rate in V s^{-1}, R = Gas constant in J K^{-1} mol^{-1}, T = temperature in K.

Corresponding to cathodic and anodic peak currents for V_2O_5, D_{Li^+} is found to be $6.987 \times 10^{-9}\ cm^2\ s^{-1}$ and $3.349 \times 10^{-9}\ cm^2\ s^{-1}$, respectively. For MCMB, D_{Li^+} is found to be $3.562 \times 10^{-9}\ cm^2\ s^{-1}$ and $2.974 \times 10^{-9}\ cm^2\ s^{-1}$ for cathode and anodic scan, respectively.

Figure 3.3C shows Galvanostatic charge-discharge profiles for 1st, 2nd, and 3rd cycles for V_2O_5 half–cell at 0.2 C rate between 2.0 V to 4.0 V. The specific discharge/charge capacities of 222/225 mAh g^{-1} were obtained for the first cycle. Three characteristic plateaus were observed in all the cycles during intercalation and deintercalation reactions at around 3.4, 3.1, and 2.2 V, which are associated with the obtained CV redox peaks, as shown in Figure 3.3A. The cycling performance for the half–cell at 0.2 C rate with coulombic efficiency is shown in Fig. 3.3D. After 50 cycles, the specific discharge/charge capacities of 180/183 mAh g^{-1} were observed. The capacity fade over 50 cycles is about 19% with the coulombic efficiency of 98%. MCMB anode provided a very stable capacity of 350 mAh g^{-1} at 0.1 C between 0.01 – 2.0 V (Figure B.3).

Full–cells are the practical batteries used in industrial applications, which comprise of anode and cathode. However, they still present challenges and prospects for future research and developments. Full–cell performance depends on the lithiated cathode, as it is the only source of lithium in the system.[31] However, for cathodes like V_2O_5, which does not have lithium of their own, pre-lithiation is one of the processes used to supplement Li^+ ions to the system.[32] In this report, we pre-lithiated the anode to complete the formation of the SEI layer and then reassembled

it with the cathode (based on capacity balancing). Figure 3.3E illustrates the voltage characteristics of the pre-lithiated MCMB/V_2O_5 full–cell. The polarization and reversibility of the voltage profile during the first discharge were improved to a larger extent compared to the half–cell performance in Fig. 3.3C. Galvanostatic cycling over the 50 cycles at 0.2C between 2.0 V – 4.0 V is very remarkable and very stable, yielding a specific discharge/charge capacity of 185/192 mAh g^{-1}, as shown in Fig. 3.3F. The N/P ratio was 1.03 and on cycling the formation of cathodic impedance interface (CEI) on the surface of cathode consumed Li^+ ions availability for the subsequent cycles.[33] Typically, CEI on V_2O_5 consists of inorganic components viz., LiF, Li_2CO_3, and organic components viz., $ROCO_2Li$, C=O/C–O species. CEI saturates on continuous cycling, however it may dissolve/remove from the surface of cathode due to puckering of V_2O_5 during delithiation.[34] After 50 cycles, the specific discharge/charge capacities of 149/150 mAh g^{-1} were observed. The capacity fade over 50 cycles is again ~19% i.e., ~0.4% per cycle. The coulombic efficiency for each cycle has been >99%, enhanced compared to half–cell performance.

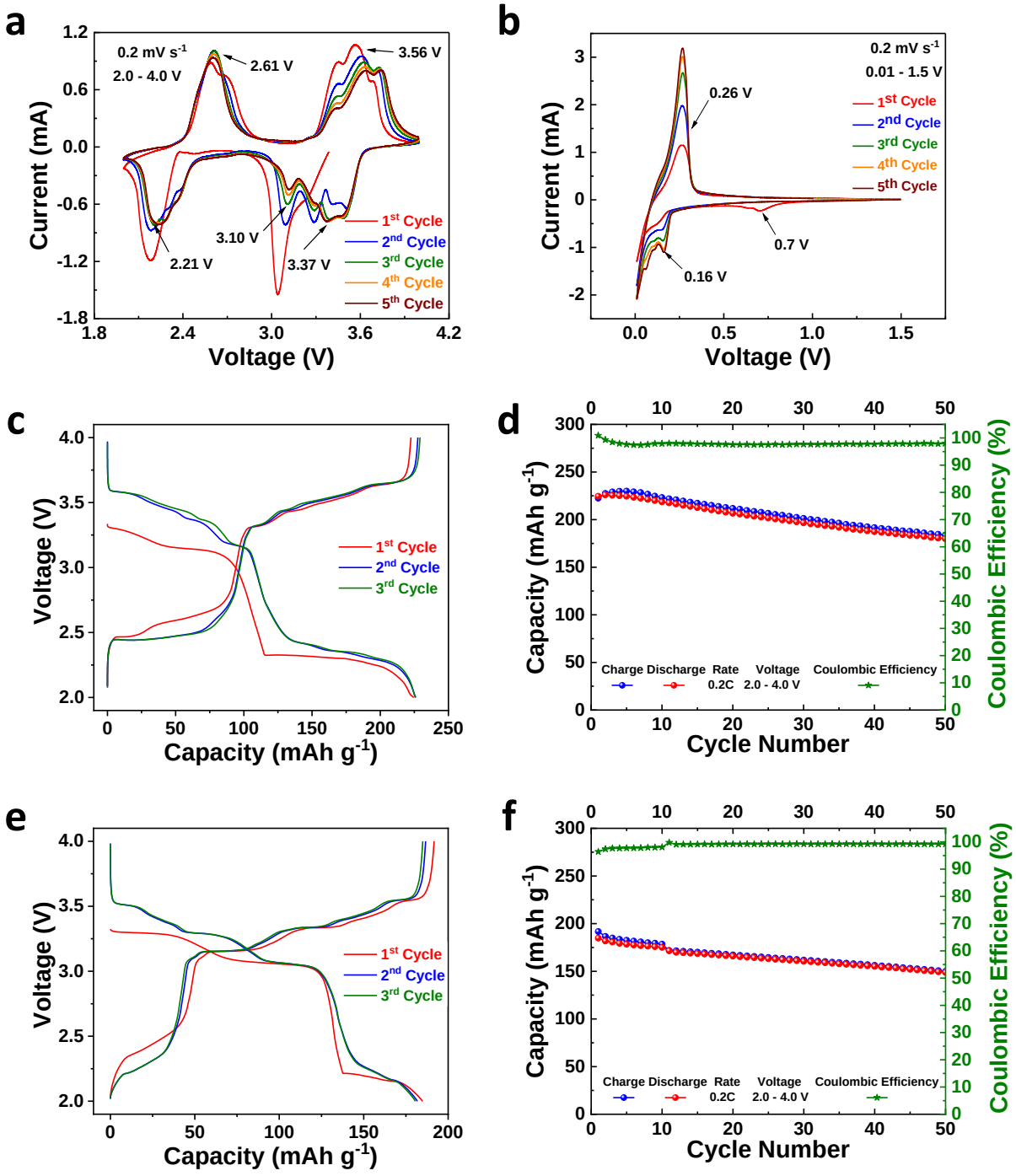

Figure 3.3: Cyclic Voltammetry of A: V_2O_5, B: MCMB at scan rate 0.2 mV s^{-1}; Electrochemical performance of Li/V_2O_5 half–cell: C: voltage profile, D: cycle performance for 50 cycles at 0.2C rate at 0.2 C rate; Electrochemical performance of pre-lithiated MCMB/V_2O_5 full–cell: E: voltage profile, F: cycle performance for 50 cycles at 0.2C rate.

3.4.3 Dual SEI Layers Formation using RLIB

Even after four decades of using full–cell LIBs, they still present challenges and thus, offer varied prospects for further research. The challenge is not just to identify the new materials with high power and energy densities, and their large–scale production but also, how to convert and store the energy required. It is becoming quite evident that these challenges will require innovations in the design and optimization of the materials.[35] Unlike the half–cell, where there are unlimited Li^+ ions from metallic lithium electrode; in the full–cell, limited Li^+ ions are consumed and capacity fades due to undesirable side reactions. Thus, discovering a way to compensate Li^+ ion losses, balance the positive and negative electrodes in full–cell, lithiation of lithium-free cathodes, and capacity fading, which are urgent challenges requiring researchers' attention. Fortunately, these challenges can be answered through the novel design of RLIB.

Figure 3.4 depicts the operation of RLIB in different modes to achieve lithiation of the anode and conventional cycling between cathode and anode. Since V_2O_5 is a lithium-free cathode, it requires Li^+ ions to cycle with MCMB conventionally. These Li^+ ions are provided to it via MCMB, which in turn derives them from the lithium reservoir. When RLIB was operated in Mode–1, the circuit connected the MCMB anode with the Li^+ reservoir. The MCMB was lithiated till 0.01 V at 0.06C rate. During this lithiation process, Li^+ ions react with electrolyte solvents to reduce them and form SEI layer. In this case, MCMB is coated on a Cu mesh current collector. Hence, Li^+ ions can be conducted across the current collector. Since MCMB has two interfaces viz., one facing lithium and the other facing V_2O_5 cathode, the SEI layers are formed on both. The theoretical capacity of MCMB is 372 mAh g^{-1}, however, in Fig. 3.4A, it is observed that the capacity derived is higher than the theoretical limit. Dual SEI layer formation is the primary cause for it.

3.4.4 RLIBs lithium-ion full-cell cycling performance V_2O_5 vs. MCMB

Once the MCMB anode is lithiated through Mode–1, it has a quite sufficient amount of Li^+ ions to cycle with V_2O_5 cathode. Subsequently, RLIB was operated in Mode–2, which connected the circuit between V_2O_5 cathode and the lithiated MCMB anode. Figure 3.4B demonstrates the voltage characteristics of the lithiated MCMB/V_2O_5 in Mode–2. Extraordinary voltage characteristics are displayed for all the cycles as compared with half–cell and full–cell. There is

no polarization in the first cycle discharge step as could be seen in the previous cases. RLIB improvised the inherent characteristics of conventional cycling. Three characteristic plateaus of phase changes in the cathode during lithiation can be clearly seen at 3.4, 3.2, and 2.3 V, and corresponding delithiation plateaus were observed, demonstrating high reversibility of the phase changes in the RLIB system. Galvanostatic cycling over the 50 cycles at 0.2C between 2.0 V – 4.0 V is stellar and remarkably stable, achieving a specific discharge/charge capacity of 251/264 mAh g^{-1}, as shown in Fig. 3.4C. There is some difference in charge and discharge capacities for the initial few cycles, these may arise from the system reconfigurations and stabilizations viz., CEI formation, electrolyte intercalation. In the full-cell studies, lithium-ion free cathode typically stabilizes after few cycles of prelithiation as compared to conventional formation cycles. Following this, the system exhibits high stability and reversibility with coulombic efficiency >99% in subsequent cycles. After 50 cycles, the specific discharge/charge capacities of 189/190 mAh g^{-1} were observed.

3.4.5 Direct–Mode Galvanostatic Cycling Performance

Various strategies have been applied to enhance the electrochemical performance of Li metal batteries to reduce the risk of dendrites short-circuiting the batteries and designing a functional membrane is one of them. Surface alteration of the conventional PP separator with hydroxyl groups, silica-nanoparticles, and polydopamine, etc., have been some of the approaches to suppress dendrite propagation. These approaches on several occasions alter the electrochemical characteristics of the charge-discharge profiles, affect cell performance.

In RLIB, MCMB anode sandwiched between two PP separators does act as a barrier to prevent dendrite propagation. When RLIB is operated in direct mode, the circuit connects the Li reservoir with the V_2O_5 cathode, bypassing the MCMB anode. The presence of Cu mesh current collector allows for the conduction of Li^+ ions through itself and anode material. The presence of conductive anode material provides a regularized path with reduced local current density for Li^+ ions for transportation. Figure 3.4D shows the voltage characteristics of RLIB in the Direct–Mode. The performance is concurrent with that of the half–cell, as essentially it is a half–cell with the sandwich separators. The inherent characteristic plateaus of the V_2O_5 cathode are preserved in the Direct–Mode. The Galvanostatic cycling, shown in 4e, illustrated features viz., capacity, initial system reconfiguration, and fade similar to previous cases. The first cycle and 50^{th} cycle discharge

/charge capacities were high at 262/268 and 201/203 mAh g^{-1}, respectively. The presence of the porous sandwich anode might be advantageous in accommodating volumetric variations during intercalation and deintercalation of Li^+ ions. Also, sandwiched anode facilitates higher electrolyte penetration and facilitates the transport of Li^+ ions.

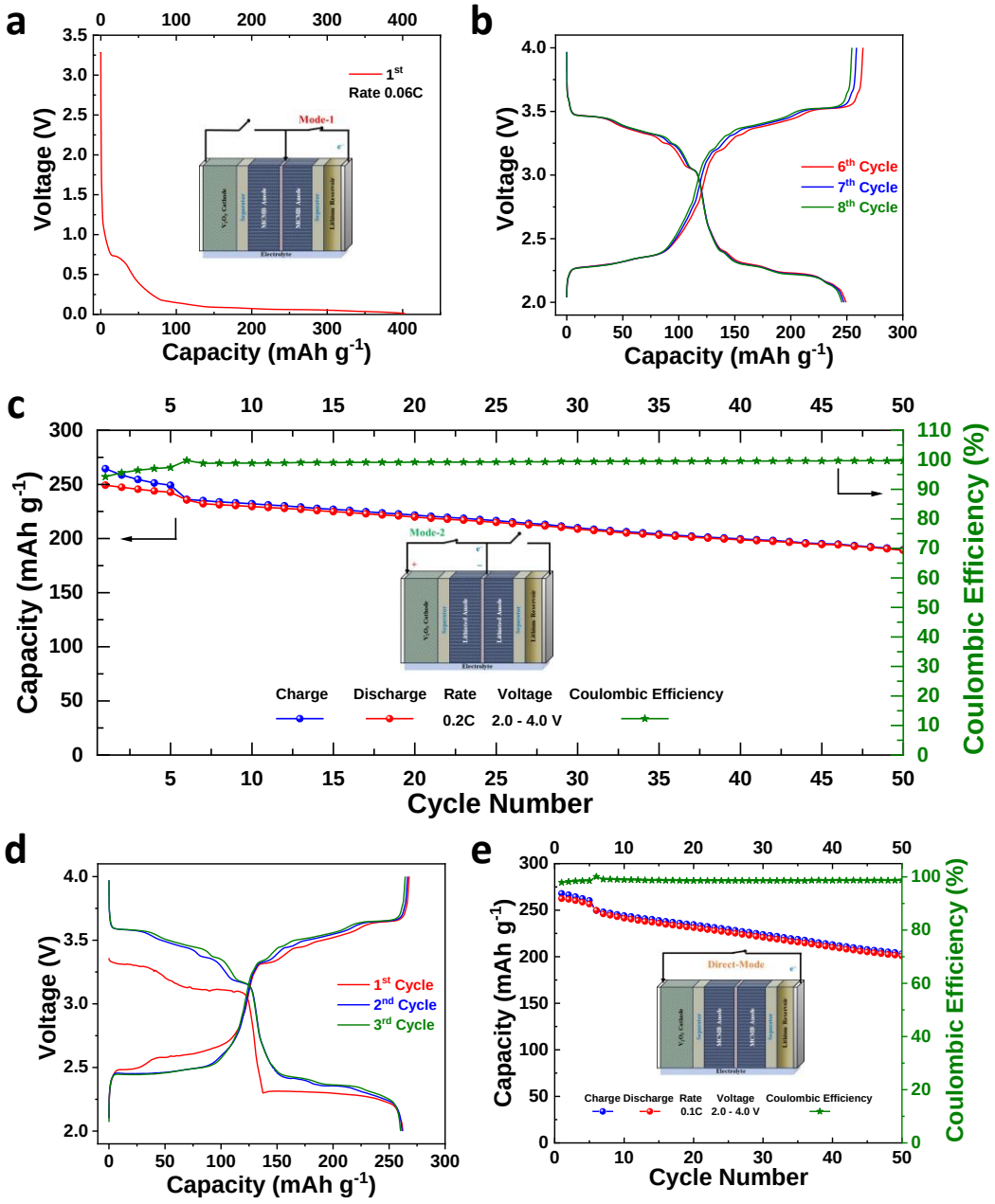

Figure 3.4: Electrochemical Performance of RLIB: A: In situ lithiation of MCMB through Mode–1 (Li/MCMB), B: Voltage characteristics in Mode–2 (MCMB/V_2O_5), C: galvanostatic cycling between lithiated anode and cathode through Mode–2(MCMB//V_2O_5); Direct-Mode (Li//V_2O_5): D: voltage characteristics; and E: galvanostatic cycling between 2.0 V – 4.0 V at 0.2C

Electrochemical impedance spectroscopy (EIS) is a very powerful technique in accurately analyzing, and mechanistically elucidating the electrochemical processes and also, to diagnose batteries viz., state of health, state of charge, internal cell temperature.[36] EIS spectra are majorly influenced by the battery chemistry. Based on the impedance spectra, equivalent circuits can be constructed, which help decipher complex physical and chemical processes inside the cell. It gives important information about the interfacial properties of lithiation and delithiation into cathode and anode materials. The Faradaic impedance can be represented in the form of a circuit of capacitors, resistors, diffusion elements, and calculating these values helps in understanding the experimental results. The EIS spectrum is presented in form of Nyquist-Plot, which has two slightly depressed semicircles in the high-frequency zone and a line in the low-frequency zone. The line is called the Warburg element, which signifies the mass transfer diffusion phenomenon and represents overpotential because of concentration gradients in the electrodes between current collectors and electrolyte. Various factors viz., current, SoC, temperature, and porosity affects these gradients. Warburg impedance, thus, depends on these parameters' fluctuations.

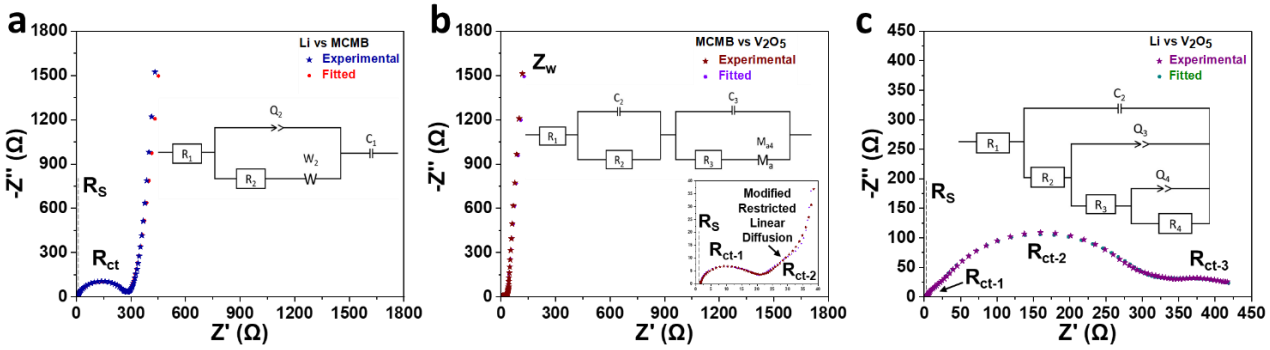

Figure 3.5: Electrochemical impedance spectroscopy of the RLIB in A: Mode–1 (Li/MCMB), B: Mode–2 (MCMB/V_2O_5), and C: Direct–Mode (Li/V_2O_5)

Figure 3.5 and B.4 show the EIS spectra for RLIB in different modes, full–cell, half–cell (represented by dots) along with fitted curve (represented with asterisks). In Mode–1 (Li/MCMB), as shown in Fig. 3.5A, the series resistance (R_S) was 1.9 Ω and charge transfer resistance (R_{ct}) was 70 Ω. At the same time, semi-infinite linear diffusion-limited Warburg impedance can be observed for MCMB at low frequencies with the fitted equivalent circuit. R_s is the impedance the solvated Li^+ ions experience when transporting through the electrolyte and derives from the friction of ions and electrolyte.[37] It is found to be purely Ohmic behavior. The capacitance component is

dominant in the circuit due to the presence of dual SEI layers on the anode, which further impedes the movement of Li^+ ions across the SEI layers. During Mode-2 operation (MCMB/V_2O_5), as shown in Fig. 3.5B the R_S was observed to be 1.4 Ω and charge transfer resistances (R_{ct-1}& R_{ct-2}) across interfaces of both the electrodes were found to be astonishingly low of 20 Ω and 12 Ω. EIS profile demonstrated modified restricted linear diffusion-limited Warburg impedance with the fitted equivalent circuit. These low values are critical for improvement in the electrochemical performance of V_2O_5 and the lower the value implies higher conductivity of the material. Also, since the V_2O_5 is vacant, and facilitates the easy accommodation of Li^+ ions in its host sites.[38] In the Direct-Mode (Li/V_2O_5), shown in Fig. 3.5C, R_S is 4.2 Ω and there are three charge transfer resistances (R_{ct-1}, R_{ct-2} & R_{ct-3}), which ions must overcome when transporting from one end to the another and their values observed were 25, 296, and 94 Ω. EIS profile demonstrated bounded diffusion-limited Warburg impedance with the fitted equivalent circuit. In this mode, the Li^+ ions must pass through dual SEI layers of MCMB anode and CEI layer of V_2O_5 cathode, which makes diffusion of ions, a challenge. Interestingly, all three boundary conditions of Fick's law i.e., semi-infinite, restricted and bounded diffusion conditions are demonstrated in RLIBs. All the parameters of the equivalent circuits are presented in Table B.1. The electrochemical parameters fitted using the software are in excellent agreement with experimental data.

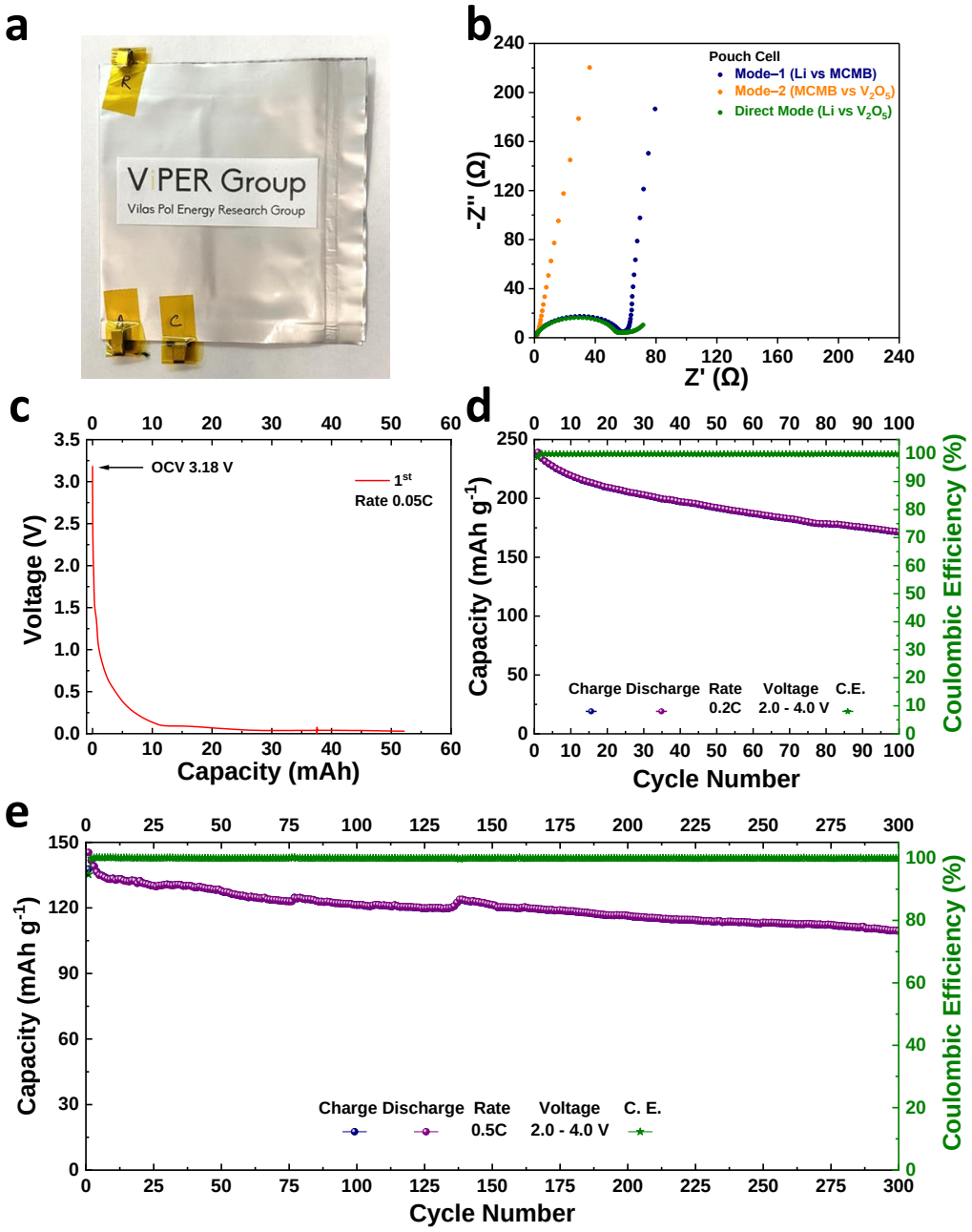

Figure 3.6: A: Pouch cell configuration of RLIB, B: Electrochemical impedance spectroscopy of the RLIB in different modes; Electrochemical Performance of RLIB pouch cell: C: in situ lithiation of MCMB through Mode–1, and Galvanostatic cycling between 2.0 V – 4.0 V through Mode–2 D: at 0.2C, and E: at 0.5C

Pouch cell is the most efficiently packed and common cell format in commercial production that offers high flexibility during construction. Figure 3.6A illustrates the RLIB pouch cell configuration. Figure 3.6B shows EIS for different modes of pouch cell configuration. Values of R_S for Mode–1, Mode–2, and Direct–Mode are 0.28 Ω, 0.49 Ω, and 0.49 Ω, respectively and R_{ct} are 0.5 Ω, 58 Ω, 53 Ω, respectively. The trends observed in the pouch-cells are congruent to CR-2032 configurations. The pouch cell is connected in Mode–1 (Li/MCMB) and discharged from OCV of 3.18 V to achieve 50 mAh capacity of MCMB electrode (shown in Fig. 3.6C). This was done to provide sufficient Li^+ ions to MCMB (~1.25–1.3 N/P). The galvanostatic cycling of the prototype of RLIB on a pouch cell format configuration is shown in Fig. 3.6C&D through Mode–2. The pouch cells were then switched to Mode–2 to achieve cycling at 0.2C (Fig. 3.6C) and 0.5C rates (Fig. 3.6D). Pouch cell performance is better than coin–cells. At 0.2C rate, a high initial capacity of 240 mAh g^{-1} was achieved, and capacity retention is ~75% after 100 cycles. At 0.5C rate, stable cycling was observed over 300 cycles with ~77% capacity retention. At higher C rates, lower capacity is observed, which may arise from poor ionic conductivity of the cathode, higher overpotential, and layered to spinel transitions or other structural modifications during cycling.[39] Interestingly, the specific capacity performance observed over the 300 cycles for V_2O_5 is comparable to that of LFP, LCO, NCM cathodes.

Presently, the target for the EV market is to produce batteries with >500 Wh kg^{-1}, <US$100 $(kWh)^{-1}$ at the pack level. Various options are being tried from changing chemistries to Li metal batteries in solid-state. However, most of the studies have been sharply attentive towards material research or optimizing parameters like electrolyte, porosity, reduce inactive materials, improve N/P ratio, etc.[40] It is very clear that there is a need for out-of-box thinking to tackle this herculean task for this technology to prevail over competing technologies like H_2 storage, fuel cells, supercapacitors, etc. We envision the RLIB technologies for usage in lithium-free cathode systems, conventional LIBs, solid-state batteries, etc. The ideology behind Direct-Mode cycling can be applied to conventional batteries to refuel the Li+ ions, which are lost after forming the SEI layers or capacity fade across multiple anodes from just one reservoir. The advantage from the usage of ultra-thin lithium reservoir can fulfill the target for EV markets, without compromising a lot on energy density and cost of the batteries.

3.5 Conclusions

In summary, the concept of reserve lithium-ion batteries for lithium-free cathode material is proposed with MCMB anode and experimentally validated. We established V_2O_5 cathode performance in various formats of cells viz., half–cell, full–cell, and RLIB. RLIB demonstrated exceptional stable and high specific discharge/charge capacities of 251/264 mAh g^{-1} in contrast to 185/192 mAh g^{-1} for full–cell and 222/225 mAh g^{-1} for half–cell. The improvement of the voltage characteristics in terms of reversibility and stability were seen in RLIB compared to full–cell and half–cell. Further, it was demonstrated the utility of the Direct-Mode cycling in RLIB to facilitate the conduction of Li^+ ions across PP sandwiched MCMB anode. Through the construction of RLIB pouch cell configuration, stable galvanostatic performance was observed over 100 cycles at 0.2C and 300 cycles at 0.5C rates (connected in Mode–2). The mechanistic elucidation of the electrochemical process during different modes of operation for RLIB was provided with the help of EIS. The boundary conditions of Fick's law viz, semi-infinite, restricted, and bounded diffusion conditions are exhibited in RLIBs. RLIB can be used for lithiation of lithium-free cathodes viz., sulfur, vanadium oxides, FeS_2, MnO_2, FeF_3, etc., to compensate SEI layer formation Li^+ ions losses, balance the positive and negative electrodes in full–cell, and refuel Li^+ ions after the capacity fade.

3.6 Acknowledgement

The authors would like to express their gratitude towards Purdue University for supporting the battery work. Authors would like to thank Deep Jokhakar and Vihang Parikh for their support in constructing the RLIB pouch cells.

3.7 References

1. J. Wang, H. Tang, L. Zhang, H. Ren, R. Yu, Q. Jin, J. Qi, D. Mao, M. Yang, Y. Wang, P. Liu, Y. Zhang, Y. Wen, L. Gu, G. Ma, Z. Su, Z. Tang, H. Zhao, and D. Wang, *Nature Energy* **2016**, 1: p. 16050.
2. D. Gohlke and Y. Zhou, T.O.V.T.O. USDOE Office of Energy Efficiency and Renewable Energy (EERE), Editor. **2020**, Argonne National Lab. (ANL), Argonne, IL (United States): United States.

3. L.R. De Jesus, G.A. Horrocks, Y. Liang, A. Parija, C. Jaye, L. Wangoh, J. Wang, D.A. Fischer, L.F. Piper, D. Prendergast, and S. Banerjee, *Nat Commun* **2016**, 7: p. 12022.
4. L. Wang, Z. Wu, J. Zou, P. Gao, X. Niu, H. Li, and L. Chen, *Joule* **2019**, 3(9): p. 2086-2102.
5. M. Palanisamy, M.H. Parekh, and V.G. Pol, *Adv. Funct. Mater.* **2020**.
6. W. Hua, M. Chen, B. Schwarz, M. Knapp, M. Bruns, J. Barthel, X. Yang, F. Sigel, R. Azmi, A. Senyshyn, A. Missiul, L. Simonelli, M. Etter, S. Wang, X. Mu, A. Fiedler, J.R. Binder, X. Guo, S. Chou, B. Zhong, S. Indris, and H. Ehrenberg, *Advanced Energy Materials* **2019**, 9(8).
7. M. Freire, N.V. Kosova, C. Jordy, D. Chateigner, O.I. Lebedev, A. Maignan, and V. Pralong, *Nat Mater* **2016**, 15(2): p. 173-7.
8. X. Yu, Y. Lyu, L. Gu, H. Wu, S.-M. Bak, Y. Zhou, K. Amine, S.N. Ehrlich, H. Li, K.-W. Nam, and X.-Q. Yang, *Advanced Energy Materials* **2014**, 4(5).
9. T. Li, X.-Z. Yuan, L. Zhang, D. Song, K. Shi, and C. Bock, *Electrochemical Energy Reviews* **2019**, 3(1): p. 43-80.
10. A. Pan, H.B. Wu, L. Yu, T. Zhu, and X.W. Lou, *ACS Appl Mater Interfaces* **2012**, 4(8): p. 3874-9.
11. A. Odani, V.G. Pol, S.V. Pol, M. Koltypin, A. Gedanken, and D. Aurbach, *Advanced Materials* **2006**, 18(11): p. 1431-1436.
12. M. Koltypin, V. Pol, A. Gedanken, and D. Aurbach, *Journal of The Electrochemical Society* **2007**, 154(7).
13. A. Manthiram, J.C. Knight, S.-T. Myung, S.-M. Oh, and Y.-K. Sun, *Advanced Energy Materials* **2016**, 6(1).
14. P.K. Nayak, E.M. Erickson, F. Schipper, T.R. Penki, N. Munichandraiah, P. Adelhelm, H. Sclar, F. Amalraj, B. Markovsky, and D. Aurbach, *Advanced Energy Materials* **2018**, 8(8).
15. P. Nakhanivej, S.K. Park, K.H. Shin, S. Yun, and H.S. Park, *Journal of Power Sources* **2019**, 436.
16. Y. Tang, X. Rui, Y. Zhang, T.M. Lim, Z. Dong, H.H. Hng, X. Chen, Q. Yan, and Z. Chen, *J. Mater. Chem. A* **2013**, 1(1): p. 82-88.
17. A.M. Cao, J.S. Hu, H.P. Liang, and L.J. Wan, *Angew Chem Int Ed Engl* **2005**, 44(28): p. 4391-5.
18. S.-B. Son, T.A. Yersak, D.M. Piper, S.C. Kim, C.S. Kang, J.S. Cho, S.-S. Suh, Y.-U. Kim, K.H. Oh, and S.-H. Lee, *Advanced Energy Materials* **2014**, 4(3).

19. F. Badway, F. Cosandey, N. Pereira, and G.G. Amatucci, *Journal of The Electrochemical Society* **2003**, 150(10).
20. A. Varzi, D. Bresser, J. von Zamory, F. Muller, and S. Passerini, *Adv Energy Mater* **2014**, 4(10): p. 1-9.
21. S.B. Chikkannanavar, D.M. Bernardi, and L. Liu, *Journal of Power Sources* **2014**, 248: p. 91-100.
22. D. Linden and T.B. Reddy, *Reserve Batteries*, in *Handbook of Batteries*. **2002**, The McGraw-Hill Companies, Inc.
23. J.D. Lee, *Concise Inorganic Chemistry*. 5th ed. **1999**.
24. J. Yao, Y. Li, R.C. Massé, E. Uchaker, and G. Cao, *Energy Storage Materials* **2018**, 11: p. 205-259.
25. Y.L. Cheah, V. Aravindan, and S. Madhavi, *Journal of The Electrochemical Society* **2013**, 160(8): p. A1016-A1024.
26. J.-N. Zhang, Q. Li, Y. Wang, J. Zheng, X. Yu, and H. Li, *Energy Storage Materials* **2018**, 14: p. 1-7.
27. P.J. Kim and V.G. Pol, *Advanced Energy Materials* **2018**, 8(36): p. 1802665.
28. M.H. Parekh, V.P. Parikh, P.J. Kim, S. Misra, Z. Qi, H. Wang, and V.G. Pol, *Carbon* **2019**, 148: p. 36-43.
29. L. Ji, Z. Lin, M. Alcoutlabi, and X. Zhang, *Energy & Environmental Science* **2011**, 4(8).
30. S. Goriparti, E. Miele, F. De Angelis, E. Di Fabrizio, R. Proietti Zaccaria, and C. Capiglia, *Journal of Power Sources* **2014**, 257: p. 421-443.
31. M.-S. Balogun, W. Qiu, Y. Luo, H. Meng, W. Mai, A. Onasanya, T.K. Olaniyi, and Y. Tong, *Nano Research* **2016**, 9(10): p. 2823-2851.
32. M.L. Divya, S. Natarajan, Y.S. Lee, and V. Aravindan, *Small* **2020**, 16(44): p. e2002624.
33. X. Liu, M. Zarrabeitia, B. Qin, G.A. Elia, and S. Passerini, *ACS Appl Mater Interfaces* **2020**, 12(49): p. 54782-54790.
34. R. Dhiman, *Journal of The Electrochemical Society* **2021**, 168(4).
35. K. Zou, W. Deng, P. Cai, X. Deng, B. Wang, C. Liu, J. Li, H. Hou, G. Zou, and X. Ji, *Advanced Functional Materials* **2020**, 31(5).
36. U. Westerhoff, T. Kroker, K. Kurbach, and M. Kurrat, *Journal of Energy Storage* **2016**, 8: p. 244-256.

37. A. Lasia, *Electrochemical Impedance Spectroscopy and its Applications*, in *Modern Aspects of Electrochemistry*, B.E. Conway, J.O.M. Bockris, and R.E. White, Editors. **2002**. p. 143-248.
38. C.-j. Cui, G.-m. Wu, J. Shen, B. Zhou, Z.-h. Zhang, H.-y. Yang, and S.-f. She, *Electrochimica Acta* **2010**, 55(7): p. 2536-2541.
39. A. Manthiram, *Nat Commun* **2020**, 11(1): p. 1550.
40. J. Liu, Z. Bao, Y. Cui, E.J. Dufek, J.B. Goodenough, P. Khalifah, Q. Li, B.Y. Liaw, P. Liu, A. Manthiram, Y.S. Meng, V.R. Subramanian, M.F. Toney, V.V. Viswanathan, M.S. Whittingham, J. Xiao, W. Xu, J. Yang, X.-Q. Yang, and J.-G. Zhang, *Nature Energy* **2019**, 4(3): p. 180-186.

4. SEPARATORS: ARAMID NANOFIBERS FOR HIGH-TEMPERATURE LITHIUM-ION BATTERIES

Mihit H. Parekh,[1] Suyash Oka,[2] Jodie Lutkenhaus,[2] Vilas G Pol[1]

[1]Davidson School of Chemical Engineering, Purdue University, West Lafayette, IN, USA 47907
[2]Artie McFerrin Department of Chemical Engineering, Texas A&M University, College Station, TX, USA 77843

This project was performed in collaboration with Suyash Oka and Dr. Jodie Lutkenhaus from Texas A&M University, where they developed the CPD-ANF separator and conducted mechanical characterization compared to Celgard® PP separator at varied temperatures. The electrochemical performance, thermal safety testing, characterization, and analysis were done by Mihit H. Parekh. The manuscript preparation was done by Mihit H. Parekh and Suyash Oka.

4.1 Overview

Ionically conducting, porous separator membranes with submicrometer size pores play an important role in governing the outcome of lithium-ion batteries (LIBs) in terms of life, safety, and effective transport of ions. Though the polyolefin membranes have dominated the commercial segment for the past few decades, to develop next-generation batteries with high-energy density, high capacity, and enhanced safety, there is a need to develop advanced separators with superior -thermal stability, -electrolyte interfacial capabilities, -high melting temperature and -mechanical stability at elevated temperatures. We prepared aramid nanofibers (ANF) with enhanced mechanical and thermal stability dried at the critical point (CPD) (32 ℃) and tested - for mechanical strength, wettability, electrochemical performance, and thermal safety aspects in LIBs. It outperforms Celgard® polypropylene separator in all aspects, delivered a high Young's modulus of 6.9 ± 1.1 GPa and ultimate tensile strength of 170±25 MPa. At 25 ℃ and 40 ℃, stable 300 and 200 cycles with 11% and 10% capacity fade were obtained at 1C rate, respectively. From the multimode calorimetry specially designed to study thermal safety aspects of LIBs coin cells, the thermal signature obtained before the rupturing of the cell demonstrates low exothermicity for CPD-ANF and post-diagnosis illustrates preservation of structural integrity after 300 ℃ depicting possibilities of developing advanced safer, high-performance LIBs.

4.2 Introduction

The functions of porous separator membranes or 'separators' inside the lithium-ion batteries (LIBs) are multiple viz., facilitate the transport of Li^+ ions, act as a physical barrier between electrodes from each other and serve as electrolyte reservoir.[1] Even though not the active component of batteries, they play a crucial role in determining cell performance, cost, safety, energy density, and cycle life. An ideal battery separator would possess high porosity, selective permeability to Li^+ ions, possess thermal, chemical, electrochemical stabilities, as well as maintains mechanical integrity, and being economical, simultaneously.[2, 3] However, practical separators that succeed in a few of these characteristics often falter in others. The transference number and ionic conductivity of the Li^+ ions are hampered by the internal structure of the separator, (5–20% reduction in conductivity). The cost contribution of separator exceeds 20% in high power cells and the target set by USABC being ≤ \$1 m^{-2}.[4] If the separator melts, undergoes mechanical deformation, or ruptures due to piercing of Li dendrites, it can lead to catastrophic failure of the battery due to short-circuiting and thermal runaway. Inhomogeneous transport of Li^+ across the separator can lead to incomplete (de)intercalation reactions and decreases life cycles of LIBs. Hence, it becomes crucial to balance the different properties of separators to develop high-performance batteries.

At present, polyolefin separator membranes such as polypropylene (PP), polyethylene (PE), and polyethylene terephthalate (PET) dominate the LIBs market due to their adequate porosity and scalable manufacturing.[5-7] Out of these, Celgard® PP is the one used most widely. LIBs are operational at a wide range of temperatures, and their performance varies as a function of temperature.[8-10] At high temperatures, the polymeric chains in the separator membrane show an increased movement that leads to a decrease in Young's modulus and hampers the mechanical integrity of the cell.[11-13] Commercial polyolefins are known to shrink and melt at high temperatures >140°C, disclosing low thermal stability and huge safety risk for LIBs. Conventional separators have poor electrolyte uptake and wettability, which reduces production efficiencies. During cycling, active material, solid electrolyte interface (SEI), Li metal debris, etc. may block the pores of the separator and apply stress on it, causing non-homogeneous pathways for Li^+ ions to shuttle across. Therefore, there is a need to develop or improve separator design with desired comprehensive characteristics.

Aramid nanofibers (ANFs), a derivative of Kevlar fibers, or poly-p-phenylene terephthalamide (PPTA) polymer, possess a high tensile modulus (~ 129 GPa), high tensile strength (~ 4 GPa), and good thermal stability till about 450-500℃.[14, 15] They have been investigated in a variety of applications due to their excellent reinforcement abilities.[14-18] Their applicability includes, but is not limited to reinforced composites, thin-film membranes, heat resistant coatings, etc. ANFs are a potential candidate for making LIB and lithium-sulfur battery (LSB) separators. [14-22] Xu et al. have reported a highly compressible and thermally insulating aerogel using ANF and polyimide (PI) blend.[23] Liu et al. have reported a composite LSB separator made of metal-organic frameworks (MOFs) and ANFs that showed a capacity of 961 mAh g^{-1} after 350 cycles at 0.2 C.[17] Li et al. fabricated an m-PEG-modified ANF membrane separator for LIB that showed a tensile strength of 55 MPa and a discharge capacity of 100 mAh g^{-1} in a cell containing lithium cobalt oxide (LCO) cathode and a graphite anode.[16]

In our previous report, we fabricated flame-resistant free-standing ANF membrane separators using vacuum-assisted filtration.[24] They exhibited excellent mechanical characteristics including Young's modulus of 8.8 ± 1.1 GPa and ultimate tensile strength (UTS) of 253 ± 18 MPa.[24] When these separators were used in lithium metal batteries consisting of $LiNi_{0.33}Mn_{0.33}Co_{0.33}O_2$ cathode and metallic Li anode, a maximum capacity of 123.4 mAh g^{-1} was achieved.[24] However, these could not outperform the commercial Celgard® PP membranes, which showed a maximum capacity of 150 mAh g^{-1} in the same cell configuration.[24] We hypothesized the reason for this poor electrochemical performance of ANF separator cells to be Li^+ ion diffusion limitations due to less porosity, poor ionic conductivity, and higher thickness of the ANF separator. These previous separators were dried using a vacuum drying process wherein the arising capillary forces increase the surface tension of films and collapse the pores in the membrane. The pore collapse reduces the porosity of membranes, and this has a detrimental effect on the Li^+ ion transport through the membrane.[25] Also, the poor ionic conductivity of the membrane is proportional to the thickness of the separator because increasing thickness has been shown to increase the charge transfer resistance of separators.[2]

We hypothesize that this problem of low porosities can be tackled by using a different drying method, such as critical point drying (CPD) (also called supercritical drying). CPD is a promising and suitable method for fabricating porous membranes because it helps in retaining the porosity during drying compared to the conventional vacuum oven and freeze-drying processes.[26-

[32] The process begins with inundating the separators with a carrier solvent, typically, ethanol for 3 days. The chamber in the critical point drying machine is filled with this carrier solvent and separators are immersed in it. Later the ethanol is replaced by liquid CO_2, the drying media, at sub-critical conditions. The chamber is then subjected to supercritical conditions with respect to the drying media (liquid CO_2, T > 32°C, P>1400 psig). At the critical point, the liquid CO_2 is converted to gaseous CO_2 in the absence of surface tension and capillary stresses. Thus during CPD, the pores and pore structure do not collapse, and high porosities are obtained.[33, 34] Ionic conductivity also increases by increasing the porosity since there are additional ionic pathways as well as a decrease in tortuosity.[29] There have been a few reports where researchers have obtained higher porosities using the CPD technique.[29, 31-33] However, the use of the CPD to retain higher porosity of battery membrane separators have not been investigated so far.

In this work, retention of the porosity and pore structure of aramid nanofiber (ANF) separators using critical point drying (CPD) and reduced their thickness to facilitate Li^+ ion transport through the channels when harnessed in a typical LIB is developed. The electrolyte wettability and uptake, porosity, and thermal behavior of the separators were characterized. Next, the mechanical performance of these critical point dried aramid nanofiber (CPD-ANF) separators was evaluated using tensile testing at different temperatures. The electrochemical performance of cells equipped with CPD-ANF separators performed in both configurations, LFP half-cell (Lithium metal anode) and LFP full cell (mesocarbon microbeads (MCMB) anode). We also assessed this electrochemical performance at different temperatures to understand the applicability of these separators in a variety of environments. The performance of CPD-ANF separators was compared with commercial Celgard® PP. Over here, mechanistic elucidation of the aramid nanofiber separators for LIBs was performed in an array of conditions that exhibited improvement in the safety aspects.

4.3 Materials and Methods

4.3.1 Materials

Tex 60 Kevlar threads were acquired from Thread Exchange and were cut into approximately 1 cm lengths and their diameter was ~0.25 mm. Dimethyl sulfoxide (DMSO) and 1 M $LiPF_6$ in 1:1 EC/DEC with 5 wt.% FEC were procured through Sigma-Aldrich. Caustic

potassium hydroxide (KOH) was purchased from Amresco. Ethyl alcohol (C_2H_5OH), n-butanol (C_4H_9OH), and pre-cast Nylon filter membranes with an average pore size of 0.2 μm, and Kimwipes were obtained from VWR. Deionized (DI) water was provided through a Milli-Q system. Commercial Celgard® 2500 PP separator was obtained from Celgard®. Liquid CO_2 was obtained from Airgas. The active materials used for the construction of CR-2032 coin-cells viz., lithium iron phosphate (LFP), and mesocarbon microbeads (MCMB) were procured from MSE Supplies LLC. The 1M $LiPF_6$ in 1:1 v/v EC: DEC electrolyte (Sigma Aldrich) had a blend of 5% v/v FEC (Sigma Aldrich) additive for stable performance. C65, conductive carbon was sourced from TIMCAL. PVdF Binder HSV-900 (Arkema) was used in electrode preparation.

4.3.2 Preparation of CPD-ANF Separators

Firstly, aramid nanofiber dispersions were prepared as per our previous report.[24] Briefly, 1 g of Kevlar fibers were mixed in 500 mL of DMSO and 1.5 g of KOH, and the mixture was stirred for 1 week until it turned viscous and dark red. This 2 mg ml^{-1} dispersion was then diluted to 0.2 mg mL^{-1} by adding DMSO. Then 1 ml of DI water was added per mg of ANFs under stirring and the dispersion was then heated to 80 ℃ for 2 h. After allowing it to cool to 45-50 ℃, the dispersion was then vacuum filtered for 3 days using a Nylon membrane. The ANF separator, while being suspended on the membrane, was washed twice in DI water, and then meticulously peeled off the nylon membrane while being submerged in DI water. The films were kept submerged in water for 24 hours followed by ethanol for 3 days. After soaking in ethanol for 3 days, the separators were cut into 1-inch × 1-inch squares before the CPD. The ethanol submersion was proceeded by critical point drying of separators.

4.3.3 Critical Point Drying (CPD) of Aramid Nanofiber Separators

The CPD machine's sample holding chamber was cleaned and wiped with ethanol and Kimwipes before usage. The chamber was filled with ethanol up to 80% of its total volume, the square aramid separators were transferred in, and the chamber was sealed with hand-tightened screws. Next, the chamber was inundated with liquid CO_2 to occupy the entire pore volume of the separators and replace ethanol from the pores. The system was allowed to equilibrate for 4 hours and then it was subjected to CO_2's supercritical conditions (pressure > 1400 psig & temperature >

32 ℃) for 30 mins. Thus, the critical point dried separators were obtained with thicknesses between 5.5 – 6.5 μm.

4.3.4 Physical Characterization

The microscopy images were acquired using scanning electron microscopy, Nova Nano SEM 200. Samples were sputter-coated with a thin layer of platinum using a Sputter Coater 208 HR before the SEM. Raman spectroscopy was performed using a Horiba Jobin Yvon Lab Ram HR microscope with 633 nm excitation. BET N_2 gas physisorption (Quantachrome Instruments, equipped with mesopore analysis) was carried out to obtain pore size distribution, pore volumes, and surface area. The porosity of separators by measured by immersing the samples in 10 ml n-butanol for 2 hours and measuring their masses before and after immersion. The thickness of separators was measured using a height gauge (Tesa μ-Hite) and verified using cross-sectional SEM. Contact angle trials were carried out with a 10 μL drop of 1 M $LiPF_6$ in 1:1 EC/DEC electrolyte and the photographs were taken using a digital camera. The images were analyzed using ImageJ software. Electrolyte uptake tests were conducted by measuring the mass change in separator samples after soaking in 1 M $LiPF_6$ in 1:1 EC/DEC for 24 hours. For dimensional analysis, sample pictures were taken by a mobile phone camera, and the area was measured using Image J software.

4.3.5 Thermal Characterization

The thermal degradation of separators was studied using Thermogravimetric Analyser (TGA, i1000 Instrument Specialist Inc.). The samples were heated in presence of argon from 25 ℃ to 1000 ℃, with a ramp rate of 10 ℃ min^{-1}. Differential scanning calorimetry (DSC, TA Instruments Q200 Analyzer) was performed to investigate the thermal behavior of separators. Samples were heated at 120℃ at ambient pressure for 2 h before carrying out the DSC. Separators were heated from 40 ℃ to 400 ℃ using a heating rate of 10 ℃ min^{-1}. Calorimetry experiments on coin-cells were performed using Multiple Module Calorimetry (MMC 274 Nexus, Netzsch Gerätebau GmbH, Germany), where cells were heated from 30 ℃ to 300 ℃ at a ramp rate of 0.2 ℃ min^{-1}.

4.3.6 Mechanical Characterization

Tensile testing was conducted using a TA Instruments Q800 Dynamic Mechanical Analyzer (DMA) equipped with thin-film clamps. Separators were cut into rectangular strips 15 – 20 mm in length and 2 – 4 mm in width to perform the tests. During tensile testing, the samples were strained at a rate of 1% min^{-1}. For the puncture video, the separator was held firmly with tweezers and a 1 mm-diameter stick was used to puncture the film at the centre.

4.3.7 Electrode and Cell Fabrication

Active material, binder, and C65 carbon were blended in the ratio 8:1:1 and were wet-mixed using adequate N-Methylpyrrolidone (NMP) solvent till desired viscosity was achieved. The slurry is mixed in the high-speed AR-100 Thinky mixer for 40 minutes. The homogeneously stirred slurry was cast on an appropriate current collector through the doctor-blade technique. The obtained laminate was vacuum oven-dried at 80 ℃ for ≥12h. The dried laminate was calendered through rollers to achieve porosity of 35–40%. The calendering was performed based on the porosity calculations i.e.

$$\text{Porosity } (\varepsilon) = 1 - \frac{\text{Bulk Density}}{\text{Particle Density}(\rho)} \tag{4.1}$$

where,

$$\text{Bulk density} = \frac{\text{Mass of electrode}}{\text{Area of electrode} \times \text{Thickness of laminate}} \tag{4.2}$$

$$\text{Particle density} = \frac{\text{Mass of all the components}}{\sum_{i=1}^{n} \rho_i \times \text{mass of component}_i} \tag{4.3}$$

The dried laminate was punched into round discs of ~15mm Φ. The coin cells of CR-2032 were assembled in a glovebox with an inert environment (99.998% Ar) with O_2 and H_2O concentration ≤0.5 ppm each. The anode, separator, cathode, and electrolyte were stacked in CR-2032 and crimped at 1000 psi.

4.3.8 Electrochemical Characterization

Galvanostatic cycling of the crimped cells was conducted using an Arbin cycler in the range of 2.5–4.0V for LFP half–cells, and 2.5–3.8V for LFP-MCMB full cells. Rate performance was

conducted at 0.1, 0.2, 0.5, 1C, 2C, and 5C. Long-term cycle tests were conducted at 1C. ESPEC BTZ 133 temperature controller with Arbin cycler was utilized to perform cycling tests at 40 ℃. Specific capacity was calculated on the basis of the active material of the electrode. EIS and CV were performed on Gamry–600 Reference system. For CV, a scan rate of 0.2 mV $s^{-1}$was used from 2.5–4.0V. For EIS, measurements were collected over the frequency range of 1Mhz to 10 mHz. All the potentials mentioned in the manuscript are versus Li^+/Li.

4.4 Results & Discussion

4.4.1 Fabrication of Critical Point Dried (CPD) ANF Separators

The process development of CPD-ANF is depicted in Fig. 4.1, which results in the formation of 10–15 µm thick ANF separators. The SEM image of Celgard® PP is shown in Fig. 4.2A. Dark, orange colored viscous ANF dispersions were obtained similar to our previous report.[24] The KOH deprotonates the Kevlar threads and facilitates the dispersion process in DMSO. Subsequent dilution, heating, and vacuum-assisted filtration led to free-standing ANF thin films suspended in DI water. Critical point drying using liquid CO_2 leads to porous ANF separators (denoted as CPD-ANF) as can be seen from the SEM imaging in Fig. 4.2B. The thickness of CPD-ANF separators ranged from 10-15 µm, while that of Celgard® PP ranged from 20-25 µm.

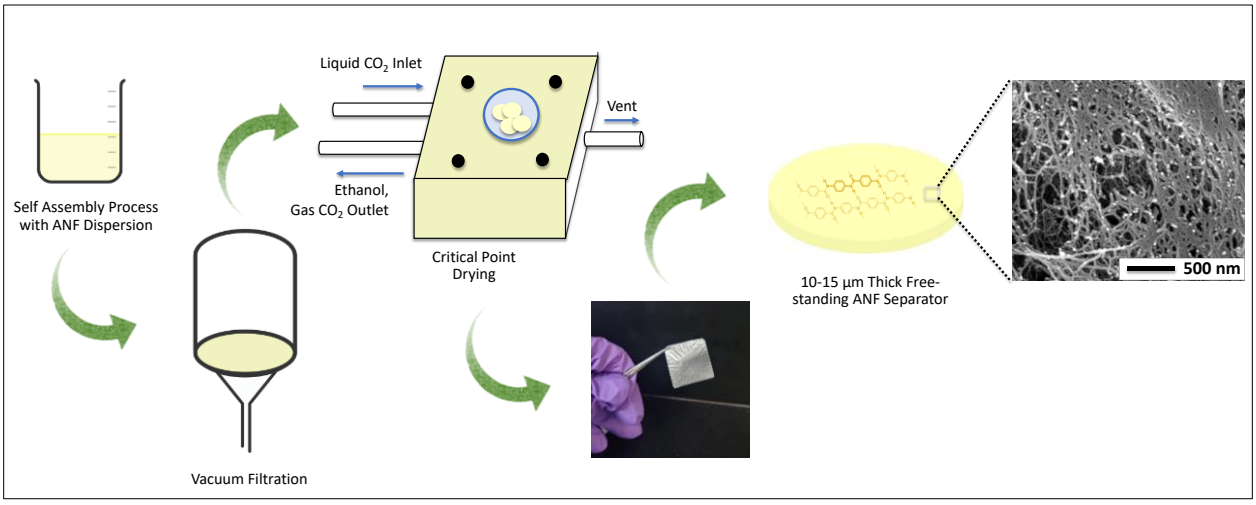

Figure 4.1: Schematic illustrating the process development of critical-point dried ANF separator.

4.4.2 Physical Characterization

BET N_2 physisorption data showed an average pore size of 3.7 nm, a pore volume of 0.31 cm^3/g, and a surface area of 57.47 m^2/g for CPD-ANF separators, as shown in Fig. 4.2C-D. The significantly higher pore volumes and surface areas in CPD-ANF separators are a result of the critical point drying process that prevents any capillary stresses from arising and hence retains the pore structure in the separator. The porosimetry data for CPD-ANF separators along with Celgard® PP and oven-dried ANF separators from our previous report[24] is presented in Table 4.1.

Table 4.1: Comparison data between CPD-ANF, Oven-dried ANF, and Celgard® PP

Properties	**Celgard® PP**	**Oven-dried ANF**	**CPD -ANF**
Avg. pore size (nm)	6.5	0.9	3.7
Pore volume ($cm^3\ g^{-1}$)	0.05	0.0071	0.31
Surface area ($m^2\ g^{-1}$)	11	1.9	57.47

The porosity of the separators was calculated by the n-butanol absorption method and was determined to be 85% of the CPD-ANF separators as compared to just 35% for the Celgard PP. Higher porosity can be attributed to the critical point drying of samples.

Raman spectroscopy confirmed the presence of ANF in the separator with characteristic C=C stretching (1183cm^{-1}, 1279cm^{-1}, 1331cm^{-1}), amide I (1569cm^{-1}), and amide II radial vibrational mode (1647cm^{-1}) peaks (shown in Fig. 4.2G). The thermal degradation behavior of CPD-ANF separator was studied using thermogravimetric analyses (TGA) (shown in Fig. 4.2H). A 5 wt% degradation temperature ($T_{5\%}$) of 428 ℃, onset temperature for degradation (T_{onset}) of 520 ℃, and peak temperature for degradation (T_{peak}) of 565 ℃ were observed for ANF separator. Meanwhile, Celgard® PP showed a $T_{5\%}$ value around 380 ℃. The T_{onset} and T_{peak} were about 398 ℃ and 465 ℃. In comparison to Celgard® PP, the CPD-ANF separator revealed substantially enhanced thermal stability and higher thermal decomposition temperatures. This is attributed to the heat-resistant properties of the polyphenyl-terephthalamide (PPTA) backbone.[35]

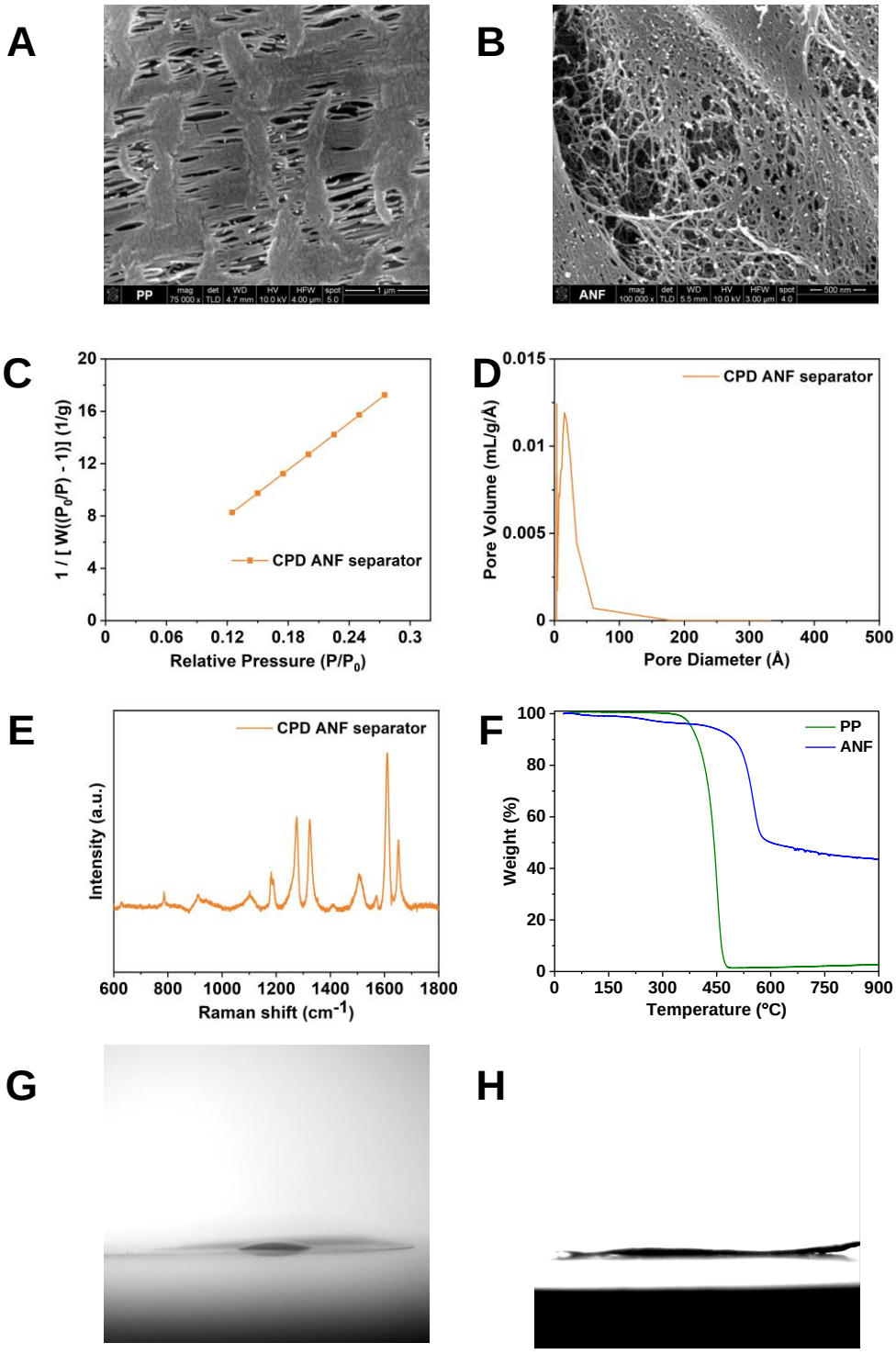

Figure 4.2: Scanning electron microscopy images of A: Celgard® PP separator, and B: CPD-ANF separator; C: BET N_2 physisorption isotherm; D: pore size distribution; E: Raman spectrum for CPD-ANF separator; F: TGA of separators, contact angle measurement of 1M $LiPF_6$ in (1:1 v/v) EC: DEC electrolyte with G: Celgard® PP separator, and H: CPD-ANF separator.

To understand the wetting properties of the separators, the samples were subject to contact angle and electrolyte uptake tests with 1 M $LiPF_6$ in 1:1 EC: DEC (v/v) with 5 wt.% FEC additives. CPD-ANF separator exhibited a contact angle of 0° as compared to 24° by Celgard® PP, thus showing an excellent wetting property of CPD-ANF separator by the electrolyte compared to Celgard® PP. Next, the CPD-ANF separators showed an electrolyte uptake of 130%, which was much higher than 71% by Celgard® PP. This could be due to higher porosity, pore volumes, and excellent wettability of the CPD-ANF separators.

4.4.3 Mechanical Characterization

It is critical to evaluate the mechanical properties of the membranes for LIBs since batteries are frequently exposed to situations wherein their mechanical integrity may be compromised.[36] Tensile tests of CPD-ANF and Celgard® PP separators were conducted at a 1% min^{-1} strain rate. Celgard® PP separator aligned in the stretch direction during manufacturing, and hence mechanical tests were performed with the stretch direction parallel to the tensile force (longitudinal direction). The stress−strain plots and data assessed at room temperature (RT) and 40℃ are presented in Fig. 4.3A-D. Box plots comparing the ultimate tensile strengths (UTS) and Young's moduli of separators at different temperatures are presented in Fig. 4.3E-F. At 25 ℃, CPD-ANF separators exhibited Young's modulus: 6.9 ± 1.1 GPa and UTS: 170 ± 25 MPa. Celgard® PP's performance was poor, showing Young's modulus of just 0.5 ± 0.05 GPa and a UTS of 84 ± 8 MPa.

It was important to assess the performance of separators at different battery operating temperatures such as 40 ℃ to understand the wide temperature applicability of CPD-ANF separators.[13] At 40℃, both separators showed greater flexibility due to the increased movement of polymer chains. CPD-ANF's Young's modulus was about 5.9 ± 0.4 GPa strength and UTS was about 173 ± 20 MPa. Celgard® PP continued to show low Young's modulus of 0.4 ± 0.05 GPa and could retain a UTS of 73 ± 5 MPa. CPD-ANF separators showed excellent Young's modulus and strength indicating that the separator can endure much higher loads without failing and deforming. It was able to outperform Celgard® PP at high temperature indicating its superior capability in mitigating mechanical failure in LIBs.

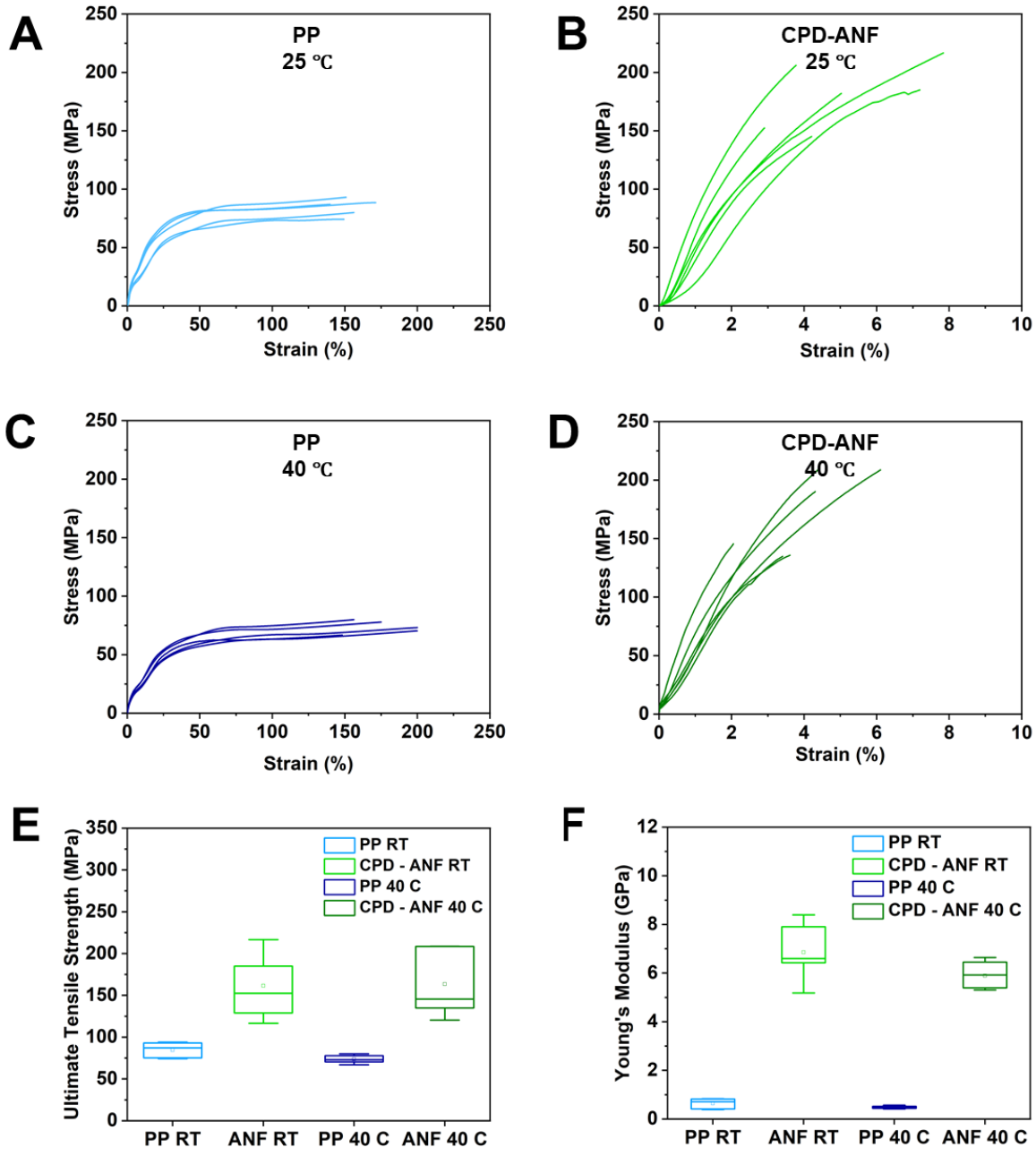

Figure 4.3: Tensile stress−strain curves for A: Celgard® PP, B: CPD-ANF at 25 ℃; C: Celgard® PP, D: CPD-ANF at 40 ℃; Box-plots for E: Ultimate tensile strength, and F: Young's Moduli at different temperatures.

4.4.4 Electrochemical Characterization.

Figure 4.4 shows the electrochemical performance of CPD-ANF separators in comparison to the PP separators. For the cathode, lithium iron phosphate was utilized, owing to its better cycle stability, cycle life, thermal stability, economical compared to the NMC, or LCO cathodes.[37] For the anode, MCMB was used, which is the conventional anode for LIBs. Cyclic voltammetry helps deconvolute the reduction and oxidation reactions that occur during the cycling of batteries. It also helps segregate Faradaic reactions from non-Faradaic ones that may be occurring in the system. Figure 4.4A-B shows CV plots for the PP separator and CPD-ANF separators, respectively. The redox peaks for LFP half–cell with polypropylene separator appeared at 3.18/3.65 V, which is analogous to that observed for CPD-ANF, where the peaks appeared at 3.25/3.65 V. The reversibility of the curves in the subsequent cycles demonstrates the reproducibility of the Faradaic reactions in the cells. The peak currents are more defined and sharper for CPD-ANF separator cell compared to PP cell. Also, CPD-ANF demonstrates less polarization than PP separator cell possibly from lower interfacial interactions.

To understand the kinetic characteristics of de-(intercalation), electrochemical impedance spectroscopy was conducted for half–cells. As shown in Fig. 4.4C-D, Nyquist plots were obtained of Li vs. LFP that showed semi-circle in the high-frequency region and Warburg element in the low-frequency region. The ohmic resistance (R_S) obtained was 1.87 Ω for cell with PP separator compared to 4.4 Ω for CPD-ANF separator cell. The charge transfer resistance (R_{CT}) for PP compared to CPD-ANF was about 212 Ω compared to 104 Ω. The interfacial compatibility between cathode-separator and lithium-metal-separator plays a critical role in practical application. The reduction in the R_{CT} implies better interfacial compatibility between the interfaces.[25] Also, lower electrolyte retention leads to high resistance in the system indicating that CPD-ANF has higher electrolyte retention capabilities than PP separator. Thus, enhanced electrolyte uptake and wetting, and conductivity lead to lower impedance in the CPD-ANF system.

To determine the performance of the half–cells, the cells were galvanostatic cycled between 2.5 – 4.0 V at different C-rates. Initially, the cells were cycled at 0.1C to determine the maximum practical capacity that could be realized. The performance of both the separators was similar, though the first cycle for the PP separator had more polarization compared to the CPD-ANF separator-contained cell (as shown in Fig. 4.4E-F). The CPD-ANF separator cells maintained similar polarization through the subsequent cycles. The first cycle coulombic efficiency for both

the system was ~95-96%. This small loss comprises the formation of cathodic electrolyte interphase (CEI) on the surface of the cathode material. The performance delivered by both the systems looks identical until zoomed in to observe that the specific capacity delivered by CPD-ANF cell was 163/162 mAh g^{-1} compared to 161/160 mAh g^{-1} PP cell, as shown in Fig. 4.4G. Over the next few cycles, the performance of CPD-ANF remained marginally higher than the PP separator. This difference may result from a variety of factors viz., homogenous transport of Li+ ions, better wetting capabilities, and electrolyte-filled pore network, higher permeability, and weaker electrolyte-separator interactions.[38]

Figure 4.4H demonstrates the comparison between the rate capabilities of the two separators. Multi-rate cycling for the two systems was conducted from 0.1C to 5C, following which the systems were cycled again at 0.1C to check for capacity retention. From the rate study, it appeared that CPD-ANF performance exceeded that of Celgard® PP, especially as the rate increased, possibly because of the thinner CPD-ANF separator. At 1C, 2C, and 5C, CPD-ANF comprised cell delivered high charge capacity of 127 mAh g^{-1}, 112 mAh g^{-1}, and 87 mAh g^{-1}. The capacity retention for CPD-ANF was 97.1% compared to 96.2% for PP. Typically, the separator structure affects the conductivity, diffusion coefficients, and transference number of Li^+ ions. At low C-rates, the salt concentration gradient is not substantial across the separator. However, with an increase in the rate, large gradients and overpotentials may develop across the separator, if the structure is unfavorable for transport, affecting the performance especially the transference number of Li^+ ions. The solvation structure across the Li^+ ions interacts with the separator surface affecting the transport phenomenon of ions through the separators. CPD-ANF with its enhanced wetting capabilities, reduced thickness, higher electrolyte uptake, uniform porosity explains better performance characteristics at different C-rates.[39]

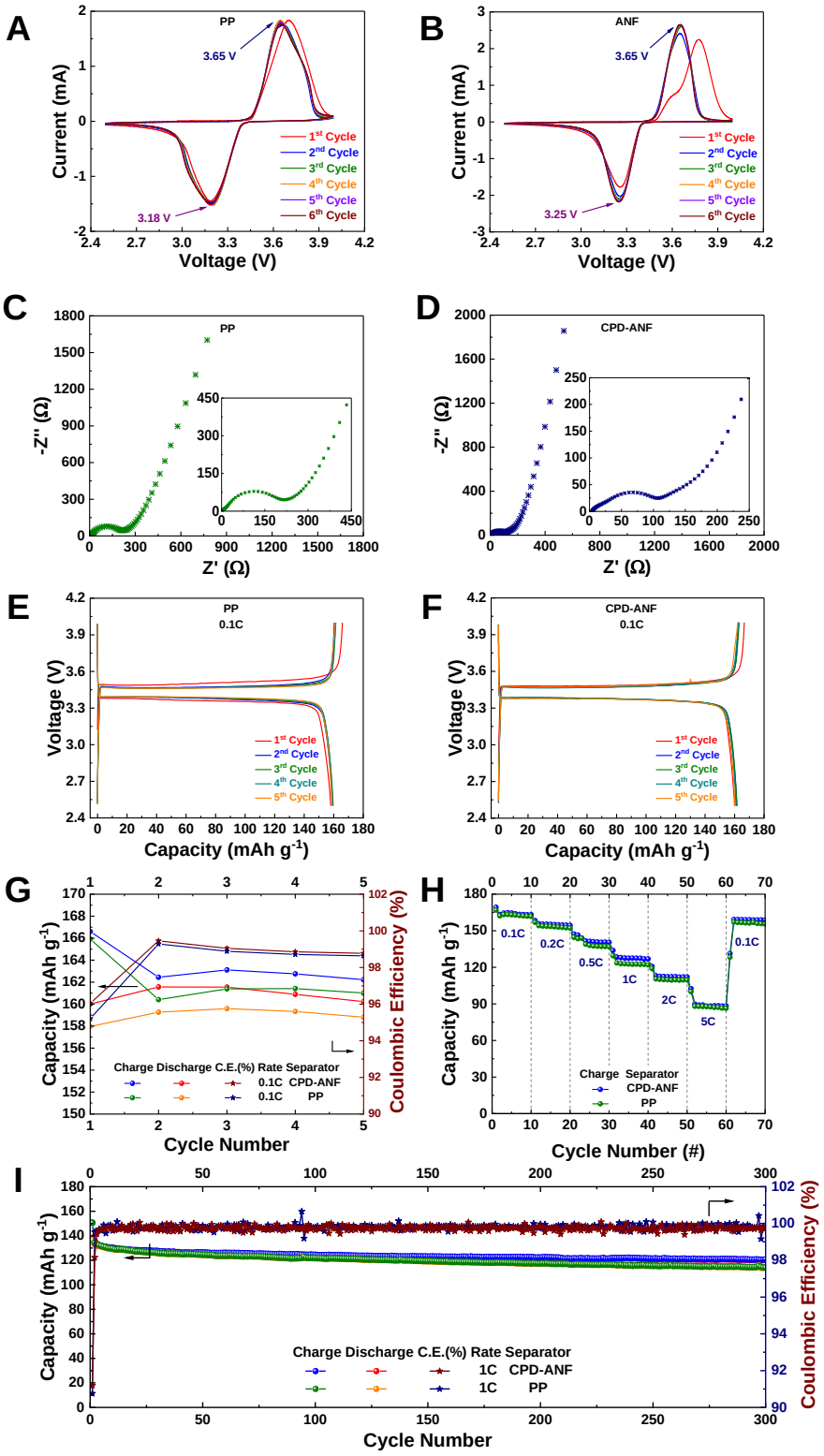

Figure 4.4: Electrochemical performance comparison between Celgard® PP and CPD-ANF with Li vs LFP half–cells. Cyclic voltammetry curves obtained at 0.2 mV s^{-1} of A: PP, B: CPD-ANF separators in the range 2.5–4.0 V. Electrochemical impedance spectra of C: PP, and D: CPD-ANF separators. Voltage characteristic profile for first 5 cycles at 0.1C for E: PP, and F: CPD-ANF separators. G: Galvanostatic cycling test for separators at 0.1C, and H: Rate performance from 0.1C to 5C for the separator cells.

The ultimate test for any energy storage system is its durability over time. Stable, long-term cycling for LIBs is essential to realizing the goal of high-power applications such as electric vehicles, grid storage, etc. To determine the cycle stability for the LIBs with different separators, cells were galvanostatically cycled between 2.5–4.0 V, at 1C (as shown in Fig. 4.5A). Celgard® PP separator, which is conventionally used is well-known to provide stable cycling. Here, it delivered stable 300 cycles, with only ~15% fade. The average charge-discharge capacity for the system were about 120.1/119.9 mAh g^{-1}. On the other hand, CPD-ANF delivered stable 300 cycles with just ~11% capacity fade. Also, the average charge-discharge capacity achieved was 123.8/123.4 mAh g^{-1}. The coulombic efficiencies for CPD-ANF had lower fluctuations compared to the Celgard® PP separator. These observations are congruent with the conducted rate study.

High-temperature cycling is an important aspect of realizing practical applications. Typically, at elevated temperature the kinetics of (de)-intercalation enhances, however, transport of Li^+ ions suffers due to modification in the separator structure. From thermal aging, the PP separator encounters pore length reduction, clogging, and reduction in mechanical strength, which decreases the effective transport parameters, and conductivity.[40] Figure 4.5B illustrates a cycling comparison between two separators at 40 °C. Celgard® PP separator cell had quite a disturbance during the initial cycling and capacity fade occurred with 40 cycles before attaining stability. An average charge-discharge capacity of 123/122 mAh g^{-1} was delivered. CPD-ANF demonstrates robust cycling over 200 cycles, with no fluctuations. Due to enhanced (de)-lithiation kinetics, average charge-discharge capacities of 140/139 mAh g^{-1} were achieved, higher than reached 25 °C. A capacity fade of just 10% was observed over 200 cycles.

The true performance of LIB can be observed in presence of limited Li^+ ions, and this limitation exists in the full–cells. After the consumption of partial Li^+ ions in the formation of SEI and CEI layers, the balance Li^+ ions shuttle across to deliver useful work.[41] Here, the full–cell comprising of LFP cathode, CPD-AND separator, MCMB anode, and electrolyte was fabricated. The cell was provided with formation cycles consisting of the first cycle at 0.05C, followed by two cycles at 0.1C. This allows for the complete formation of the solid electrolytic interfacial layers on the electrodes. Following this, the cell was subjected to cycling between 2.5–3.8 V, at 1C. The cell provided stable 100 cycles with 5.7% capacity fade. The average charge-discharge capacities of 107/106 mAh g^{-1} were achieved.

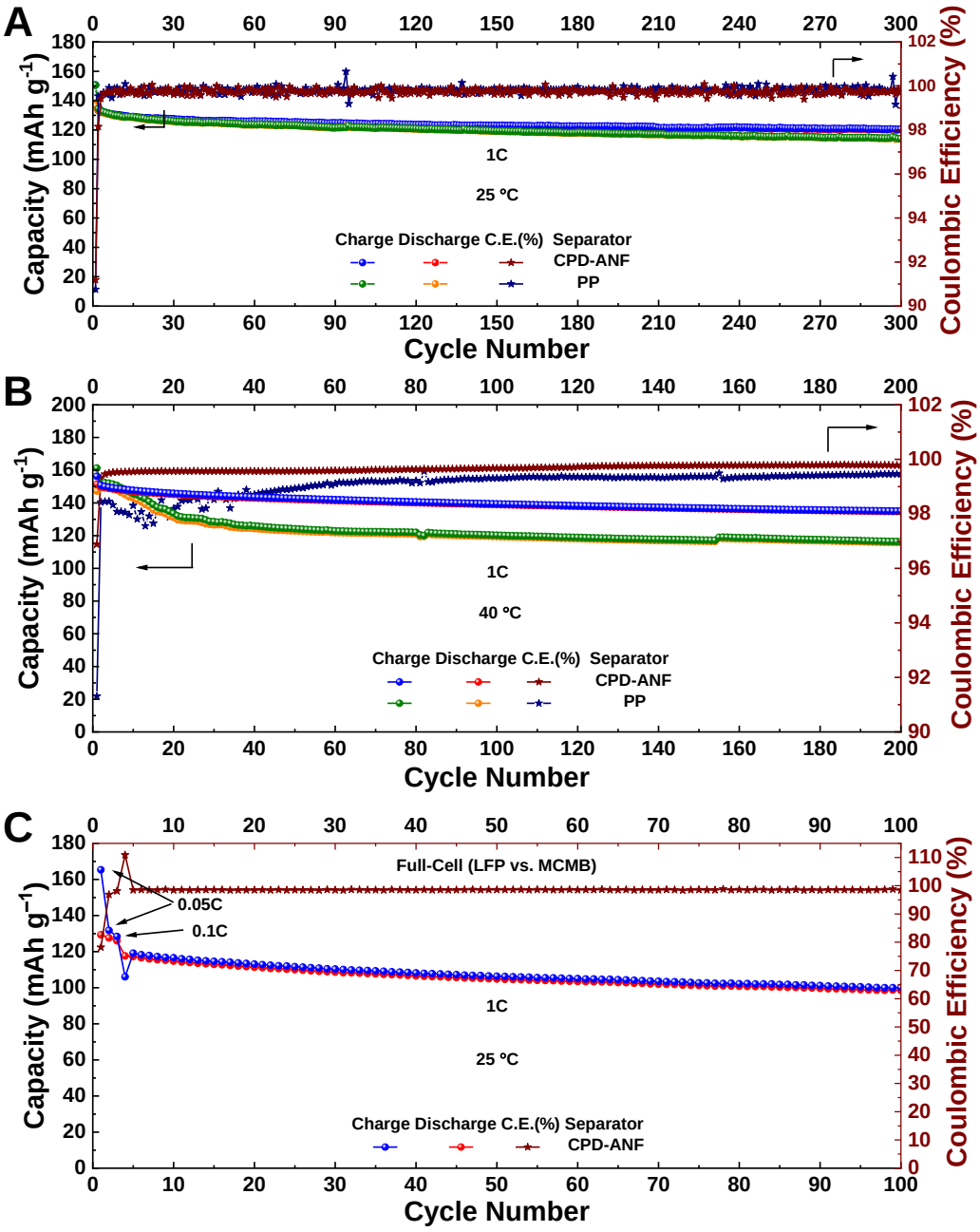

Figure 4.5: Galvanostatic cycling performance of PP and CPD-ANF separators in LFP half–cells at A: 25 ℃, B: 40℃; and C: Full–Cell Performance of LFP-MCMB chemistry with CPD-ANF separator at 25 ℃.

Thermal Safety

The DSC shown in Fig. 4.6A indicates that CPD-ANF exhibited no change in the thermal behavior up to 400 ℃, whereas we have previously reported that Celgard® PP exhibited melting and recrystallization at 165 ± 2 ℃ and 113 ± 1 ℃, respectively.[42] The absence of heat changes for CPD-ANF separators indicated their usage in high-temperature applications. On the other hand, the Celgard® PP undergoes structural modifications that can possibly lead to short circuits and a catastrophic failure such as a subsequent thermal runaway of the battery.[43]

For mechanistic elucidation of the thermal safety aspects of the systems, they were subjected to multimodule calorimetry (MMC), which conducts the calorimetry experiment on practical coin-cells to avoid artifacts, which may be generated from the DSC. Since all the components of LIBs are present in the MMC, the thermal signature observed provides an enhanced understanding of safety features from interactions amongst the components at high-temperature.[44] Full–cells with CPD-ANF and PP separators were provided 100 cycles and then charged to 100% SOC before subjecting to high temperatures inside the MMC. The electrolyte content of the cell with PP separator had ~26 mg and for CPD-ANF ~ 48 mg. The thermal heat signatures observed for the cells when heated from room temperature to 300 ℃ are shown in Fig. 4.6B. The cells opened up around 219 ℃ for PP compared to 185 ℃ for CPD-ANF. This may be due to electrolyte phase change that occurs at T > 80 ℃.[45] The peaks for the PP cell appeared more exothermic compared to those for CPD-ANF. The heat released before rupturing was ~243 J g^{-1} for CPD-ANF cell compared to 494 J g^{-1}. Voltage suddenly drops between 215 ℃ – 230 ℃. The voltage for the CPD-ANF cell remains steady until the collapse compared to that for the PP cell. This occurs due to the mechanical integrity of the structure, which is maintained by the CPD-ANF compared to PP separators after being exposed to high temperatures. Figure 4.6C shows the post-MMC diagnostic photographs of disintegrated cell components. For PP cells, current-collectors and spacers can be easily seen, however, no evidence of PP separator could be observed. Surprisingly, along with the previously observed components, the dark blackened CPD-ANF separator was uncovered, with structural shape intact.

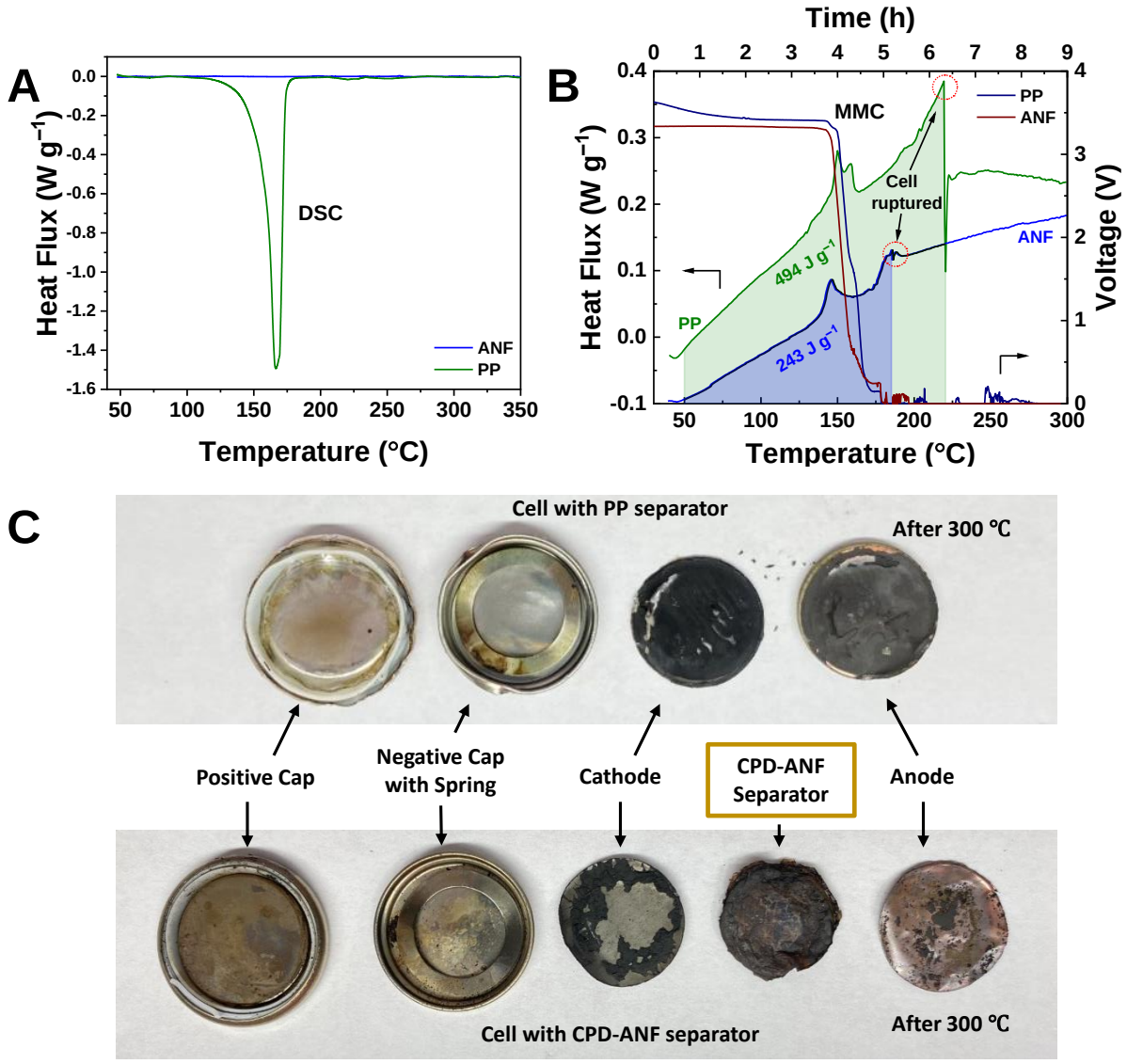

Figure 4.6: Thermal safety characterization of PP and CPD-ANF separators. Thermal signatures from A: DSC; B: MMC; and C: The post-MMC diagnostic photograph of disintegrated CR-2032 cells with different separators.

4.5 Conclusions

Aramid nanofiber separators were fabricated by using vacuum-assisted self-assembly and dried using a critical point drying (CPD) process. The CPD was carried out to retain the pore structure and porosity of these separators that is crucial for facilitating Li^+ ion transport. The separators exhibited excellent thermal stability with T_{peak} of 520 ℃ for CPD-ANF and no thermal behavior up to 400 ℃ compared to 398 ℃ for PP with phase change around 165 ℃. From multimodule calorimetry, the heat release before rupturing was 494 J g^{-1} for PP compared to just 243 J g^{-1}. After 300 ℃, the CPD-ANF separator held on to its mechanical integrity, whereas the PP separator was found missing. In terms of mechanical performance, CPD-ANF separators outperformed the commercial Celgard® PP membranes at room temperature (RT) and at 40℃. The CPD-ANF separators showed 110 ± 10% greater ultimate tensile strengths and 800 ± 50% higher Young's modulus than Celgard® PP. The electrochemical performance of CPD-ANF far exceeded that of PP in terms of cycle stability, rate capabilities, and cycle life at 40 ℃. The capacity fade for CPD-ANF separators was about 11% and 10% at 25 ℃ and 40℃ compared to 15% and 23% for PP after 300 and 200 cycles, respectively. CPD-ANF separators, exhibiting excellent mechanical performance and Li^+ ion transport at a wide range of temperatures, possess a high potential for high-performance Li-ion batteries. Additional work can be directed towards testing the operability of these separators at harsher conditions that can be found in aerospace environments.

4.6 Acknowledgement

VP truly thanks the financial support from the Office of Naval Research (Grant Nos. # N000142112070 and N00014-18-1-2397).

4.7 References

1. X. Huang, *Journal of Solid State Electrochemistry* **2010**, 15(4): p. 649-662.
2. H. Lee, M. Yanilmaz, O. Toprakci, K. Fu, and X. Zhang, *Energy Environ. Sci.* **2014**, 7(12): p. 3857-3886.
3. P. Zhai, K. Liu, Z. Wang, L. Shi, and S. Yuan, *Journal of Power Sources* **2021**, 499.
4. L. Zhang, X. Li, M. Yang, and W. Chen, *Energy Storage Materials* **2021**, 41: p. 522-545.

5. Q.-Q. Gu, H.-J. Xue, Z.-W. Li, J.-C. Song, and Z.-Y. Sun, *Journal of Power Sources* **2021**, 483: p. 229155.
6. J. Hao, G. Lei, Z. Li, L. Wu, Q. Xiao, and L. Wang, *Journal of Membrane Science* **2013**, 428: p. 11-16.
7. Y. Li, H. Pu, and Y. Wei, *Electrochimica Acta* **2018**, 264: p. 140-149.
8. G. Karimi and X. Li, *INTERNATIONAL JOURNAL OF ENERGY RESEARCH* **2013**, 37(1): p. 13-24.
9. L. Lu, X. Han, J. Li, J. Hua, and M. Ouyang, *Journal of Power Sources* **2013**, 226: p. 272-288.
10. B. Scrosati, J. Hassoun, and Y.K. Sun, *ENERGY & ENVIRONMENTAL SCIENCE* **2011**, 4(9): p. 3287-3295.
11. T.M. Bandhauer, S. Garimella, and T.F. Fuller, *Journal of The Electrochemical Society* **2011**, 158(3).
12. F. Leng, C.M. Tan, and M. Pecht, *Scientific Reports* **2015**, 5(1): p. 12967.
13. S. Ma, M. Jiang, P. Tao, C. Song, J. Wu, J. Wang, T. Deng, and W. Shang, *Progress in Natural Science: Materials International* **2018**, 28(6): p. 653-666.
14. J. Lin, S.H. Bang, M.H. Malakooti, and H.A. Sodano, *ACS Appl Mater Interfaces* **2017**, 9(12): p. 11167-11175.
15. B. Yang, L. Wang, M. Zhang, J. Luo, Z. Lu, and X. Ding, *Advanced Functional Materials* **2020**, 30(22).
16. J. Li, W. Tian, H. Yan, L. He, and X. Tuo, *Journal of Applied Polymer Science* **2016**, 133(30).
17. J. Liu, J. Wang, L. Zhu, X. Chen, Q. Ma, L. Wang, X. Wang, and W. Yan, *Chemical Engineering Journal* **2021**, 411.
18. X. Zhang, Q. Sun, C. Zhen, Y. Niu, Y. Han, G. Zeng, D. Chen, C. Feng, N. Chen, W. Lv, and W. He, *Energy Storage Materials* **2021**, 37: p. 628-647.
19. J. Shiju, F. Al-Sagheer, and Z. Ahmad, *Polymers (Basel)* **2020**, 12(11).
20. L. Si, Z. Lu, C. Yao, Q. Ma, Y. Zhao, Y. Wang, D. Wang, and Z. Jin, *Journal of Materials Science* **2020**, 55(14): p. 5948-5960.
21. L. Wang, M. Zhang, B. Yang, J. Tan, and X. Ding, *ACS Nano* **2020**, 14(8): p. 10633-10647.
22. Y. Yang, C. Huang, G. Gao, C. Hu, L. Luo, and J. Xu, *Carbohydr Polym* **2020**, 247: p. 116702.

23. G. Xu, M. Li, T. Wu, and C. Teng, *Reactive and Functional Polymers* **2020**, 154.
24. A. Patel, K. Wilcox, Z. Li, I. George, R. Juneja, C. Lollar, S. Lazar, J. Grunlan, W.E. Tenhaeff, and J.L. Lutkenhaus, *ACS Appl Mater Interfaces* **2020**, 12(23): p. 25756-25766.
25. B. Yang, L. Wang, M. Zhang, W. Li, Q. Zhou, and L. Zhong, *Journal of Materials Chemistry A* **2021**, 9(22): p. 12923-12946.
26. E.L. Artem, V.M. Natalia, I.K. Illarion, and A.K. Roman, *Journal of Non-Crystalline Solids* **2021**, 553: p. 120475.
27. A.V. Rao, D. Haranath, G.M. Pajonk, and P.B. Wagh, *Materials Science and Technology* 14(11): p. 1194-1199.
28. K. Sridhar and R. Claire, *Journal of the European Ceramic Society* **1996**, 16(2): p. 143-147.
29. J. Estella, J.C. Echeverra, M. Laguna, and J.J. Garrido, *Journal of Porous Materials* **2008**, 15(6): p. 705--713.
30. W. Fan, X. Zhang, Y. Zhang, Y. Zhang, and T. Liu, *Composites Science and Technology* **2019**, 173: p. 47-52.
31. A.E. Lebedev, N.V. Menshutina, I.I. Khudeev, and R.A. Kamyshinsky, *Journal of Non-Crystalline Solids* **2021**, 553(October 2020): p. 120475.
32. P.H. Tewari, A.J. Hunt, and K.D. Lofftus, *Materials Letters* **1985**, 3(9): p. 363-367.
33. A. Venkateswara Rao, D. Haranath, G.M. Pajonk, and P.B. Wagh, *Materials Science and Technology* **1998**, 14(11): p. 1194-1199.
34. C.A. García-González, M.C. Camino-Rey, M. Alnaief, C. Zetzl, and I. Smirnova, *The Journal of Supercritical Fluids* **2012**, 66: p. 297-306.
35. M. Yang, K. Cao, L. Sui, Y. Qi, J. Zhu, A. Waas, E.M. Arruda, J. Kieffer, M.D. Thouless, and N.A. Kotov, *ACS Nano* **2011**, 5(9): p. 6945-6954.
36. X. Feng, M. Ouyang, X. Liu, L. Lu, Y. Xia, and X. He, *Energy Storage Materials* **2018**, 10: p. 246-267.
37. A.K. Padhi, K.S. Nanjundaswamy, and J.B. Goodenough, *Journal of The Electrochemical Society* **1997**, 144(4): p. 1188–1194.
38. M.F. Lagadec, R. Zahn, and V. Wood, *Nature Energy* **2018**, 4(1): p. 16-25.
39. G.Y. Gor, J. Cannarella, C.Z. Leng, A. Vishnyakov, and C.B. Arnold, *Journal of Power Sources* **2015**, 294: p. 167-172.

40. R. l'Abee, F. DaRosa, M.J. Armstrong, M.M. Hantel, and D. Mourzagh, *Journal of Power Sources* **2017**, 345: p. 202-211.
41. M. Palanisamy, M.H. Parekh, and V.G. Pol, *Adv. Funct. Mater.* **2020**.
42. A. Patel, K. Wilcox, Z. Li, I. George, R. Juneja, C. Lollar, S. Lazar, J. Grunlan, W.E. Tenhaeff, and J.L. Lutkenhaus, *ACS Applied Materials & Interfaces* **2020**, 12(23): p. 25756-25766.
43. J. Deng, C. Bae, J. Marcicki, A. Masias, and T. Miller, *Nature Energy* **2018**, 3(4): p. 261-266.
44. M.H. Parekh, A.D. Sediako, A. Naseri, M.J. Thomson, and V.G. Pol, *Advanced Energy Materials* **2019**.
45. M.H. Parekh, B. Li, M. Palanisamy, T.E. Adams, V. Tomar, and V.G. Pol, *ACS Applied Energy Materials* **2020**.

5. SEPARATORS: MODIFIED MICROPOROUS MEMBRANES FOR LITHIUM-SULFUR BATTERIES

Mihit H.Parekh,[1] Deep Jokhakar,[1,2] Harsha Rao,[1] Vihang P.Parikh,[1] Manikandan Palanisamy,[1] Vilas G. Pol[1]

[1]Davidson School of Chemical Engineering, Purdue University, West Lafayette, IN 47907
[2]Brightvolt Incorporation, 7970 S Energy Dr, Newberry, IN 47449

This work is under the peer review process. Electrochemical testing and data analysis were carried out by Mihit H. Parekh. Material characterization was done by Mihit H. Parekh and Harsha Rao. Vihang Parikh and Deep Jokhakar provided technical inputs and designing the pouch cells. Deep Jokhakar assembled the pouch cells at BrightVolt Incorporation, IN, USA. Manuscript preparation was done by Mihit H. Parekh.

5.1 Overview

Conventional cathodes have capacities <250 mAh g^{-1}, and lithium-ion batteries cannot keep up with the ever-growing demand from high power and energy-dense applications. Being the lightest, abundant, and most economical cathode with extremely high theoretical capacity sulfur is an attractive option. However, the chemistry suffers from critical issues viz., poor sulfur conductivity, polysulfide shuttling, and lithium dendrite growth. Here, through the use of a tailored separator, comprising of graphene-polydopamine coat on a standard Celgard® polypropylene separator, all the issues were tackled simultaneously. Functionalized separator acted as a barricade for polysulfide from shuttling by adsorbing them preferably due to their favorable interactions with functional groups of polydopamine on the surface and outperformed the pristine separator. At –25, 0, 25, 40, and 50 ℃, the cells yielded about 170, 350, 580, 360, 550 mAh g^{-1} capacity, respectively. The system delivered 100 cycles at 50℃ followed by 300 cycles at 40 ℃. The capacity retention of 95% at 0.5C was reported after being exposed to high rates of 3C and 4C. A similar stable performance was observed with single-layered pouch cells. High-performance Li-S batteries proposed here can be valuable to a variety of applications like defense, transportation, and space explorations, where drastic conditions affect the battery functionalities, in the coming times ahead.

5.2 Introduction

Lithium-ion batteries (LIBs) are one of the technologies that have revolutionized human life beyond imagination.[1, 2] We have become heavily dependent on them for our day-to-day affairs. LIBs have been incorporated into portable consumer appliances, defense applications, and electric vehicles (EVs).[3] In LIBs, various high theoretical specific capacity anode materials like silicon (3596 mAh g^{-1}),[4] tin (993 mAh g^{-1}), antimony (660 mAh g^{-1}), carbon (372 mAh g^{-1}),[5] and their composites have been extensively developed in the past thirty years. Subsequently, promising cathode materials like $LiCoO_2$, $LiMn_xNi_yCo_zO_2$ (x+y+z = 1), $LiFePO_4$, $LiMn_2O_4$ have been used.[6] However, the practical specific capacities of these cathodes are < 250 mAh g^{-1},[7] and hence thicker cathodes are required to match with the anodes' capacities. Thicker cathode comes with several issues of capacity fade due to high overpotentials during cycling, high impedance for electrons, higher current densities on separators (causing more overpotentials), potential lithium plating, and impedes mass transfer of Li^+ ions.[8, 9] Also, LIBs cannot cope with the ever-increasing demand for more power and energy-consuming applications like energy grids, electric vehicles (EVs), etc.[10] This would require a significant increment in the energy density, capacity, and reduction in the cost of raw materials of the system. In this scenario, sulfur can be used as one of the alternative cathodes in the lithium-ion shuttling system for high-power applications.[3]

Sulfur is the lightest cathode, and has attractive properties viz., the high theoretical specific capacity of 1672 mAh g^{-1}, high energy density (2600 Wh kg^{-1}), abundant, and inexpensive (~$50 per metric ton).[3,11] Other advantages of transitioning from conventional insertion cathodes to sulfur apart from high capacity are eco-friendly nature and improved safety from the lower operational voltage (2.15 V vs Li/Li^+). Sulfur would have a crucial role to play for the advanced next-generation batteries.[11] Sulfur chemistry is quite old, about 50 years back it was used as primary batteries, and since the last decade has garnered attention for an inexpensive alternative to rechargeable Li^+ ion technologies. There are a few critical issues to be dealt with before the goal can be realized viz., the electrically insulative nature of sulfur (5×10^{-30} S cm^{-1} at 25 °C), volume expansion effects, polysulfide shuttling effect, and dendritic growth of metallic lithium.[3, 11-13] Low conductivity of sulfur generates inadequate electrochemical contact of active material, increased internal battery resistance, and subsequently, large polarization. Octasulfur (cyclo-S_8) undergoes morphological and structural transformations during the redox process to form insoluble, and poor ionic conductive short-chain polysulfides i.e., Li_2S & Li_2S_2, and soluble long-chain

polysulfides i.e., Li_2S_X ($8 \leq X \leq 3$) in liquid electrolyte. The insoluble polysulfides on the sulfur surface prevent further reduction in discharging process and the soluble polysulfides shuttle across the separator. These unwanted characteristics lead to inefficient active material utilization, poor safety assurance, poor system energy efficiency, and drastically low cycle life.[14]

To tackle the conductivity issue of sulfur and polysulfide shuttling effect, the following approaches have been taken a) impregnation of sulfur in mesoporous materials like carbon;[15-17] b) using metal sulfides or oxides, which form bonds with polysulfides;[18-21] c) coating sulfur with conductive polymers;[22] d) using metallic organic frameworks or covalent organic frameworks;[23-25] e) inverse vulcanization using sulfur as the main chain;[26, 27] f) fabricate cathode comprising of SeS.[28, 29] However, some of these approaches, lead to lowering of the energy density of the system, involve complex fabrication steps or raw materials are expensive. To address the issue of lithium metal dendrites growth, exotic electrode coatings, electrolytic additives, special shutdown separators are used.[30] Nevertheless, the specified approaches impede cell performance in line with high-cost procedures. Therefore, an alternative commercially viable approach is modifying polypropylene (PP) separator, as it can easily resolve the coulombic efficiency issue of Li-metal batteries, and cycle performance at critical temperatures.

Herein, we report the proposed hypothesis that, use of surface tailored separator for sulfur-carbon (SC) cathode for trapping polysulfide, curbing dendrites growth and mitigating their propagation. In previous studies, it has been reported that polydopamine (PDA) coated separators have better ionic conductivity and wettability and positively affect electrochemical performance.[31, 32] Then the graphene coating on the PDA-coated separator supports accommodating volume expansion of SC electrode during cycling as well as enhancing local electrical conductivity. The tailored separator acted as a barrier in preventing the shuttling of polysulfide by adsorbing them preferentially due to the unique characteristic of the hydrophilic nature of the separator.

5.3 Experimental Section

5.3.1 Preparation of SC Cathode

Sulfur powder (Sigma Aldrich), carbon black (Timken Co.), PVdF HSV900 (Arkema) were taken in the ratio of 60:30:10. The sulfur powder was hand-milled with carbon black for 1 h. The mixture was then mixed with 10% w/w HSV900 binder in N-methyl pyrrolidone solvent. The

slurry was mixed in Thinky planetary mixed for 40 mins at 2000 rpm. To achieve the desired loading, an appropriate wet gap was chosen and the slurry was cast on the aluminum current collector. The laminate was dried in fumehood for 30 minutes and then in a vacuum oven at 50 ℃ for 3 h. The dried laminate was calendered for desired porosity of 35-40% and then punched into the electrode discs. The loading weight of the electrodes was ~3 mg cm^{-2}.

5.3.2 Preparation of PDA-tailored separator

The surface functionalization of pristine separator was completed by submerging it into the dopamine solution (10×10^{-3} m), which was prepared from Tris-buffer solution (pH 8.5) and methanol, similar to previous literature.[31, 32] After 5 h, the treated separator was removed from the solution, and washed with sufficient deionized water. The tailored separator was dried in the vacuum oven at 50 °C for 20h.

5.3.3 Preparation of Graphene Layer Coated PDA-Separator

As to the preparation of aqueous slurry for graphene coating, 90 mg graphene nanosheet powder and 10 mg CMC binder (sigma Aldrich) were dispersed in DI water by a planetary mixer (Thinky). The prepared graphene-CMC (Gr-CMC) slurry was thinly cast onto the PDA-separator and then dried in the vacuum oven at 50 °C for 20 h.

5.3.4 Preparation of single-layered pouch cells

The electrodes dimensions were 6.6×3.8 cm^2 with areal loading of ~2 mg cm^{-2}. The separator dimensions were 6.9×4.2 cm^2. The electrolyte quantity added was ~20 μL mg^{-1}. The tailored separator with graphene-PDA faced SC composite cathode. The total capacity of the single-layered pouch cell was ~20 mAh. Pouch cells were prepared in dry-room with humidity <1%, temperature ~18 ℃, and dew point temperature set at –40 ℃.

5.3.5 Electrochemical Characterization

After the laminate is dried, circular electrodes of 14.9 mm diameter were punched and stored under vacuum before assembling CR2032 coin cells (MTI Corporation) to study the electrochemical behavior. The cell construction was done in inert conditions inside the glovebox,

which is filled with 99.998% argon having O_2 and H_2O concentration <1 ppm. Cells comprised of the SC cathode, electrolyte, Celgrad® 2500 separator, and Li anode. The electrolyte consisted of 1% w/w $LiNO_3$ in 1 M LiTFSI dissolved in 1:1 DOL/DME solution. Using Arbin cycler, galvanostatic cycling was performed within the voltage range of 1.7 – 2.8 V and the current rate of 0.1C, 0.2C, 0.5 C, 1C, 2C, and 4C. To determine the cycle stability of the SC composite, a constant current rate of 0.5C was applied. The specific capacities were determined from the active ingredient weight of the electrodes (the weight of HSV900 PVdF binder and carbon black C65 were excluded). Gamry-600 reference system was used for performing cyclic voltammetry and electrochemical impedance spectroscopy. CV was measured at a scanning rate of 0.2 mV s^{-1} from 1.7 V to 2.8 V, while EIS measurements after cell construction was recorded through 10 mV amplitude AC voltage perturbation operated over the frequency range 1 MHz – 0.01 Hz. All the potentials mentioned are versus Li+/Li.

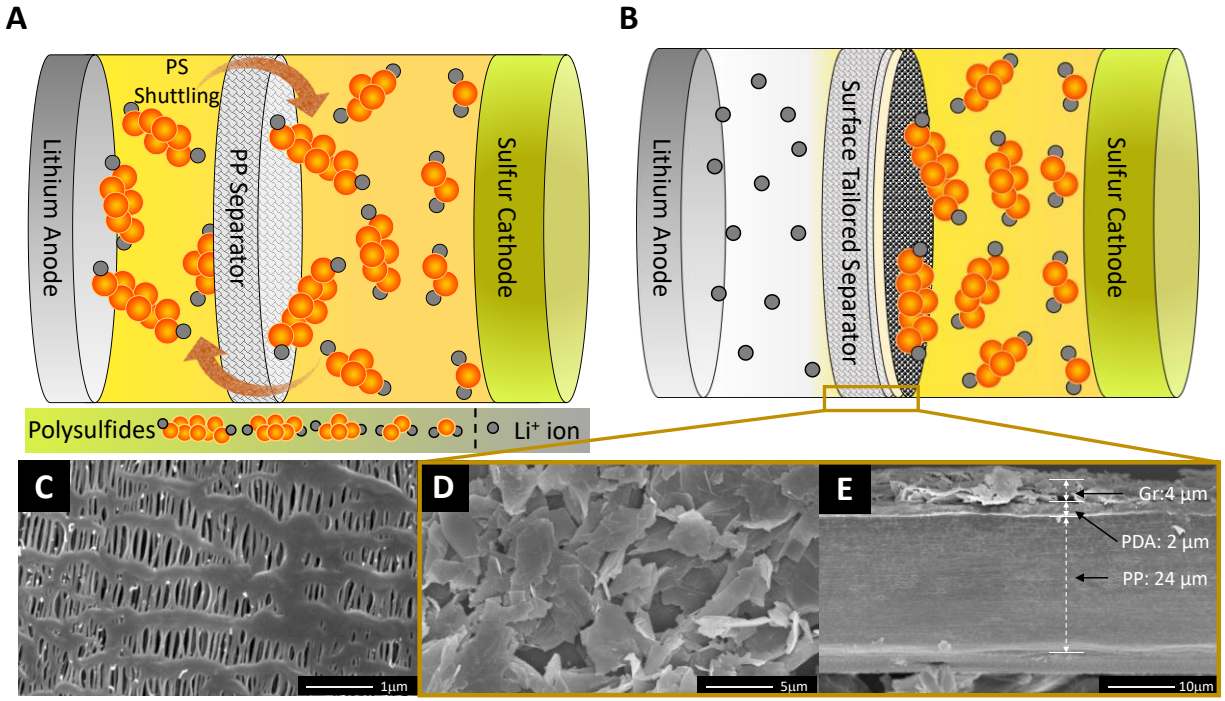

Figure 5.1: Schematic representation of LiS chemistry in batteries. A: Presence of polysulfide shuttling effect in presence of polypropylene separator; B: Suppression of polysulfide shuttling effect with the presence of tailored separator. High resolution scanning electron microscopy of separators, C: Top-view of polypropylene separator, D: Top-view of tailored separator containing graphene particles, and E: Cross-sectional view of the tailored separator illustrating graphene, and polydopamine layers on polypropylene separator.

5.4 Results & Discussion

Figure 5.1 shows a schematic of LiS batteries in presence of a conventional PP separator and tailored separator. In a conventional setup, shown in Fig. 5.1A, the polysulfides easily shuttle across the separator leading to a reduction in coulombic efficiency and side reactions on the anode surface. Also, the dendritic growth occurs on the surface of Li, which can eventually pierce through the separator causing short-circuit leading to fire or explosion in extreme cases. However, the tailored separator, which has layers of polydopamine, and graphene behaves like a physical barrier to block the shuttling of polysulfides, as shown in Fig. 5.1B. Figure 5.1C-E depicts high-resolution SEM images of polypropylene separator, top view, and cross-sectional view of the surface tailored separator. Flaky natured graphene coated on the PP separator can be observed in Fig. 5.1D. The polydopamine layer on PP is ~2 μm with the majority of PDA imbibed inside the PP separator, and the graphene-CMC binder coating on the PDA layer is about 4 μm. The thinner layers facilitate the easy exchange of Li^+ ions across the separator.

X-ray diffraction, Raman spectroscopy, BET adsorption, and DLS particle size distribution was performed on the carbon-sulfur composite material to study the phase purity, crystallinity, porosity and surface area, and particle size distribution, respectively. To understand the effect of temperature on ionic conductivity of the electrolyte, it was analyzed on Autolab Microcell HC with TSC1600 cell. Figure 5.2 A shows the XRD pattern of SC composite. In comparison with Orthorhombic Fddd JCPDS # 83-2283, the crystal structure of the sulfur appeared to be Fddd orthorhombic with major characteristic peaks appearing at 23.06°, 25.86°, and 27.72°.[33, 34] Raman spectra of the SC composite and elemental sulfur are shown in Fig. 5.2B. For elemental sulfur, characteristic bands are observed at 155, 220, and 474 cm^{-1}. For SC composite, there are characteristic bands seen at 1324 and 1592 cm^{-1}, which are occurring from the resonance of D-band and G-band stretching of carbon. The features of sulfur are suppressed by the bands of carbon with a slight bulge being noticed in the lower range of wavenumber.

Figure 5.2C shows nitrogen adsorption isotherms for SC composite and it represents a mixed type I and II isotherms based on the relative pressure (P/P_0). At high P/P_0, the majority volume is adsorbed indicating macroporous or non-porous structure. In the low and intermediate P/P_0 range, the adsorption is due to the microporous structure of C-65 and the outer mesoporous surface, respectively. The Brunauer–Emmett–Teller (BET) surface area of the SC composite was found to be 11.35 $m^2 g^{-1}$. From the pore size distribution, the composite exhibits micropores (<2

nm), mesopores (2–5 nm), and medium coarse mesopores (>10 nm) distribution (Fig. 5.2D). This suggests that there might be pore accumulation occurrence in the composite. The hand-milled SC composite was characterized by NanoBrook 90Plus PALS analyzer, where the sample was dispersed in ethanol and sonicated to break the aggregates. The d_{90} value of the SC composite is 131 nm as illustrated in Fig. 5.2E.

As Li-S chemistry requires a combination of specific solvent(s), lithium salt(s), and additives(s) to function in operating voltage range while having stability with pure lithium metal, we prepared an in-house electrolyte with 1M LiTFSI in 1:1 (v/v) DOL:DME with 1 wt% $LiNO_3$. To characterize this electrolyte, conductivity at various temperatures was measured to calculate Arrhenius parameters and compared with other electrolytes reported in the literature. Autolab Microcell HC has the ability of a typical potentiostat and combines temperature-controlled chamber with cell. Measurement of EIS at OCV with frsequency in the range of 1 MHz to 1 Hz at various temperatures was done. Conductivity calculations are based on the charge transfer resistance. The EIS at room temperature and Arrhenius plot are shown below in Fig. 5.2F. A linear fitting provides the slope, which is equal to the ratio of activation energy and gas constant. Based on our experiment, activation energy is 0.073 eV, and this is comparable to values available in the literature.[35] Hence, the control experiment is comparable to other studies.

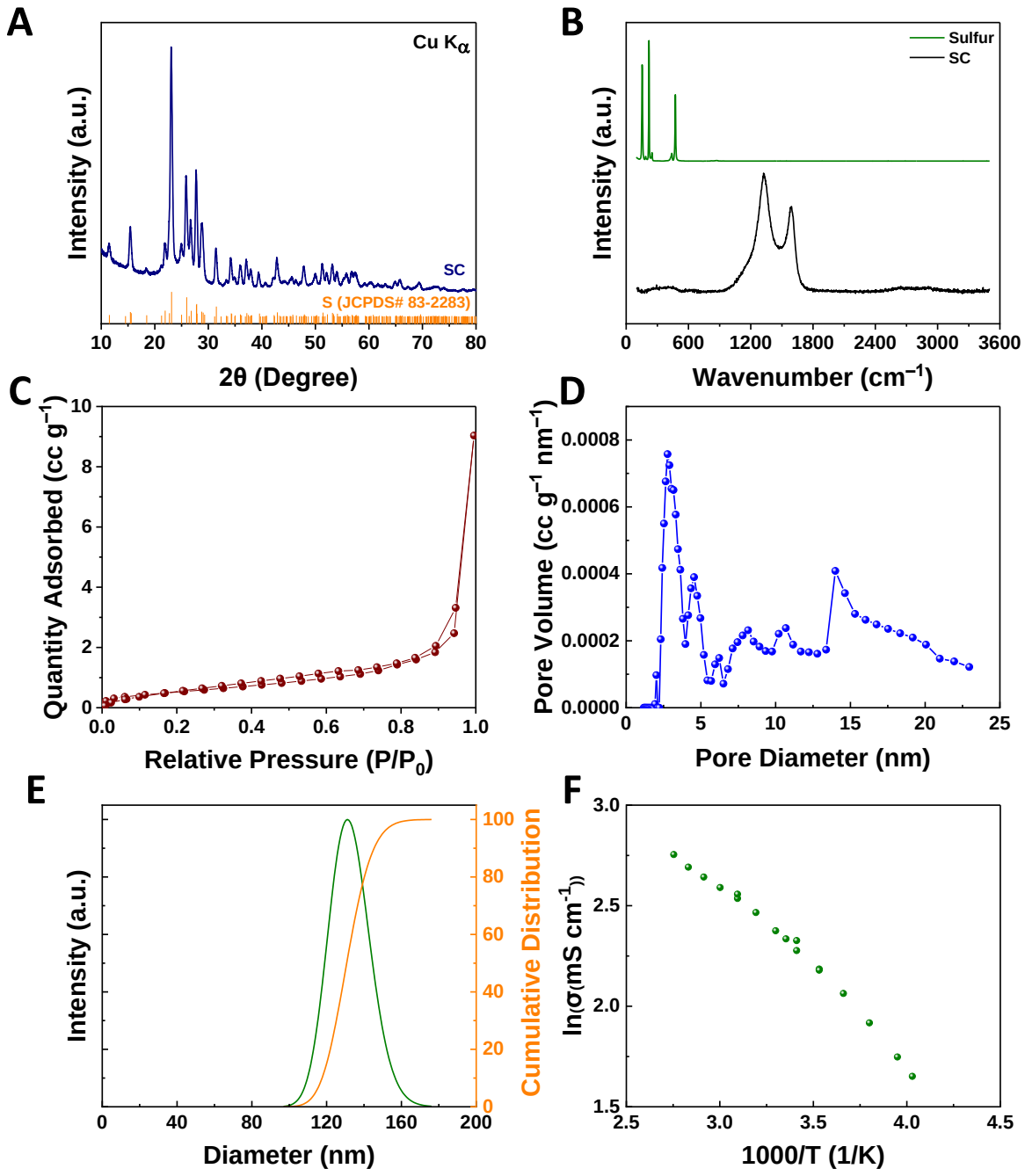

Figure 5.2: A: XRD patterns of SC, Sulfur; B: Raman Spectra of SC composite, and sulfur; C: Adsorption isotherm for SC composite; D: Pore size distribution of SC composite, E: PALS Particle size distribution for the SC composite; and F: Conductivity of the electrolyte at different temperatures.

Figure 5.3 shows the electrochemical performance of the SC cathode with a tailored separator and with a pristine separator at room temperature, 25°C. Figure 5.3A depicts the cyclic voltammetry of SC cathode in the presence of a pristine and tailored separator. Though the anodic process of the Li extraction is simple and is analogous to other carbon-based cathodes, however, the cathodic process is divided into multiple redox steps for the Li insertion. Two reduction peaks are observed around 2.04V and 2.3V. Overlapping oxidation peaks are observed between 2.33 and 2.55 V. To analyze the interfacial behaviors of each sulfur electrode, electrochemical impedance spectroscopy (EIS) studies were carried out. The Ohmic resistance of pristine (Fig. 5.3B), and tailored separators (Fig. C.1) showed values of 5.1 Ω, and 2.5 Ω, respectively. Charge transfer resistance (R_{ct}) of each cell exhibited different values. The pristine separator cell showed a higher charge transfer resistance (22.3 Ω), compared with the tailored separator cell (12.8 Ω), indicating that the electrical conductivity of the cathode is enhanced by the presence of graphene-PDA coated separator. Also, tailored separator cells showed a prominent Warburg diffusion element as compared to pristine separator cells.

Figure 5.3C demonstrates rate studies of SC cathode showing the specific capacities. Multi-rate galvanostatic cycling is exhibited at different rates between 0.1C and 4C. As can be seen in Fig. 5.3C, the capacity retention for 0.5C was ~ 93%. The tailored separator exhibited capacities of 925, 833, 644, 480, 326, 260, and 220 mAh g^{-1} at increasing C rates. Capacity retention for 0.5C rate was ~95%. Conversion-type cathode materials are less suited for fast charging applications and therefore, stellar performance is not observed above 2C.[36] Figure 5.3D shows the charge-discharge voltage characteristics of SC composite with tailored separator at 0.5C rate. Two discharge plateaus are observed at 2.38 V and 2.06 V, which are congruent to cathodic peaks seen in CV. At 0.5C rate, tailored separator exhibited a high charge-discharge capacity of 677/687 mAh g^{-1} compared to the cell with 663/713 mAh g^{-1} of pristine separator, shown in Fig. 5.3E. This drastic difference in the performance of cells by change in separators may be due to the formation of polysulfides pre-cycling, as a dark yellowish colored ring is observed around the SC composite electrode. The presence of graphene and polydopamine in the tailored separator prevents the polysulfides from shuttling across the separator by the physical adsorption phenomenon. Dopamine contains amine and catechol groups, which generate a hydrophilic environment on the surface of the PP separator and improves its wettability, uptake, and conductivity.[37] Hydrophilic surface allows for facile coating of graphene with Na-CMC binder on the PDA coated PP separator.

This hydrophilic natured graphene-PDA layer can successfully adsorb the polar polysulfides (typically long-chain polysulfides). The layer prevents the diffusion of polysulfides and also acts as a buffer to accommodate volume changes in the SC cathode. The coating of PDA on the PP separator blocks the channels on it, which in conventional separator provides the pathway for polysulfide dispersion.

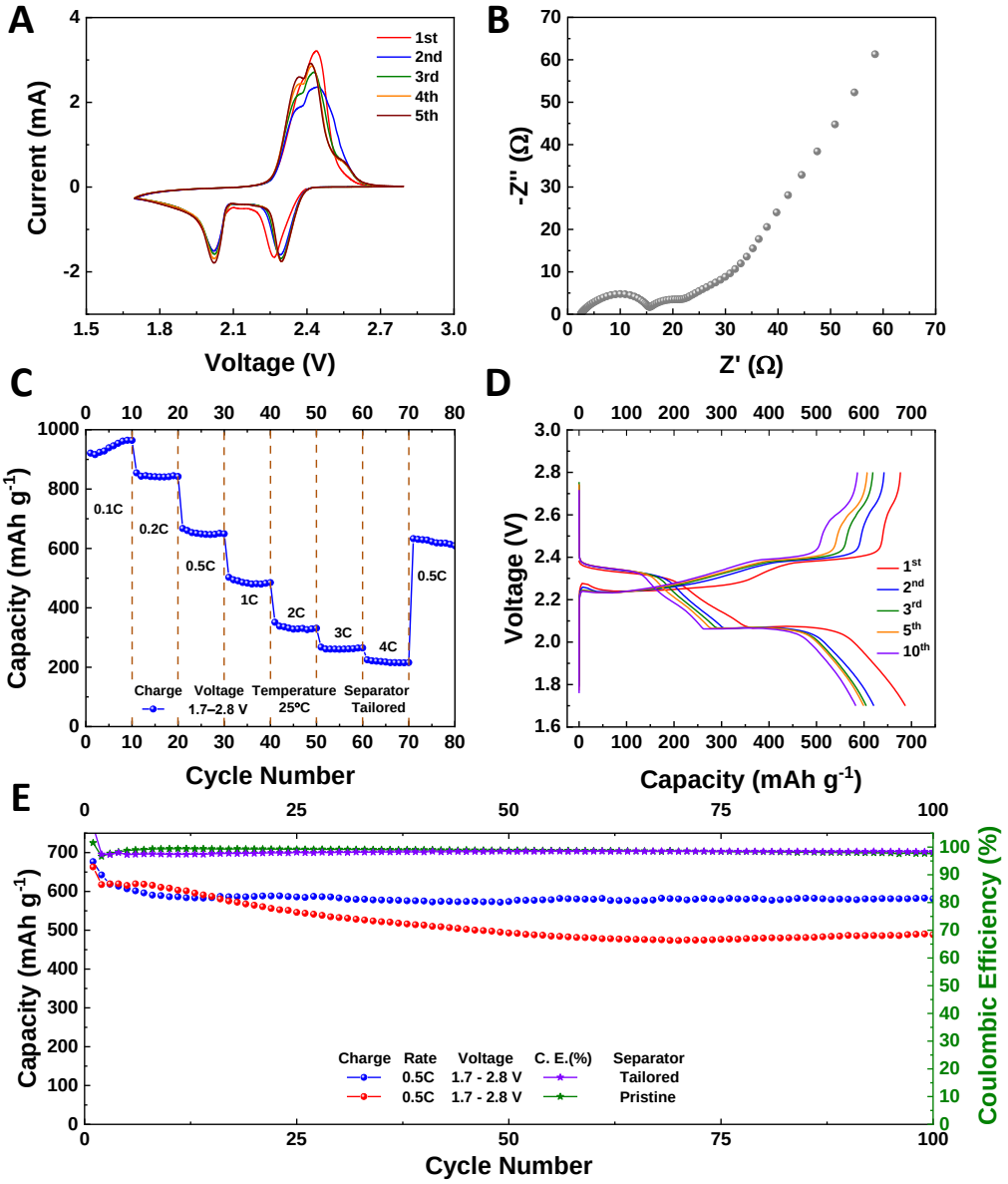

Figure 5.3: Electrochemical performance of Li-S cell. A: Cyclic voltammetry of Li-S cell with tailored separator at 25 °C; B: EIS of Li-S cell with tailored separator; C: Rate studies exhibiting performance at 0.1C, 0.2C, 0.5C, 1C, 2C, 3C, and 4C at 25 °C; D: Voltage characteristics of Li-S cells; and E: Cycling performance at 0.5C at 25 °C.

Energy-dense batteries would be expected to play important role in performance-critical applications like space, subsea, and defense. Conventional LIBs present tough challenges viz., low capacity, massive overpotential, and rate capabilities at low temperature. In such cases, Li-S batteries could play a major role as the primary reason why the batteries perform poorly at low temperatures is due to electrolyte and the co-solvents of Li-S batteries viz., DME and DOL have substantially low freezing points of –58 °C and –95 °C, respectively. This allows for the conduction of lithium ions at such low temperatures. As can be seen from Fig. 5.2F, the conductivity of electrolyte at –25 °C is >5 mS cm^{-1}. A startling performance was observed for cells at 0 °C for tailored separator, as shown in Fig. 5.4A, with the voltage characteristics resembling that of 25°C performance. The two distinct discharge plateaus were observed at 2.38 V and 2.02 V. Short-chain polysulfides contribute to the majority of the capacity for Li-S system, and it can be observed that as the temperature drops down, the formation of short-chain polysulfides is being suppressed resulting in lower specific capacity than 25°C. However, the cyclability of the tailored separator at 0.5C exhibits a stable cycling performance with an average capacity of about 392 mAh g^{-1} for 200 cycles. Astonishingly, the performance of SC cathode at –25 °C was phenomenal at C/25 rate. Figure 5.4C demonstrates the voltage profile at –25 °C, wherein there is drastic transformation compared to the at 25 °C and 0 °C. This visible stunted suppression of the second plateau region occurs due to aggregation behavior and degree of coordination of dominant electroactive polysulfide species Li_2S_4. This behavior at –25 °C causes clustering of aggregates in the electrolyte and inhibits the further conversion of the polysulfides. Another possible explanation for this behavior at low temperature may arise from the electrostatic interaction of Li^+ cation with salt anion and polysulfides. The affinity of Li^+ towards polysulfides leads to the networking of Li^+–S_x^{-2} and thus promoting clustering. Strong coordinating lithium salts can help support Li_2S_4 conversion to Li_2S and mitigate the clustering effect.[38] Nonetheless, a specific capacity of about 170 mAh g^{-1} was obtained with >99% coulombic efficiency at –25 °C (shown in Fig. 5.4D), which is still higher than extractable from conventional LIBs. The presence of a tailored separator apart from blocking the diffusion process, reinforced in achieving a high coulombic efficiency. In general, there is huge potential in empowering the Li-S battery for critical low-temperature conditions.

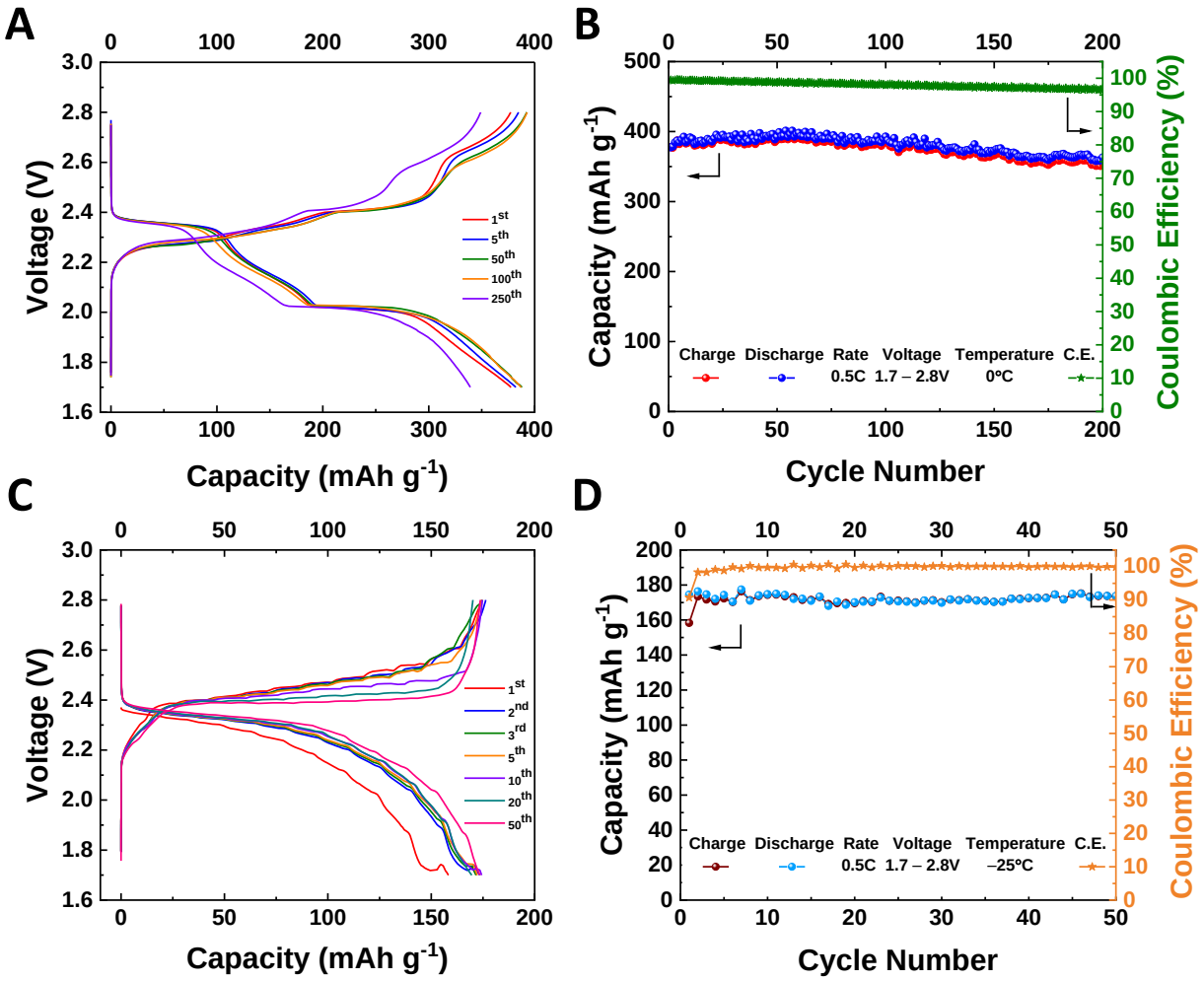

Figure 5.4: Electrochemical performance of Li-S cell at zero and negative temperatures. A: Voltage characteristics of Li-S cells at 0°C; and B: Cycling performance at 0.5C at 0 °C; C: Voltage characteristics of Li-S cells at –25°C; and D: Cycling performance at 0.5C at –25°C

High operating temperature for Li-S batteries promotes high polysulfide shuttling due to enhanced diffusion and kinetics parameters that lead to poor life cycles. These limitations have restricted the realization of Li-S batteries for temperature critical applications. However, the presence of the tailored separator should suppress the shuttling effect even at higher temperatures. To test the hypothesis, the cells were operated at 50 °C for 100 cycles, and then the temperature was reduced to 40 °C. The electrochemical performance of the system with the tailored separator is shown in Fig. 5.5. At elevated temperature, charge transfer resistance decreases, which can be seen in Fig. 5.5A, where R_s was observed to be 5.35 Ω and R_{ct} was 4.65 Ω. After 100 cycles, at 40 °C, R_S and R_{CT} were observed to be about 6.25 Ω and 5.99 Ω, respectively. The dual semicircle

of R_{ct} may occur from PDA reducing the pore size leading to little hinderance to ions while neighboring graphene enhances electronic conductivity. The voltage profile of the SC cathode as seen in Fig. 5.5B, resembles the ones observed for 25 ℃ and 0 ℃. The two plateaus during the discharge process were seen at 2.31 V and 2.06 V. Due to the faster kinetics, there is a slight reduction in the polarization compared to 25 ℃ and 0 ℃. On subsequent cycling, the polarization reduces even further at 40 ℃. The galvanostatic cycling demonstrated stable cycling at 50 ℃ followed by 40 ℃ (Fig. 5.5C). At 50 ℃ the SC cathode provided the initial capacity of 604 mAh g^{-1} and 499 mAh g^{-1} after 100 cycles. The coulombic efficiency was slightly lower than 99% indicating either side reactions occurrence or minor polysulfide shuttle effect. After 100 cycles, the capacity went to 400 mAh g^{-1} possibly due to enhanced kinetics at elevated temperature causing more polysulfide generations with ~79% capacity retention after 300 cycles. The coulombic efficiency was maintained at >98.5%

Evaluating the performance of energy material in larger configuration cells viz., pouch cell is a stepping stone towards realization for potential applications. Pouch cells have challenges in terms of larger areal capacity, which causes severe shuttling of polysulfides, and large areal current on the Li anode that leads to dendrite growth. Both these are detrimental to the practical realization of the Li-S batteries. The presence of tailored separator aides in suppressing PS and uniformly distributing large areal current on Li anode. Figure 5.5D shows the performance of Li-S pouch cell, which delivered an average capacity of 541 mAh g^{-1} with coulombic efficiency >98%.

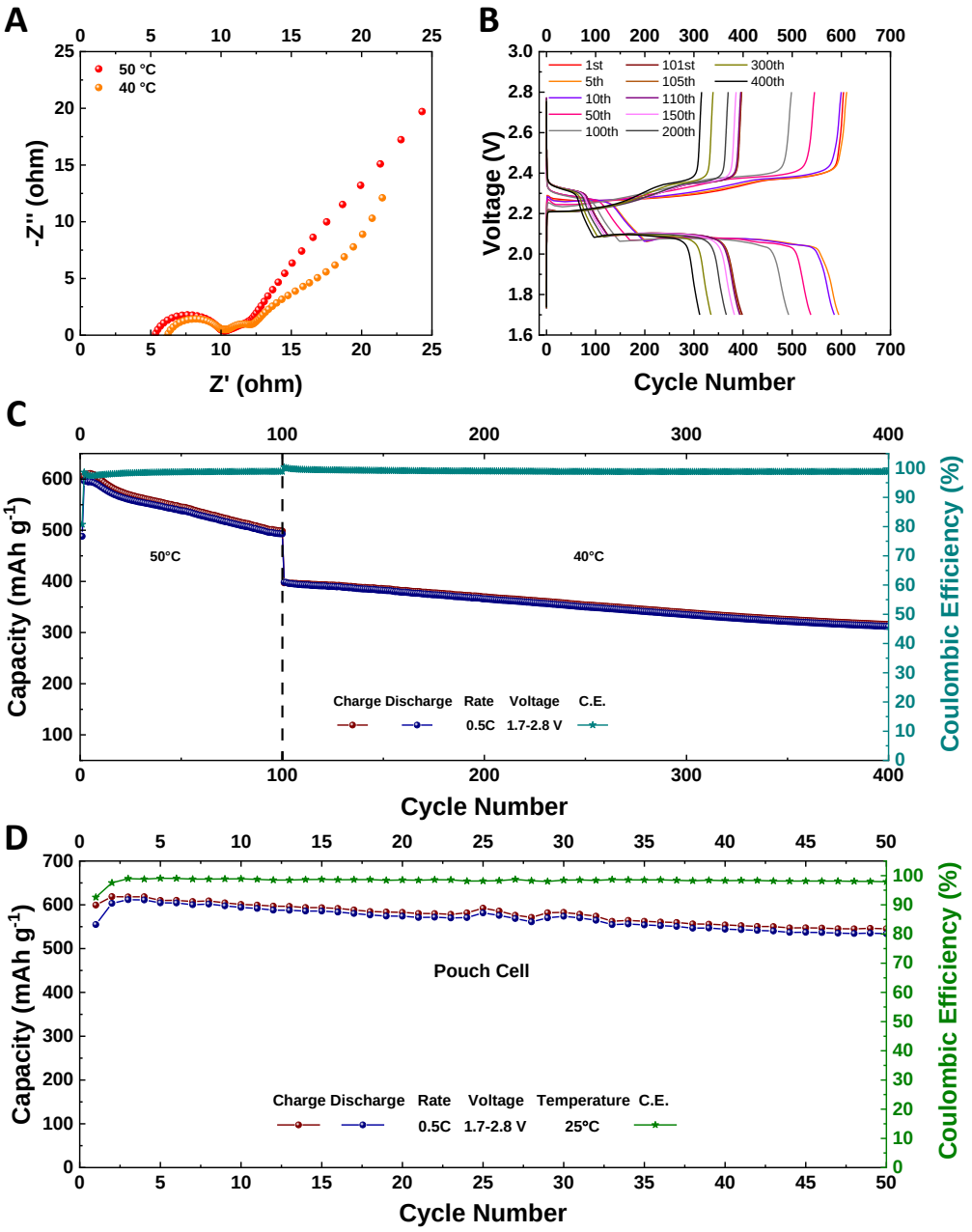

Figure 5.5: Electrochemical performance of Li-S cell at high temperatures of 40°C and 50°C. A: EIS of Li-S cell with tailored separator; B: Voltage characteristics of Li-S cells at 50°C and 40°C; C: Cycling performance at 0.5C for 100 cycles at 50 °C followed by 300 cycles at 40°C. D. Pouch cell Li/Graphene-PD-PP/CS

5.5 Conclusion

A tailored separator consisting of graphene–polydopamine coated on polypropylene was used to enhance the performance of Li-S batteries consisting of SC composite cathode and Li anode. The separator served multipurpose viz., blocked pathways for polysulfides shuttling with their preferential adsorption at graphene-PDA layer, enhanced electrical conductivity of SC cathode, and prevented the growth of dendrites by a uniform distribution of the areal current applied. The three critical issues of Li-S batteries were tackled using this approach. The electrochemical performance of the system was studied at –25 ℃, 0 ℃, 25 ℃, 40 ℃, and 50 ℃ and achieved stable cycling with specific capacity 170, 392, 580, 360, and 550 mAh g^{-1}, respectively. The presence of the tailored separator helped achieve stable 400 cycles at high temperatures when diffusion and kinetics are enhanced. The system had capacity retention of ~95% at 0.5C after exposure to high rates of 4C. Single-layered pouch cell delivered a capacity of 541 mAh g^{-1} at 0.5C. This strategic and promising approach will help in the advancement towards the commercialization of Li-S batteries.

5.6 Acknowledgement

VP truly thanks the financial support from the Office of Naval Research (Grant # N000142112070 and Program Manager, Maria Medeiros).

5.7 References

1. J.M. Tarascon and M. Armand, *Nature* **2001**, 414(6861): p. 359-367.
2. J.B. Goodenough and K.-S. Park, *Journal of the American Chemical Society* **2013**, 135(4): p. 1167-1176.
3. A. Eftekhari and D.-W. Kim, *Journal of Materials Chemistry A* **2017**, 5(34): p. 17734-17776.
4. H. Wu and Y. Cui, *Nano Today* **2012**, 7(5): p. 414-429.
5. M. Gaberscek, M. Bele, J. Drofenik, R. Dominko, and S. Pejovnik, *Electrochemical and Solid-State Letters* **2000**, 3(4): p. 171-173.
6. M. Armand and J.M. Tarascon, *Nature* **2008**, 451(7179): p. 652-657.
7. G. Gabrielli, M. Marinaro, M. Mancini, P. Axmann, and M. Wohlfahrt-Mehrens, *Journal of Power Sources* **2017**, 351: p. 35-44.

8. M.H. Parekh, A.D. Sediako, A. Naseri, M.J. Thomson, and V.G. Pol, *Advanced Energy Materials* **2019**.
9. J. Kasnatscheew, T. Placke, B. Streipert, S. Rothermel, R. Wagner, P. Meister, I.C. Laskovic, and M. Winter, *Journal of The Electrochemical Society* **2017**, 164(12): p. A2479-A2486.
10. J.B. Goodenough and Y. Kim, *Chemistry of Materials* **2010**, 22(3): p. 587-603.
11. P.J.H. Kim, K. Kim, and V.G. Pol, *Carbon* **2018**, 131: p. 175-183.
12. P.J. Kim and V.G. Pol, *Advanced Energy Materials* **2018**, 8(36): p. 1802665.
13. W. Xue, Z. Shi, L. Suo, C. Wang, Z. Wang, H. Wang, K.P. So, A. Maurano, D. Yu, Y. Chen, L. Qie, Z. Zhu, G. Xu, J. Kong, and J. Li, *Nature Energy* **2019**, 4(5): p. 374-382.
14. A. MANTHIRAM, Y. FU, and Y.-S. SU, *Accounts of Chemical Research* **2013**, 46(5): p. 1125–1134.
15. R. Sahore, B.D.A. Levin, M. Pan, D.A. Muller, F.J. DiSalvo, and E.P. Giannelis, *Advanced Energy Materials* **2016**, 6(14).
16. L. Borchardt, M. Oschatz, and S. Kaskel, *Chemistry* **2016**, 22(22): p. 7324-51.
17. A. Eftekhari and Z. Fan, *Materials Chemistry Frontiers* **2017**, 1(6): p. 1001-1027.
18. Y. Xia, B. Wang, X. Zhao, G. Wang, and H. Wang, *Electrochimica Acta* **2016**, 187: p. 55-64.
19. H. Wang, D. Ren, Z. Zhu, P. Saha, H. Jiang, and C. Li, *Chemical Engineering Journal* **2016**, 288: p. 179-184.
20. R.V. Bugga, S.C. Jones, J. Pasalic, C.S. Seu, J.-P. Jones, and L. Torres, *Journal of The Electrochemical Society* **2016**, 164(2): p. A265-A276.
21. B. Campbell, J. Bell, H.H. Bay, Z. Favors, R. Ionescu, C.S. Ozkan, and M. Ozkan, *Nanoscale* **2015**, 7(16): p. 7051-5.
22. Z. Gong, Q. Wu, F. Wang, X. Li, X. Fan, H. Yang, and Z. Luo, *RSC Advances* **2015**, 5(117): p. 96862-96869.
23. A. Eftekhari, L. Li, and Y. Yang, *Journal of Power Sources* **2017**, 347: p. 86-107.
24. Z.A. Ghazi, L. Zhu, H. Wang, A. Naeem, A.M. Khattak, B. Liang, N.A. Khan, Z. Wei, L. Li, and Z. Tang, *Advanced Energy Materials* **2016**, 6(24).
25. H. Park and D.J. Siegel, *Chemistry of Materials* **2017**, 29(11): p. 4932-4939.
26. D.A. Boyd, *Angew Chem Int Ed Engl* **2016**, 55(50): p. 15486-15502.

27. W.J. Chung, J.J. Griebel, E.T. Kim, H. Yoon, A.G. Simmonds, H.J. Ji, P.T. Dirlam, R.S. Glass, J.J. Wie, N.A. Nguyen, B.W. Guralnick, J. Park, A. Somogyi, P. Theato, M.E. Mackay, Y.E. Sung, K. Char, and J. Pyun, *Nat Chem* **2013**, 5(6): p. 518-24.
28. A. Eftekhari, *Sustainable Energy & Fuels* **2017**, 1(1): p. 14-29.
29. A. Abouimrane, D. Dambournet, K.W. Chapman, P.J. Chupas, W. Weng, and K. Amine, *J Am Chem Soc* **2012**, 134(10): p. 4505-8.
30. H. Wu, D. Zhuo, D. Kong, and Y. Cui, *Nat Commun* **2014**, 5: p. 5193.
31. M.H. Ryou, Y.M. Lee, J.K. Park, and J.W. Choi, *Adv Mater* **2011**, 23(27): p. 3066-70.
32. M.-H. Ryou, D.J. Lee, J.-N. Lee, Y.M. Lee, J.-K. Park, and J.W. Choi, *Advanced Energy Materials* **2012**, 2(6): p. 645-650.
33. W. Weng, V.G. Pol, and K. Amine, *Adv Mater* **2013**, 25(11): p. 1608-15.
34. A.D. Dysart, J.C. Burgos, A. Mistry, C.-F. Chen, Z. Liu, C.N. Hong, P.B. Balbuena, P.P. Mukherjee, and V.G. Pol, *Journal of The Electrochemical Society* **2016**, 163(5): p. A730-A741.
35. Q. Zhao, X. Liu, J. Zheng, Y. Deng, A. Warren, Q. Zhang, and L. Archer, *Proc Natl Acad Sci U S A* **2020**, 117(42): p. 26053-26060.
36. M. Weiss, R. Ruess, J. Kasnatscheew, Y. Levartovsky, N.R. Levy, P. Minnmann, L. Stolz, T. Waldmann, M. Wohlfahrt-Mehrens, D. Aurbach, M. Winter, Y. Ein-Eli, and J. Janek, *Advanced Energy Materials* **2021**.
37. Z. Zhang, Z. Zhang, J. Li, and Y. Lai, *Journal of Solid State Electrochemistry* **2015**, 19(6): p. 1709-1715.
38. A. Gupta, A. Bhargav, J.P. Jones, R.V. Bugga, and A. Manthiram, *Chem Mater* **2020**, 32(5): p. 2070-2077.

6. BATTERY THERMAL SENSING: IN SITU THERMAL RUNAWAY DETECTION WITH AN INTEGRATED INTERNAL SENSOR

A version of this chapter has been previously published as journal articles: Mihit H. Parekh, Bing Li, Manikandan Palanisamy, Thomas E. Adams, Vikas Tomar, and Vilas G. Pol. *In Situ Mechanistic Elucidation of Superior Si-C-Graphite Li-Ion Battery Anode Formation with Thermal Safety Aspects*. ACS Appl. Energy Mater. 2020, 3, 8, 7997-8008; It is reproduced here with permission from the ACS Publications. The main journal articles and supporting information have been merged, and the text and figures have been modified where appropriate. Electrochemical testing, thermal safety tests, and characterization were carried out by Mihit H. Parekh. Sensor embedment in the spacer, resistance temperature detector data analysis, and modeling were carried by Dr. Bing Li and Dr. Vikas Tomar. Dr. Thomas E. Adams provided his technical expertise to the project. Manuscript preparation was performed by Mihit H. Parekh and Dr. Bing Li.

ACS Appl. Energy Mater. DOI: 10.1021/acsaem.0c01392

6.1 Overview

Thermal safety is of prime importance for any energy storage system. For Lithium-ion Batteries (LIBs), numerous safety incidences have been roadblocks on the path towards realizing high energy density next-generation batteries. Solutions viz., electrolyte additives, shut-off separators, exotic coatings have limited scope in their operating voltage window, response time, and performance. Various temperature monitoring devices have been tested out with their limitations. Here, we report the in situ sensing of thermal signatures from the anode of a typical LIB using an internal resistance temperature detector (RTD). Solid electrolyte interface (SEI) comprised of $ROCO_2Li$, $(CH_2OCO_2Li)_2$ and ROLi is formed on the surface of a graphite anode, and its decomposition releases enormous heat during thermal runway events. Sensing the temperature from the anode gives direct access to the heat liberated in thermal runaway, including SEI decomposition related heat generation. External short circuit (ESC) and overcharge tests were conducted to trigger the thermal runaway event, and temperature of 36.4 °C and 48.4 °C were recorded using internal RTDs, which were 9 °C and 20 °C higher than with external RTD, respectively. Interestingly, internal RTD has detection ability for 90% temperature rise 14 times faster than compared to the external RTD. Modeling of simulated tests explained the occurrence of different regimes during thermal runaway events initialed by ESC and overcharge. Furthermore, Multimode Calorimetry (MMC) for LIB with internal RTD yielded more endothermic peaks

beyond 150 °C due to the presence of 3D-printed Poly Lactic Acid (PLA) support. Overall, 1.75 kJ g^{-1} of generated heat was measured using MMC, which is significantly lower than LIB without RTD sensor. The RTD embedded assembly acts as a passive safety device while stationed inside the battery. Using thermal signatures from RTD, an advanced battery management system can lead to a conducive LIB, which would be a safer powerhouse for high energy density applications such as in the automotive industry and high energy grid-storage.

6.2 Introduction

One of the technologies that have positively affected the entire humankind, in a very short time since its advent, is Lithium-ion Batteries (LIBs). The 2019 Nobel Prize in Chemistry was given to Prof. John Goodenough, Prof. M. Stanley Whittingham, and Prof. Akira Yoshino for the development of this outstanding technology. In fact, LIBs have become the technology of choice to power our mobile and stationary applications.[1] After three decades of commercialization, the field has seen significant improvements in a variety of aspects, viz, charging rate, capacity, and cycle life. However, one key factor that remains of concern is the safety of LIBs.[2] The safety incidents are detrimental for the battery market and the businesses to a large extent. Though the frequency of LIB related safety incidents is one in million, it can still be improved to match the number of defects in semiconductor industries.[3]

The State of Health (SoH), State of Charge (SoC), and temperature profile are the major challenges to monitor and control LIBs. Ineffective monitoring and controlling can degrade battery life, performance, or worse cause mishaps like fires and explosions. To elucidate the causes and behavior of safety incidents, safety, and abuse tests are performed, which are classified into three categories: electrical, thermal, and mechanical.[4] A popular electrical abuse test is the external short circuit (ESC) test, where the positive and negative terminals of batteries are shorted. This creates a current pulse passing through the electrodes to initiate thermal runaway, which is based on the Joules' heating principle.[5] Another type of electrical abuse test involves overcharging or over-discharging the battery outside of its voltage stability window causes side reactions between the electrodes, current collectors, and electrolyte, leading to large amounts of localized heat generation in the system. In thermal abuse tests, the cells are exposed to high temperatures. The thermal stability of the battery can be understood through the evolution of battery temperature.

Mechanical tests abuse cells by crush, nail penetration, and even bullet impact give important details about the mechanical integrity of the system in larger battery configurations.[3, 6, 7]

Primary reasons for thermal runaway are directly related to the batteries' flammable organic electrolyte, cell design (electrode, separator, wall thickness, and vent), and charging-discharging rates. A variety of exothermic reactions contribute towards thermal runaway, namely, SEI decomposition, the interaction of lithium with electrolyte, and oxygen removal from the crystal lattice of the cathode during overcharge.[8] All these phenomena generate enormous heat inside the system, which is dissipated via conduction, convection, and radiation, and emission of molten cell material (ejecta). In events when external factors become dominant, viz, nail penetration, short-circuit, or external heating, the battery management system (BMS) cannot prevent the cell's catastrophic behavior. For such cases, safety devices are designed into cells, such as safety vents, special coatings, electrolyte additives, or shut-off separators.[9] However, *in situ* safety devices are known to adversely affect the performance of the cells. To mitigate a thermal runaway event, heat needs to be effectively dissipated away the cells or else temperature will continue to increase. Heat can be removed from the surface of the cell with water cooling, air cooling, phase change materials, heat sinks, or combinations of these approaches.[10-13] Internal cooling techniques like microchannels and small heat pipes have also been applied and are found to be more effective than external traditional approaches.[14-16] However, for internal cooling, the battery assembly needs to be significantly modified, which leads to a reduction in energy density. It is critical to understand the thermal gradient of a cell as the surface temperature monitored is a fraction of the internal maximum temperature of cells thus creating a need to precisely monitor the internal temperature to provide information to improvise safety, performance, and SoH. Because the temperature at the cell's core is typically higher than the external surface, making *in situ* temperature measurement is vital for monitoring and controlling.

Various temperature measurement techniques have been introduced to assist BMSs for better prediction and prevention, viz, Thermocouples, Thermistors, Impedance-based temperature measurements, Fiber Bragg-grating (FBG) sensors, Thermal imaging-liquid crystal thermography, and RTDs.[1] Mutyala *et al.* integrated thin flexible K-thermocouple inside cells for measuring internal temperature.[17] Similarly, Martiny *et al.* developed a thermocouple matrix to measure internal spatial temperature.[18] Zhang *et al.* inserted a T-type thermocouple between the separator and anode.[19] Though results from thermocouple monitoring are promising, they cause stability

issues, require isolation from the electrolyte, and need special arrangements like drilling holes to insert them inside the batteries. Hybrid electric vehicles. viz, Honda Civic and Toyota Prius use thermistors to measure battery temperature.[20] Researchers like Debert have developed and utilized thermistors for comparison to simulations, but overall, their application in research has been very limited.[21] Currently, thermistors can only be placed on the terminals, surface, or near the cell. Impedance based measurement is a non-destructive and sensor-less measurement and studied by various researchers and their colleagues, viz., Raijmakers, Srinivasan, and Schwartz have shown some development of this technique.[22-24] However, this technique faces key issues from interference with electric current, aging and SoC dependencies, cross talk interference, and large charge/ discharge (DC) currents. Guiliano *et al.* observed temperature fluctuations for pouch cells with the help of liquid crystal thermography.[25] Kakade *et al.* calibrated an extended set of thermochromic liquid crystal (TLC) and provided a relationship between hue and temperature.[26] This technique is quite cost-intensive, impractical, and fragile. Yang *et al.* pioneers in FBG sensor technology for LIBs, installed it to extract information about the temperature.[27] Amietszajew *et al.* utilized it for measuring temperature for 18650 battery.[28] Novais *et al.* used an FBG sensor between double layer separator.[29] For FBG sensors, the measurement is dependent on fiber coating and presently, there is no development for calibration and measurement below 0°C.[28],[20] This points towards the importance of effective temperature management system (TMS) designs, which should be compact, low-cost, light-weight, reliable, and capable of swift-detections. Wang *et al.* utilized an RTD between two electrodes to sense the temperature gradient.[30] Lee *et al.* developed thin flexible films for internal temperature measurements.[31] Table D.1 provides a comparison of existing temperature monitoring techniques with their advantages and disadvantages.

In our previous work, an RTD was embedded in a 3D-printed polylactic acid (PLA) spacer and stationed behind the cathode[32] for *in situ* thermal monitoring of ESC events. It was observed that the temperature gradient between internal RTD and external RTD was 5.8°C and internal RTD responded almost 10 times faster. This also proved that ceramic RTD was stable in the harsh chemical and electrochemical environment inside the cell. Graphite anode has the SEI layer, which consists of reduced electrolytic compounds, viz, LiF, Li_2O, Li_2CO_3, polyolefins, and semibicarbonates, formed on its surface,[33] and during the charged state, the graphitic anode has lithium in its interlayer spacing. The initiation of the thermal runaway begins with the breakdown

of SEI followed by the electrolyte reacting with lithium in graphite interlayers. This makes it critical to monitor temperature changes with an RTD stationed behind anode to mitigate thermal runaway situations using the battery management system.

In this article, three such thermal runway events were studied, viz, ESC, overcharge, and overheat using multiple module calorimetry (MMC) to determine the detection capabilities and presence of RTD on the operation of cells. These tests are very important steps towards the development of *in situ* temperature monitoring systems for next-generation LIBs. Through a combination of these tests – a complete portrait of RTD behavior, safety aspects, advantages, and drawbacks are obtained.

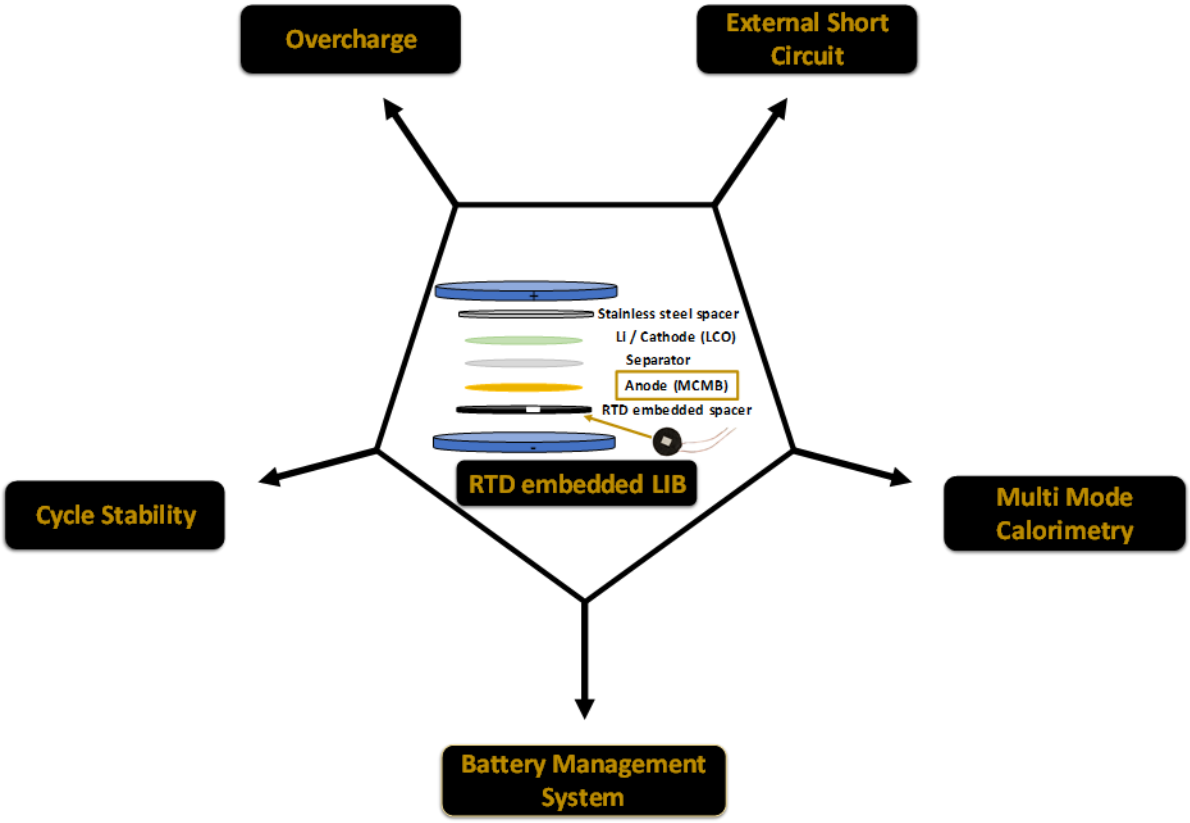

Figure 6.1: *In situ* RTD sensor for monitoring electrode surface temperature during simulated thermal runaway abuse tests like overcharge, ESC, overheating. The thermal signatures from RTD act valuable input for the battery management system.

6.3 Experimental Section

6.3.1 Electrode Development and Characterization

Lithium cobalt oxide (LCO) and mesocarbon microbeads (MCMB) electrodes were prepared using 80% active component (LCO or MCMB), 10% HSV-1800 binder and 10% Super P carbon black in N-methyl pyrrolidone (NMP) solvent. Components were mixed for 40 minutes using a Thinky mixer to form a homogeneous slurry. The slurry was cast on aluminum (for LCO) and copper (for MCMB) current collectors using the automatic doctor blade technique. After casting, the laminate was dried in a vacuum oven (MTI Corporation) at 80^{o}C for 12 hours. Following this, the dried laminate was calendared using roll press and then punched to obtain electrode discs. Electrodes of different loadings were prepared to perform the tests. MCMB electrodes had loading for thin electrodes of 2 mg cm^{-2} and thick ones had 20 mg cm^{-2}. In the case of LCO, thin electrodes had a loading of 5 mg cm^{-2} and thicker one had 42 mg cm^{-2}. Electrodes of diameter 15.5 mm were dried in an oven before utilizing them for fabricating CR2032 coin cells (MTI Corporation). Cells were assembled in inert argon (99.998%) atmosphere using glovebox with O_2 and H_2O concentration <1 ppm. Key components of the cell include electrodes, Celgard 2500 separator, and electrolyte, which consisted of 5% (v/v) fluoroethylene carbonate in 1 M $LiPF_6$ dissolved in 1:1 EC:DEC solution. Half cells were cycled between 0.01 – 1.5 V and given two formation cycles at 0.1C rate followed by one at 0.25C rate. Full cell with LCO and MCMB electrodes were given two formation cycles (between 3.0 – 4.2 V) before conducting overcharge and calorimetric experiments. Cyclic voltammetry was performed at a scan rate of 0.1 mV s^{-1} between 0.01 – 1.5 V using Gamry-600+ reference system. Electrochemical impedance spectroscopy (EIS) was obtained using Gamry-600+ reference system after the 50th, 100th, 150th and 200th cycle. EIS was conducted using 10 mV amplitude AC voltage perturbation over frequency ranging from 1 MHz – 0.01 Hz. Overheating tests were conducted using Multiple Module Calorimetry (Netzsch Instruments North America) from room temperature up to 300°C. Overcharge tests were conducted by charging the cell at 5C rate from 4.2 V – 12.0 V on Gamry-600 Reference System. ESC tests were conducted by directly connecting the positive and negative poles of the coin cell through a shunt resistor < 20 mΩ resulting in a “hard short circuit” condition defined in NAVSEA 9310 [34]. During abuse tests, the coin cell was clamped within a polylactic acid (PLA) cell holder prepared by additive manufacturing, where an RTD was embedded for

measuring cell-surface temperature. Details of the short circuit testing setup can be found in our previous work.[32] All the potentials stated are versus Li^+/Li.

6.3.2 Material Characterization

Particles before and after destructive tests were imaged using Nova Nano SEM 200 microscope. Raman imaging was carried out with a 785 nm Raman probe by CNI Laser, and the analyzed region was imaged with Dino-Lite digital microscope. Using Rigaku SmartLab X-Ray Diffractometer having Cu Kα source of radiation, x-ray diffraction (XRD) patterns were recorded for MCMB and LCO powders at a scan rate of 0.5° min^{-1} (Figure D.3). Calorimetry experiments were conducted on Multiple Module Calorimetry MMC 274 Nexus® from room temperature up to 300℃.

6.3.3 Device Configuration

The role of the internal RTD sensor is to ensure that temperature measurement is effective, accurate, and does not interfere with the operation or damage the electrode surface. Therefore, the RTD sensor was placed behind the anode's copper current collector. RTD sensor was embedded in a 3D-printed spacer composed of polylactic acid (PLA) by additive manufacturing. For this work, a Pt1000 RTD (Omega Engineering Inc.) having a 4 mm × 5 mm flat Al_2O_3 sensing surface was chosen. Pt1000 RTD has been widely employed in temperature monitoring of processes. The RTD embedded in the PLA spacer was ensured to be completely flat to achieve better contacts between electrodes and separators and to avoid internal short circuit issues during crimping. As shown in Fig. 6.1, a strip of copper was wound around the PLA spacer to ensure electronic conductivity to the anode. The spacer with copper strip was placed in the negative cap and anode was placed at the center followed by electrolyte, separator, LCO cathode, stainless steel spacer, and spring. The assembly was then closed using a positive cap and crimped to ensure tight contact between components. This novel method of sensing the thermal change in the electrode was achieved, which mitigated sensor-related disturbance in the battery operation.

6.4 Results & Discussions

Figure 6.1 illustrates a schematic of the RTD integrated LIB whose thermal signature can be input to an advanced BMS to mitigate accidents and damage in the event of thermal runaway. The performance of internal RTD sensors by far exceeds that of external temperature sensors, in abuse tests like an ESC and overcharge. Also, the presence of an internal RTD acts as a passive safety device inside LIB by absorbing a portion of the heat generated during severe thermal runaway and melts. To quantify and validate the presence of the novel thermal measurement device, the RTD, inside the battery, electrochemical studies were performed in conjunction with the electrical and thermal abuse tests. These tests attempt to mimic the normal operation of a battery and abuse scenarios, which may be encountered by the LIBs while in service. The response of the LIBs in each of these abuse tests was also analyzed. These studies can help elucidate the relationship between the battery's thermal response and its chemistry. From the test conditions, insights about the thermal runaway processes and how abuse conditions trigger thermal runaway in LIBs were enhanced.

6.4.1 Electrochemical Measurements

Electrochemical Impedance Spectroscopy (EIS) analysis was conducted between 1 MHz to 10 mHz at 25 °C for half-cell. In Fig. 6.2A, Nyquist plots of lithium cell impedance are shown with Warburg element having an angle higher than 45°, which implies a high lithium-ion diffusion phenomenon.[35] To obtain a clear understanding of the system, the lithium battery was completely charged (fully delithiated anode) before taking the EIS. EIS was performed on 50^{th}, 100^{th}, 150^{th} and 200^{th} cycles. After the 50^{th} cycle, series resistance (R_s) was 3Ω, which increased to 11Ω in the 100^{th} cycle. The increase in impedance could be attributed to conductivity loss due to current collector corrosion, particle delamination, or decomposition of binder particles, creating additional impedance in the system.[36] Series resistance (R_s), however, remained constant even after 150 charge-discharge cycles. Interestingly, after the 200^{th} cycle, R_s reduced to 5Ω, which could be due to extended charge-discharge cycling creating synergy between all battery components and higher electrolyte penetration.[37] After 50 cycles, charge transfer resistance (R_{CT}) was about 32Ω, which slightly increased to 36Ω for the 100^{th} and 150^{th} cycles too. For the 200^{th} cycle, R_{CT} was further increased to 38Ω. This overall increase in the R_{CT} may have arisen from stress accumulation in the

electrodes from continuous long-term cycling.[36] From Ohmic resistance (R_O), it is clear that the effect of the 3D-printed spacer on the cell operation and performance is insignificant and could be safely used to manage LIBs.

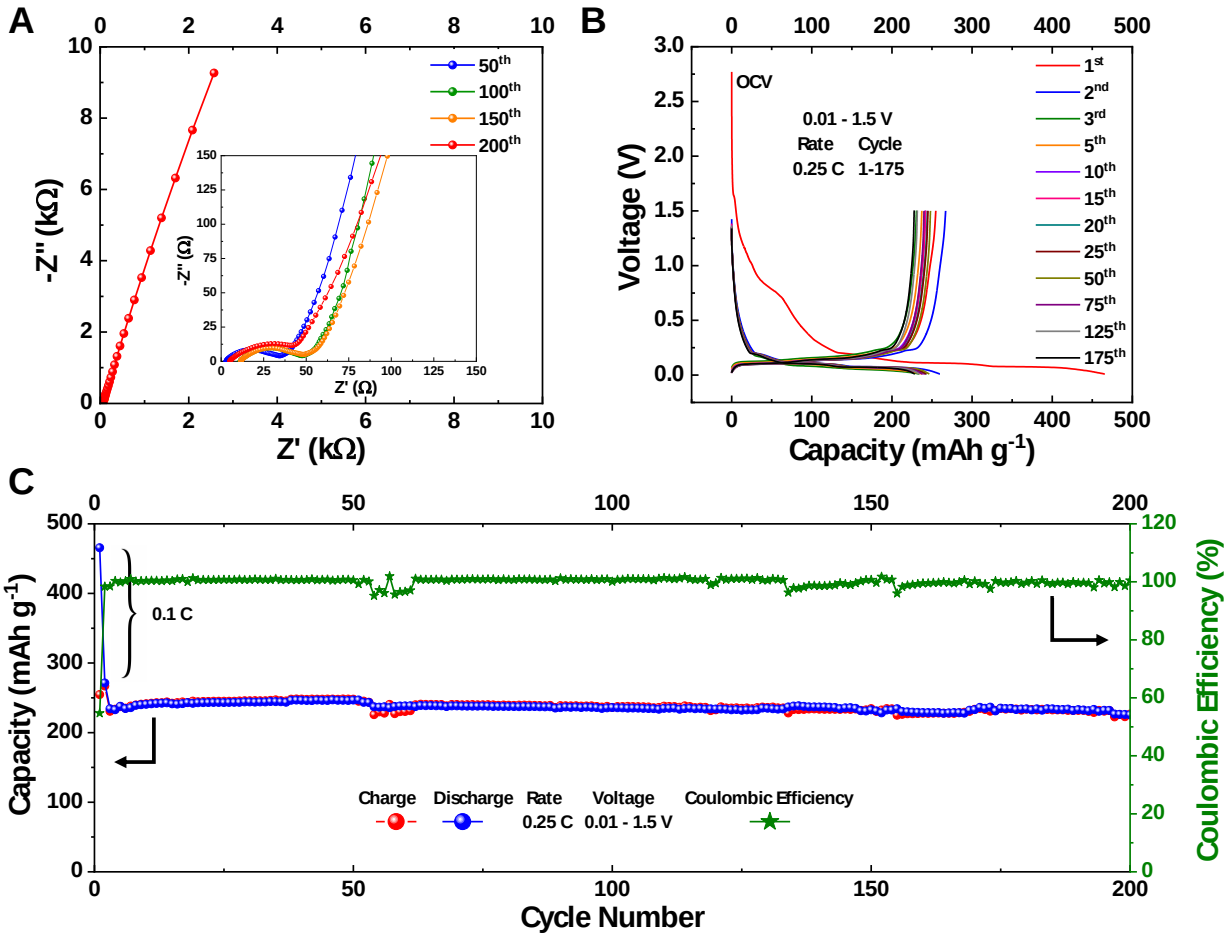

Figure 6.2: Electrochemical performance of MCMB half-cell. A: Electrochemical Impedance Spectroscopy; B: Voltage profiles for cycle 1-175; and C: Constant current density cycling at 0.25 C rate

Cyclic Voltammetry was performed between 0.01 V and 2.0 V (versus Li/Li^+ reference electrode) at a scanning rate of 0.1 mV s^{-1} to determine kinetics and reversibility of the reaction for RTD embedded half–cell. Lithiation of MCMB occurs when the potential is swept from 2.0 V to 0.01 V and delithiation of MCMB occurs when sweeping from the potential of 0.01 V to 2.0 V. Typically, MCMB has one reduction peak and one oxidation peak between 0.01 V and 0.5 V. We observed oxidation peak around 0.21 V (Figure D.1). For the first cycle, during reduction, two peaks were obtained at 1.61 V and 0.88 V. The peak at 0.88 V was due to SEI layer formation.[38]

Figure 6.2B shows voltage profiles for RTD embedded cell. From the plot, it can be seen that MCMB is lithiated at 0.11 V and delithiation begins at 0.18 V for 0.25 C rate. This lithiation profile is fairly congruent to that obtained in the literature.[39] This supports the fact that the addition of RTD on PLA spacer is not affecting the cycling performance of the batteries.

Now, from Fig. 6.2C, it was observed that the first cycle discharge specific capacity for RTD embedded MCMB cell was 465 mAh g^{-1}, and the charge specific capacity was 254 mAh g^{-1}. This irreversible capacity loss is attributed to the formation of the SEI layer.[38] For the 0.25C rate cycling, the performance of the RTD embedded system was very similar to conventional MCMB cells. The RTD embedded cell gave a very stable average capacity of 238 mAh g^{-1} after 200 cycles. There are some disturbances around the 50^{th} and 150^{th} cycles due to the removal of the cell from the Arbin cycler to conduct the EIS analysis. This may be the possible reason for the fluctuations in the cycles around those points. Interestingly, despite a few fluctuations, the cell continued to cycle like a conventional cell and gave a very stable cycle performance.

6.4.2 External Short-Circuit (ESC) Test

Connecting a short between the electrodes at different potential externally generates a high current pulse in the LIB system. Major factors contributing to ESC are physical damage, water infiltration, and contaminating cells with conductors[1] Also, ESC causes damage to the electrode morphology due to the forceful removal of lithium-ion from the interlayer spacings (Figure D.4B). Pores and cracks generated on the surface of the MCMB electrode suggest sudden extraction of lithium ions from the morphology. The reaction mechanism, in the case of an external short circuit, is similar to that of overcharge (mentioned in the overcharge section) except for the disintegration of cathode material releasing oxygen on account of high voltage. The external short circuit leads to a high-temperature rise, which is responsible for the decomposition of electrolyte and other side reactions that may proceed along.

For the ESC test, LCO-MCMB full cell was used. The cell was charged at 0.1C rate to 4.2 V, then the terminals were shorted with a wire. The external circuit consisted of copper wires, 3D-printed cell holders with embedded RTD for battery surface temperature measurement, and a shunt resistor. The shunt resistor used was of 15 mΩ, generating a “hard short circuit” condition specified in NAVSEA 9310.[34] The current, voltage, internal RTD and external RTD resistances were measured and recorded for an hour using an Arbin data acquisition system and a temperature

recording unit by Omega Engineering The cells were at room temperature before the test. As soon as the terminals were shorted, reactions occurred almost instantaneously as indicated by the electrode's temperature monitored by the internal RTD. As shown in Fig. 6.3, the internal temperature rose by 12.4°C to a maximum of 36.4°C, but the external temperature only rose to a maximum of 27.6°C, and the maximum electrode temperature rise was 3.6°C. Remarkably, the detection ability of internal RTD to measure 90% of the temperature rise (t_{90}) turned out to be 14 times faster as compared to the external RTD. Previously, we reported the detection ability to be 10 times faster when the measurements were done from beneath the cathode surface.[32] This is a very critical and significant development suggesting the measurements to be observed from beneath the anode surface rather than cathode for even faster detection to avoid thermal runaway catastrophes.

Spotnitz *et al.* analyzed the mechanism of LIB short circuit and contributed the rapid heating mostly to ohmic heat generation and cathode decomposition,[40] which linked to the mass of the cathode material. Thus, for coin cells with limited amounts of electrode material and excessive electrolyte for Li^+ diffusion, the temperature rise caused by the short-circuiting can be predicted by the mass of active cathode material. In our previous work, the RTD sensor was placed behind the cathode aluminum current collector to measure cathode temperature during LIB short circuit. The previously reported relation between cathode temperature and active LCO mass[40] predicts a temperature rise of 9.12°C under the short-circuit condition, which is lower than the anode temperature rise observed in this study. Thus, the transient temperature difference between anode and cathode exists during a thermal runaway event caused by a short-circuit. As the thermal conductivity of polymeric separator is typically limited, the contact between the separator and porous electrode material generates high thermal resistance.[41] This suggests localized higher-heat generation from the surface of the anode as compared to that of the cathode.

In our previous work [32], a model relating the maximum rising rate of battery surface temperature ($\frac{dT_{ext}}{dt}_{,max}$) with LCO mass, and cathode temperature rise (ΔT_c) was developed.[40] Here the model was modified to provide a prediction of ΔT_c based on LCO mass and $\frac{dT_{ext}}{dt}_{,max}$, which is shown in Fig. 6.3B. It can be found that if ΔT_c and ΔT_a were assumed to be the same in a thermal runaway event, such as ESC, the LCO mass and $\frac{dT_{ext}}{dt}_{,max}$ based prediction of ΔT_c underestimated temperature rise of anode ΔT_a. The error in the predicted anode temperature rise

mainly comes from two aspects:(1) the difference between anode temperature and cathode temperature due to the breakdown of various compounds in the SEI layer and reaction of lithium stored in the interlayer spacing of MCMB with electrolyte generates extra heat on the anode side, and (2) thermal resistance within the tested LIB. $\frac{dT_{ext}}{dt}_{,max}$ observed in this study was lower than most LIBs tested in our previous work despite the high LCO mass. The value of ΔT_a capture by internal RTD generally matched with the LCO mass, further verified that the tested LIB was with high thermal resistance which affected $\frac{dT_{ext}}{dt}_{,max}$. The difference in cell structure from the assembly process could affect battery surface temperature and impair the reliability of $\frac{dT_{ext}}{dt}_{,max}$ based on LIB thermal runaway monitoring. This low $\frac{dT_{ext}}{dt}_{,max}$ generated high error in prediction of electrode temperature rise shown in Fig. 6.3B. Thus, the electrode temperature measured by internal RTD is more effective for battery safety management and thermal runaway detection. Battery surface temperature cannot monitor the transient change in electrode temperature as in thermal runaway events.

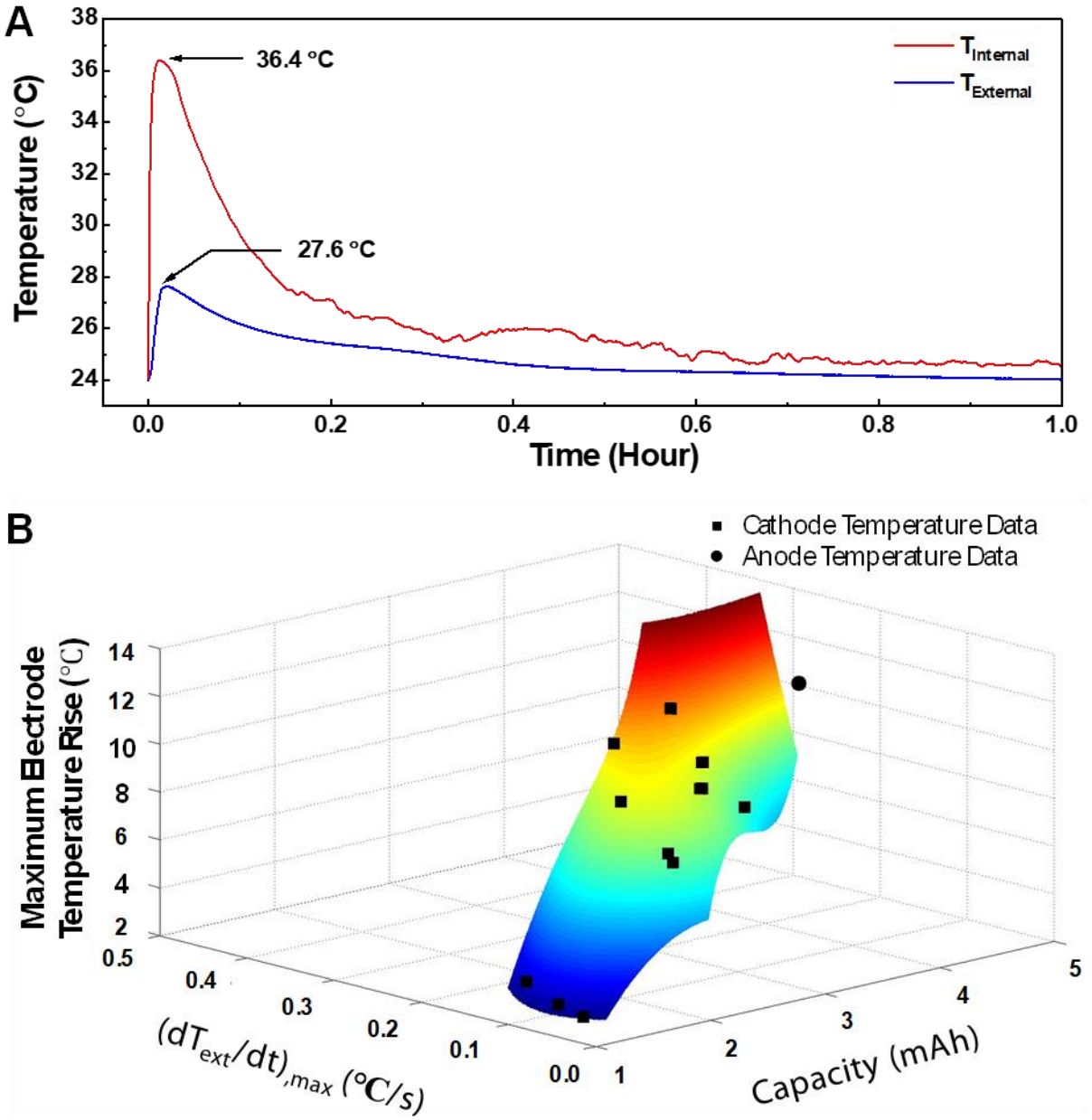

Figure 6.3: Short Circuit Test Result and Prediction A: Temperature measurements with internal RTD, and external RTD during the short circuit test of coin cell comprising MCMB anode, LCO cathode with 1M $LiPF_6$ in EC/DEC electrolyte; B: Prediction of anode temperature rise in ESC based on cathode temperature measurement and comparison with measured anode temperature rise.

6.4.3 Micro-Raman Analysis

The graphite anode was studied by micro-Raman analysis at pre and post ESC test. Based on the work of Pimenta *et al*.,[42] D, G, and G' bands of graphite originate from material defects and are expected to exhibit Raman peaks around 1350 cm^{-1}, 1580 $cm^{-1,}$ and 2700 cm^{-1} respectively. For graphite material, these Raman peaks have three main origins: stacking faults, crystallite size, and localized electronic states.[42] The stacking fault can be evaluated by examining the existence of G' band.[42] Localized electronic states are associated with the in-plane crystallite size L_a, which is related to the intensity ratio of D and G bands (I_D/I_G) with the relation given in eq. (1):[42]

$$L_a\,(nm) = (560/E^4).(I_D/I_G)^{-1} \qquad (6.1)$$

where E is the excitation laser energy in eV. During the continuous cycling of LIBs, the lithiation- delithiation process can induce dislocations within the graphite[43] and cracking of graphite particles.[44] This would change the in-plane crystallite size L_a, which can be reflected by the I_D/I_G ratio. The G band is generally present throughout the graphite structure, and its intensity represents the lithiation condition of the anode.[43, 44] During the lithiation process, the intensity of the G band of graphite would decrease, and the G band would be nearly non-detectable when the anode is fully charged.[45] In this study, several features in the micro-Raman spectrum, including position and intensity of G band, the existence of G' band, and intensity ratio I_D/I_G were analyzed to obtain a detailed understanding of changes in the graphite structure from short circuit test. The micro-Raman analysis results are presented in Fig. 6.4.

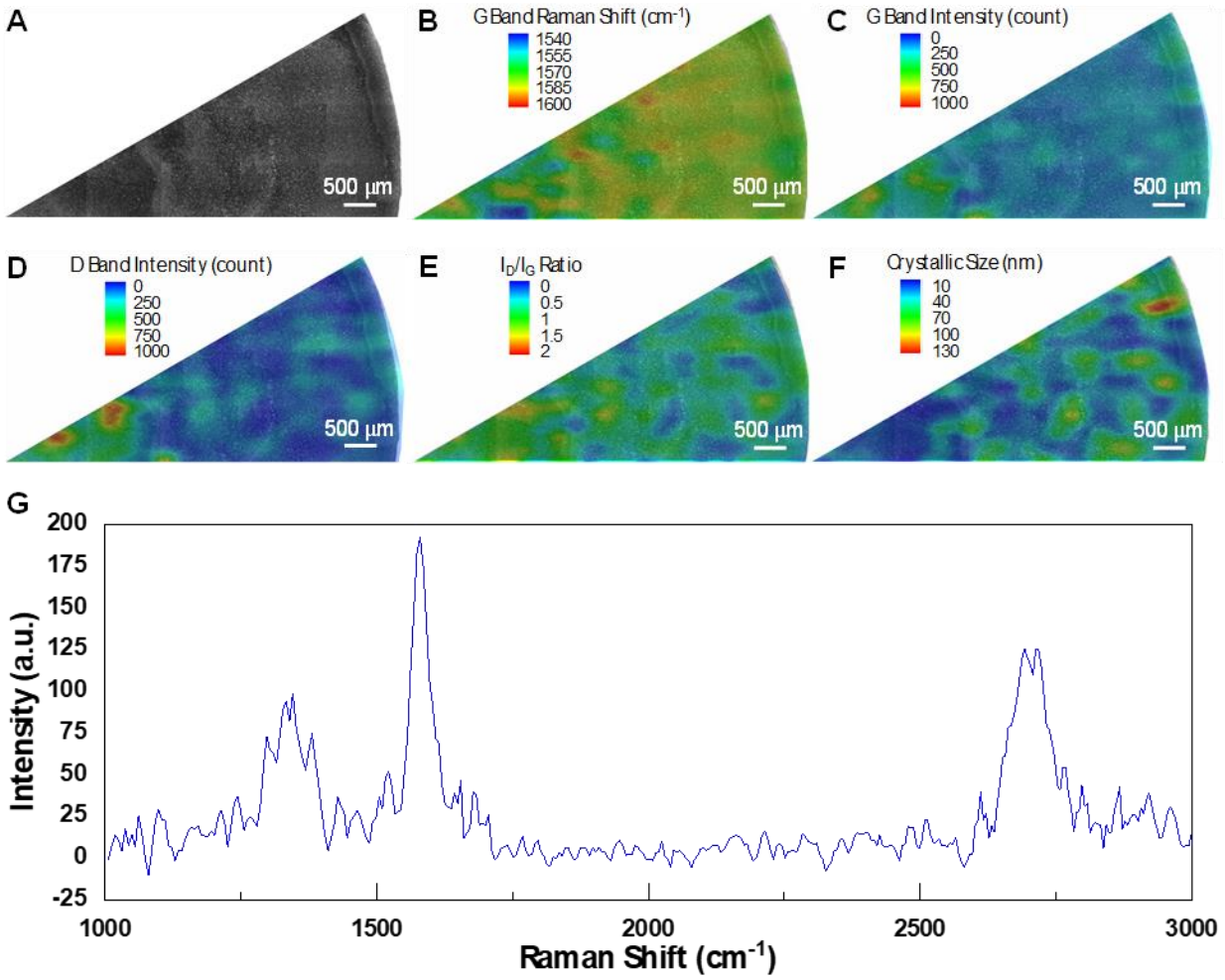

Figure 6.4: Micro-Raman spectroscopy analysis of MCMB anode after short circuit test A: Microscope imaging of anode; B: Raman shift contour of G band; C: G band intensity contour; D: Raman shift contour of D band; E: Contour of intensity ratio I_D/I_G; F: Crystalline size contour based on I_D/I_G; G: Representative Raman Spectrum of MCMB after short circuit test.

Based on the Raman spectra obtained from the analyzed region of the graphite anode, G' band presented throughout the anode. The double-peak feature of the G' band was maintained after the short circuit test, which originates from the high-temperature treatment of graphite that is common in anode preparation.[42] This indicates that the graphite generally maintained its layered structure and crystallite features formed during the high-temperature treatment. The existence of the G' band enabled the study of the anode after the short circuit test based on information obtained from the micro-Raman analysis of graphite. From the analysis of the G band, the graphite-lithium intercalation compound (LiC_6) formed during the charging of the LIB was exhausted during the short circuit test, as changes in the intensity and position of the G band were negligible compared

with a pristine graphite anode. The shape of the G band after the short circuit test remained similar to that of the pristine MCMB electrode with no short circuit history reported in the literature,[46] although the splitting of G band has been noticed during the lithiation process of MCMB and graphite electrodes.[47] The splitting of G-band of MCMB could be contributed to the phase transition to the stage 4 phase, where both the vibration of carbon atoms in interior graphite layer planes and inbounding graphite layers existed.[47, 48] During the delithiation process, the splitting of G-band was erased by the reverse phase transition, which was observed by Chen et al. in their in-situ Raman analysis of MCMB electrode delithiation.[47] The unchanged G band shape of MCMB electrode after the short circuit test indicated that most of the lithium ions on the anode side were involved in the delithiation process during the short-circuit condition. Thus, the temperature rises from the short-circuit test can be predicted with the mass of electrode material or LIB capacity. It can then be compared with the temperature rise from regular LIB discharging to evaluate the effect of short circuit related thermal runaway on LIB safety.

The in-plane crystallite size L_a was obtained from the I_D/I_G ratio and is presented in Fig. 6.4. From comparison with the crystallite size obtained in the same manner from pristine graphite anode, there was evident cracking in the graphite after a short circuit. SEM imaging of the anode after the short circuit test also supported this (Figure D.4B). Thus, it is necessary to measure the electrode temperature in thermal runaway events from the current collector side rather than directly from the anode material, as electrode cracking may impair the sensor-electrode contact.[32]

6.4.4 Overcharge Test

Overcharging essentially stores excess energy into the cell, which is followed by heat generation and gas evolution. The thermal runaway induced by overcharge is typically more severe than any other abuse condition due to the excessive energy stored in the system. Overcharging is typically caused by the failure of BMS to stop the charge at the cut-off voltage threshold. This can also occur in a series connection of cells of varying capacities where the cell with the least capacity gets overcharged. In this case, the BMS usually controls the virtual cell, which is a string of cells connected in series. Depending on the SoC, there is either capacity fade or thermal runaway situation. During overcharging, excessive Li^+ ions from cathode intercalate into the graphitic anode, and once the anode is saturated with the Li^+ ions, the excess lithium plates on the surface of the graphitic anode, forming dendrites.[49]

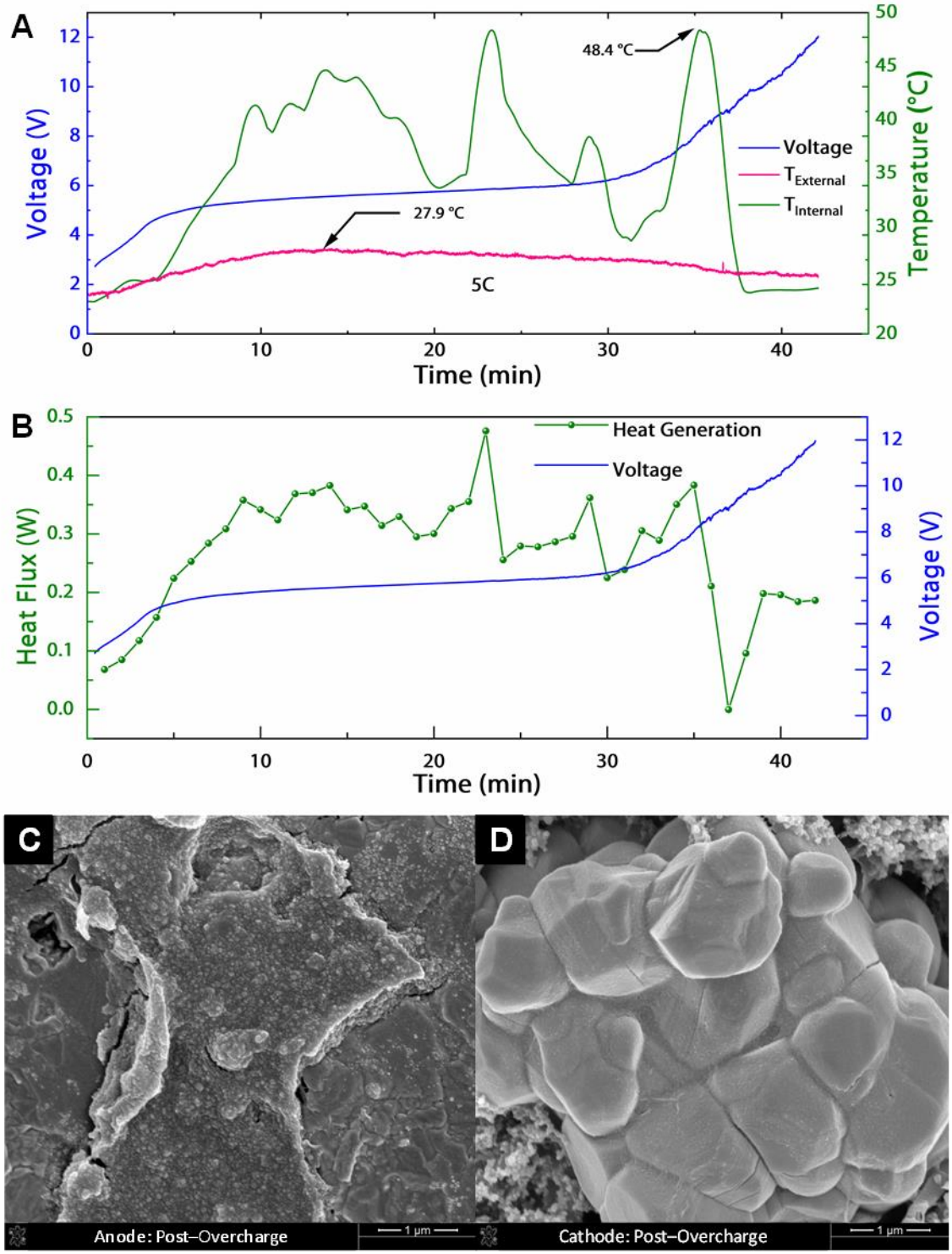

Figure 6.5: Overcharge Abuse Test A: In Operando overcharge abuse test of LCO-MCMB Full Cell at 5C rate with thermal sensing using RTD; B: Heat generation rate during the overcharge process; C: High-resolution SEM of Anode post overcharge test; and D: Cathode post overcharge test.

If lithium is extracted beyond a lower threshold, typically x = 0.16 for Li_xCoO_2, from the crystal lattice of the cathode, then it can cause structural collapse, liberating heat and oxygen from decomposition.[50] For lithium cobalt oxide, at overcharged conditions, it forms highly oxidative cobalt oxide (CoO_2), which reduces itself by oxidizing the electrolyte causing more gas formation. For larger format cells under high current, the cell explodes and at smaller current, the cell swells.

For the overcharge test, LCO-MCMB Full Cell was cycled at 0.1C rate between 3.0 V – 4.2 V for 5 cycles to complete SEI formation. Next, the cell was charged at the 5C rate with voltage upper threshold at 12 V. The cells were at room temperature before the test. The maximum temperature recorded by external RTD was 27.9°C, while the maximum internal RTD detected a much higher temperature of 48.4°C during the overcharge process. This is one of the highest recorded temperatures from a coin cell configuration with electrochemically low active mass, which also shown the existence of high thermal resistance between the electrode and case of the coin cell. From the internal RTD, the large temperature variations measured are likely due to the gas evolution from cathode and electrolyte decomposition, which causes the electrode to move inside the coin cell. Major reactions during overcharge, which occur at the cathode and electrolyte decomposition are shown in the equations (2) – (6) below:[8, 51]

$$\mathbf{Li_{0.5}CoO_2} \rightarrow \frac{\mathbf{1}}{\mathbf{2}}\mathbf{LiCoO_2} + \frac{\mathbf{1}}{\mathbf{6}}\mathbf{Co_3O_4} + \frac{\mathbf{1}}{\mathbf{6}}\mathbf{0_2}\uparrow \tag{6.2}$$

$$\mathbf{3\ CoO_2 \rightarrow Co_3O_4 + O_2}\uparrow \tag{6.3}$$

$$\mathbf{C_3H_4O_3} + \frac{\mathbf{5}}{\mathbf{2}}\ \mathbf{O_2 \rightarrow 3\ CO_2 + 2\ H_2O} \tag{6.4}$$

$$\mathbf{C_3H_4O_3 \rightarrow CO_2 + C_2H_4O} \tag{6.5}$$

$$\mathbf{(CH_3CH_2O)_2CO + 6\ O_2 \rightarrow 5\ CO_2 + 5\ H_2O} \tag{6.6}$$

The readings of internal and external RTDs begins to differ around 4.7 V, which is typically the decomposition voltage for the electrolyte.[52] After the 37th minute, the internal RTD temperature dropped, which may be caused by the electrode losing contact with the RTD due to gas generation. When lithium is completely extracted from the LCO, the chemical reaction stops on the cathode side, and then the heat generation from hereon is primarily due to overpotential from ohmic heating at a relatively lower rate.[50] Also, the material of construction for coin cells is stainless steel, which has a high heat transfer coefficient and hence, dissipates heat quickly by

convection. To measure the exothermic heat generated from all the cell's components, MMC studies were carried out. As shown in Fig. 6.5C-D, post-diagnostic analysis of electrodes with high-resolution SEM was performed after the overcharge test. Anode seems swollen due to over lithiation and as for cathode, the morphology has become rough and slight cracks can be seen on the surface due to complete lithium extraction from the crystal lattice. High-resolution SEM of pristine anode and cathode are shown in Fig. D.4A and Fig. D.5, respectively.

Multiple works have been reported on modeling the heat generation during the overcharge of LIBs.[50, 53, 54] In these works, the surface temperature was used to represent the temperature of the battery, or the temperature field within the LIBs was assumed to be uniform. To validate the assumption of uniform temperature distribution with LIBs, the Biot number, a dimensionless quantity, is typically employed.[50, 55] The Biot number is defined as:

$$\mathbf{B_i} = \frac{\mathbf{h} \cdot (\mathbf{V/A})}{\mathbf{k}} \tag{6.7}$$

for a cylinder, h is the heat transfer coefficient between the LIB and air, V is the volume of the LIB, A is the surface area of the LIB, and k is the thermal conductivity.[50] An estimation of k was obtained as 0.5 – 1.1 W/(m.K)[56], and h is estimated as 10 W/(m.K). With this information, the Biot number for the LIB can be estimated at 0.011 – 0.024. It has been widely accepted that when $B_i \leq 0.1$, the temperature of a system can be regarded as uniform.[57] However, both this study and our previous work[32] indicated that a significant temperature gradient would be present during thermal runaway and appears to be attributed to gas generation during thermal runaway as it has been reported that gas accumulation could result in the deformation of battery construction,[58] which affects the condition of thermal conduction. As a result, it is necessary to measure electrode temperature to obtain the heat generation rate during LIB thermal runaway.

A general energy balance equation for LIBs[28] can be written as:

$$\mathbf{mC}\frac{\mathbf{dT_{ext}}}{\mathbf{dt}} = \dot{\mathbf{Q}} - \mathbf{hA}(\mathbf{T_{ext}} - \mathbf{T}_\infty) \tag{6.8}$$

where m is battery mass, C is the average heat capacity of LIB, $\dot{Q}$ is the rate of heat generation, T_{ext} is battery surface temperature, T_∞ is environment temperature and A is surface

area of LIB. Despite the validity of equation (8), the cell temperature was assumed uniform that contradicts the observation in Fig. 6.5.

A modification of equation (8) is proposed here to improve the rate of heat generation estimate during overcharge. The cell was clamped in a PLA battery holder during the test, and LIB's heat loss solely came by thermal conduction through the PLA holder. Since the LIB surface temperature was relatively low, the temperature of the external surface of the PLA holder can be assumed to be 23 ℃ (room temperature during the test) and contact resistance between battery and PLA holder was neglected. The heat generation rate can then be expressed by eq. (9) as:

$$\dot{\mathbf{Q}} = \mathbf{m}_{int}\mathbf{C}_{int}\frac{\mathbf{dT_{int}}}{\mathbf{dt}} + \mathbf{m}_{ext}\mathbf{C}_{ext}\frac{\mathbf{dT_{ext}}}{\mathbf{dt}} + \boldsymbol{\lambda}\mathbf{A}\frac{(\mathbf{T_{ext}} - \mathbf{T}_{\infty})}{\boldsymbol{\Delta}} \tag{6.9}$$

where λ is the heat conductivity of PLA and Δ is the thickness of the PLA holder. Here the LIB components were separated into two groups. The electrodes, separator, stainless steel, PLA spacer, and the RTD sensor were assumed to have the same temperature obtained by the internal RTD. Their total mass is m_{int} and the average heat capacity is C_{int}. The battery case, stainless steel spring, and electrolyte were assumed to be with the temperature obtained by the external RTD. Their total mass is m_{ext} and the average heat capacity is C_{ext}. C_{int} and C_{ext} were obtained with the heat capacity of individual LIB components[59-68] and $\dot{Q}$ was calculated for every 1-minute of temperature recording during the overcharge test.

From Fig. 6.5B, it can be found that the heat generation of LIB during thermal runaway can be separated into three periods: (1) $\dot{Q}$ increased gradually. The normal charging process of LIB was maintained in this period, most input energies were converted into chemical energy and stored in electrodes. (2) The heat was generated rapidly within LIB with some fluctuation in the heat generation rate. This period can be separated into two parts: when $0 < x \leq 0.16$ in Li_xCoO_2, most input energy was converted into heat. When x in Li_xCoO_2 reached 0, a rapid exothermic chemical reaction occurred [50]. (3) LIB shutdown denoted by $\dot{Q} \approx 0$ at t=37th minute, which corresponded with the sudden drop in electrode temperature. After electrode temperature started dropping, heat generation within the LIB was dominated by over potential related physical process and the contribution of the electrochemical process was negligible.[50]

6.4.5 Multiple Module Calorimetry Testing and Analysis

Temperature and cycling conditions are two of the many parameters that affect the performance of batteries. It is crucial for manufacturers to understand and know heat generation during the charging/discharging cycles for elucidating more about cell energy efficiency, lifetime, and to improve cell performance. Imperatively, to understand more about the coin cell safety characteristics, a cell must be subjected to cycling abuse or high temperature. Also, apart from the voltage and current measurements, a quantitative way to differentiate between changes in chemistry are needed for measuring heat signatures from the coin cell. A large amount of chemical and physical changes happens in a battery can be described with a function of time, temperature, and cycling load. Heat absorbed or released during these physicochemical processes varies and they provide additional pieces of information that help to speed up the development of the battery field. Measuring the decomposition reactions helps in understanding the safety and failure mechanisms as well as the initial formations inside the battery. The tabletop calorimeter MMC 274 Nexus® connects the small Differential Scanning Calorimeter (DSC) to larger adiabatic reaction calorimeters. Figure 6.6A shows the schematic of the MMC 274 Nexus®. Using this, clear onset temperatures for major events that occur within the cell can be observed and determined.

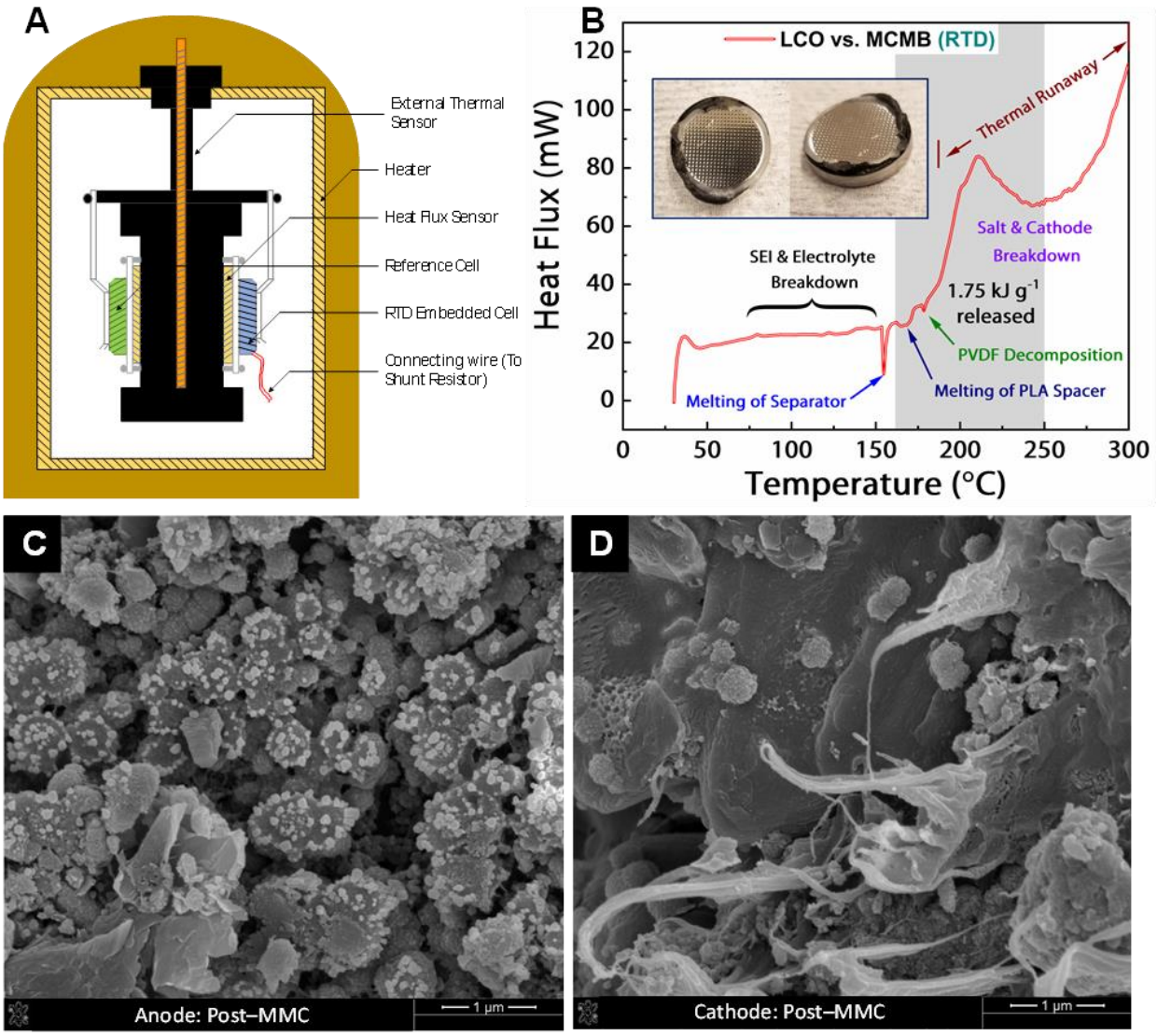

Figure 6.6: Multiple Module Calorimetry and Analysis A: Schematic of tabletop calorimeter MMC 274 Nexus®; and B: Operando MMC signature for RTD embedded LCO-graphite battery (Inset: Post MMC analysis images of RTD embedded cell); High-resolution SEM of C: Anode post-MMC; and D: Cathode post-MMC.

To study the thermal safety aspect after embedding the LIBs with RTD, LCO-MCMB full cells were cycled at 0.1C rate between 3.0 V and 4.2 V. Before the initiation of the calorimetry experiments, the cells were charged to 100% state of charge (SoC, fully lithiated graphite) and then placed inside the MMC chamber. The cells were heated from room temperature to 300 °C at a heating rate of 0.5°C min^{-1}. Several critical steps occur below 300°C, which is responsible for the disintegration of the cell. Hence, the focus was on observing those ignition points before the thermal runaway event occurs. The thermal heat signature for the cell with LCO-MCMB electrode system with 1M $LiPF_6$ in 1:1 (v/v) EC: DEC electrolyte is shown in Fig. 6.6B. Typically, 25 –

60°C range is considered as a normal operating window for the battery, above which the electrolyte could start decomposing. Beyond this range, a variety of reactions occur inside the battery, which leads to electrode disintegration. SEI layer starts to degrade around 80°C and begins reacting with electrolyte starting at 120°C.[33, 69] As shown in Fig. 6.6B, polypropylene separator melts between 155 – 165 °C. Depending on the crystallinity of the polylactic acid, the version used began melting in the range of 170 – 178°C, which can be observed from the heat signature.[70] Following this temperature range is binder decomposition at about 180°C, and then the onset of thermal runaway, which is mainly caused by salt and cathode breakdown, and electrolyte reactions with the lithiated anode. In our previous work,[36] the heat released from 160 – 250 °C for LCO-graphite system was ca. 2.41 $kJ \cdot g^{-1}$. Surprisingly, the installment of RTD leads to a reduced amount of energy released in this range. The heat released from RTD embedded LCO-MCMB full cell was 1.75 $kJ \cdot g^{-1}$. Also, the onset for the conventional cell was 170 °C, whereas in the proposed work there was a delay in the thermal runaway by 10 °C and occurred after 180 °C. The likely reason for the delay in the thermal runaway and lower heat generation is the melting of the PLA spacer. As shown in the inset of Fig. 6.6B, PLA melts and covers the gasket of the coin cell. This prevents the atmospheric oxygen from entering the coin cell to a larger extent delaying the onset of the thermal runaway event. The post-diagnostic image of the conventional coin cell is shown in Fig. D.2. From the image, it can be observed that the whole-cell disintegrated with positive and negative caps being separated from one another. Hence, the RTD embedded PLA spacer assembly acts as a passive safety device inside the battery thus providing additional safety margin. Post diagnostic analysis of electrodes (shown in Fig. 6.6C, D) illustrates that materials have shrunk, and strands of polypropylene separators can be seen on the cathode. Globules of PVDF binders and Super P carbon can be seen on the surface of MCMB. From all the tests performed, it appears that it would be highly beneficial to incorporate RTD inside the batteries to extract valuable data for BMS and enhance the safety aspects of the next-generation batteries. Figure D.6 shows the strategy for operating RTD incorporated LIB in a safe manner to prevent the occurrence of thermal runaway situations, which may be occurring due to various factors like overcharging, short circuit, overheating, etc. BMS helps in monitoring the working temperature of LIB and identify faulty cells, which can be isolated from the pack to mitigate damage to livelihood or properties. Experiments on the larger format cells such as 18650 or 21700 would provide more insights based on the current work.

6.5 Conclusion

As next-generation LIB energy densities increase, safety concerns are the key drivers towards adapting their use in applications like electric vehicles (EVs), unmanned systems, and grid storage. The whole crux of the problem lies in understanding the initiation of thermal runaway, trigger mechanisms, and the ability to predict and prevent the onset of thermal runaway and its often-catastrophic behavior. In this paper, a novel approach was presented and discussed on how to acquire thermal signatures of LIB using RTD sensors. An RTD is embedded in 3D-printed PLA spacer and stationed behind anode for temperature detection. For the ESC test, internal RTD measured 36.4^{o}C that is much higher than 27.4^{o}C measured by the external RTD. During the overcharge abuse test, a record high temperature of 48.4^{o}C was achieved in coin cell configuration. Detection ability, t_{90}, was 14 times faster for internal RTD than the external RTD. Anode temperature profile obtained with internal RTD also showed that the breakdown of SEI and reactions of lithiated graphite with electrolyte are the primary reason for the exothermic heat generation. Thus, these tests signify the importance of acquiring *in situ* temperature measurements to feed as input to BMS to mitigate thermal runaway events. A model was proposed to quantify heat loss during the overcharge and short circuit tests for better prediction of temperature rise and understanding different regions of thermal runaway. According to the multimode calorimetry results, the LIB with RTD stationed generated 1.75 kJ·g^{-1}, which was significantly lower than 2.41 kJ·g^{-1} for a LIB without RTD. Melting of PLA spacer coats coin cell gasket preventing atmospheric oxygen from entering the system to cause more havoc. Thus, RTD assembly apart from its primary function as a thermal monitor act as a passive safety device. Also, it is expected that future advanced BMS would take input from *in situ* thermal monitors for mitigation of mishaps due to thermal runaway events. Based on all the tests performed, chemical reactions explained, and models proposed, it would contribute towards further development of the *in situ* temperature measuring devices.

6.6 Acknowledgement

Authors acknowledge the Davidson School of Chemical Engineering and School of Aeronautics and Astronautics, Purdue University for their financial support in this project. Authors acknowledge the Office of Naval Research (ONR) for supporting the work under the grant

N00014-18-1-2397. VP and VT wish to thank Dr. Michele Anderson from ONR for supporting this work. Authors thank NETZSCH company for MMC 274 Multi-Module Calorimeter with special technical support from Peter Ralbovsky and Peter Vichos.

Funding information: ONR-NEPTUNE, Grant/Award Number: N00014-18-1-2397

6.7 References

1. L.H.J. Raijmakers, D.L. Danilov, R.A. Eichel, and P.H.L. Notten, *Applied Energy* **2019**, 240: p. 918-945.
2. J. Deng, C. Bae, J. Marcicki, A. Masias, and T. Miller, *Nature Energy* **2018**, 3(4): p. 261-266.
3. Q. Wang, P. Ping, X. Zhao, G. Chu, J. Sun, and C. Chen, *Journal of Power Sources* **2012**, 208: p. 210-224.
4. X. Feng, M. Ouyang, X. Liu, L. Lu, Y. Xia, and X. He, *Energy Storage Materials* **2018**, 10: p. 246-267.
5. J.P. Joule, *The Scientific Papers of James Prescott Joule*. Vol. 1. **1884**: Cambridge University Press.
6. W. Hao, Z. Yuan, Y. Xu, S. Zhu, H. Chen, and D. Fang, *Journal of Power Sources* **2019**, 444.
7. R. Xiong, S. Ma, H. Li, F. Sun, and J. Li, *iScience* **2020**, 23(4): p. 101010.
8. H. Arai, M. Tsuda, K. Saito, M. Hayashi, and Y. Sakurai, *Journal of The Electrochemical Society* **2002**, 149(4).
9. P.G. Balakrishnan, R. Ramesh, and T. Prem Kumar, *Journal of Power Sources* **2006**, 155(2): p. 401-414.
10. L.H. Saw, Tay A. A. O., and L.W. Zhang, *IEEE* **2015**.
11. S. Wilke, B. Schweitzer, S. Khateeb, and S. Al-Hallaj, *Journal of Power Sources* **2017**, 340: p. 51-59.
12. H. Park, *Journal of Power Sources* **2013**, 239: p. 30-36.
13. A. Greco, D. Cao, X. Jiang, and H. Yang, *Journal of Power Sources* **2014**, 257: p. 344-355.
14. K. Shah, C. McKee, D. Chalise, and A. Jain, *Energy* **2016**, 113: p. 852-860.
15. T.M. Bandhauer and S. Garimella, *Applied Thermal Engineering* **2013**, 61(2): p. 756-769.
16. D. Anthony, D. Wong, D. Wetz, and A. Jain, *Journal of The Electrochemical Society* **2017**, 164(6): p. A961-A967.

17. M.S.K. Mutyala, J. Zhao, J. Li, H. Pan, C. Yuan, and X. Li, *Journal of Power Sources* **2014**, 260: p. 43-49.
18. N. Martiny, J. Geder, Y. Wang, W. Kraus, and A. Jossen. *Development of a Thin-Film Thermocouple Matrix for In-Situ Temperature Measurement in a Lithium Ion Pouch Cell*. in *Sensors*. 2013. Baltimore, US: IEEE.
19. G. Zhang, L. Cao, S. Ge, C.Y. Wang, C.E. Shaffer, and C.D. Rahn, *Sci Rep* **2015**, 5: p. 18237.
20. J. Cao and A. Emadi, *IEEE Industrial Electronics Magazine* **2011**, 5(1): p. 27-35.
21. M. Debert, G. Colin, G. Bloch, and Y. Chamaillard, *Control Engineering Practice* **2013**, 21(8): p. 1035-1042.
22. L.H.J. Raijmakers, D.L. Danilov, J.P.M. van Lammeren, M.J.G. Lammers, and P.H.L. Notten, *Journal of Power Sources* **2014**, 247: p. 539-544.
23. R. Srinivasan, *Journal of Power Sources* **2012**, 198: p. 351-358.
24. R. Schwarz, K. Semmler, M. Wenger, V.R.H. Lorentz, and M. März, in *IECON 2015 - 41st Annual Conference of the IEEE Industrial Electronics Society*. **2015**, IEEE: Yokohama, Japan. p. 001536-001541.
25. M.R. Giuliano, S.G. Advani, and A.K. Prasad, *Journal of Power Sources* **2011**, 196(15): p. 6517-6524.
26. V.U. Kakade, G.D. Lock, M. Wilson, J.M. Owen, and J.E. Mayhew, *International Journal of Heat and Fluid Flow* **2009**, 30(5): p. 939-949.
27. G. Yang, C. Leitão, Y. Li, J. Pinto, and X. Jiang, *Measurement* **2013**, 46(9): p. 3166-3172.
28. T. Amietszajew, E. McTurk, J. Fleming, and R. Bhagat, *Electrochimica Acta* **2018**, 263: p. 346-352.
29. S. Novais, M. Nascimento, L. Grande, M.F. Domingues, P. Antunes, N. Alberto, C. Leitao, R. Oliveira, S. Koch, G.T. Kim, S. Passerini, and J. Pinto, *Sensors (Basel)* **2016**, 16(9).
30. P. Wang, X. Zhang, L. Yang, X. Zhang, M. Yang, H. Chen, and D. Fang, *Extreme Mechanics Letters* **2016**, 9: p. 459-466.
31. C.Y. Lee, S.J. Lee, M.S. Tang, and P.C. Chen, *Sensors (Basel)* **2011**, 11(10): p. 9942-50.
32. B. Li, M.H. Parekh, R.A. Adams, T.E. Adams, C.T. Love, V.G. Pol, and V. Tomar, *Sci Rep* **2019**, 9(1): p. 13255.
33. E. Peled and S. Menkin, *Journal of The Electrochemical Society* **2017**, 164(7): p. A1703-A1719.

34. N.S.S. Command. *Technical Manual for Navy Lithium Battery Safety Program Responsibilities and Procedures*. 2010 [cited 2019 Oct 1st]; Available from: https://www.public.navy.mil/NAVSAFECEN/Documents/afloat/Surface/CS/Lithium_Batteries_Info/LithBatt_NAVSEA_TMS9310.pdf.
35. S.-M. Park and J.-S. Yoo, *Analytical Chemistry* **2003**, 75(21): p. 455A - 461A.
36. M.H. Parekh, A.D. Sediako, A. Naseri, M.J. Thomson, and V.G. Pol, *Advanced Energy Materials* **2019**.
37. C. Pastor-Fernández, K. Uddin, G.H. Chouchelamane, W.D. Widanage, and J. Marco, *Journal of Power Sources* **2017**, 360: p. 301-318.
38. S.J. An, J. Li, C. Daniel, D. Mohanty, S. Nagpure, and D.L. Wood, *Carbon* **2016**, 105: p. 52-76.
39. M.H. Parekh, V.P. Parikh, P.J. Kim, S. Misra, Z. Qi, H. Wang, and V.G. Pol, *Carbon* **2019**, 148: p. 36-43.
40. R. Spotnitza and J. Franklin, *Journal of Power Sources* **2003**, 113: p. 81-100.
41. R. Ponnappan and T.S. Ravigururajan, *Journal of Power Sources* **2004**, 129(1): p. 7-13.
42. M.A. Pimenta, G. Dresselhaus, M.S. Dresselhaus, L.G. Cancado, A. Jorio, and R. Saito, *Phys Chem Chem Phys* **2007**, 9(11): p. 1276-91.
43. V.A. Sethuraman, L.J. Hardwick, V. Srinivasan, and R. Kostecki, *Journal of Power Sources* **2010**, 195(11): p. 3655-3660.
44. M. Dubarry, C. Truchot, and B.Y. Liaw, *Journal of Power Sources* **2014**, 258: p. 408-419.
45. P. Novák, D. Goers, L. Hardwick, M. Holzapfel, W. Scheifele, J. Ufheil, and A. Würsig, *Journal of Power Sources* **2005**, 146(1-2): p. 15-20.
46. Y. Cheng, Q. Zhang, C. Fang, J. Chen, S. Guo, and X. Che, *Journal of Alloys and Compounds* **2017**, 724: p. 443-449.
47. Y. Cheng, G. Wang, M. Yan, and Z. Jiang, *Journal of Solid State Electrochemistry* **2006**, 11(2): p. 310-316.
48. M.D. Levi and D. Aurbach, *The Journal of Physical Chemistry B* **1997**, 101: p. 4630-4640.
49. Y. Takeda, O. Yamamoto, and N. Imanishi, *Electrochemistry* **2016**, 84(4): p. 210-218.
50. Y. Zeng, K. Wu, D. Wang, Z. Wang, and L. Chen, *Journal of Power Sources* **2006**, 160(2): p. 1302-1307.

51. K. Kumai, H. Miyashiro, Y. Kobayashi, K. Takei, and R. Ishikawa, *Journal of Power Sources* **1999**, 81–82: p. 715–719.
52. K. Xu, S.P. Ding, and J.T. Richard, *Journal of The Electrochemical Society* **1999**, 146.
53. F. Xu, H. He, Y. Liu, C. Dun, Y. Ren, Q. Liu, M.-x. Wang, and J. Xie, *Journal of The Electrochemical Society* **2012**, 159(5): p. A678-A687.
54. Y.V. Mikhaylik and J.R. Akridge, *Journal of The Electrochemical Society* **2003**, 150(3).
55. T.D. Hatchard, D.D. MacNeil, A. Basu, and J.R. Dahn, *Journal of The Electrochemical Society* **2001**, 148(7).
56. O.S. Burheim, M.A. Onsrudc, J.G. Pharoahd, F. Vullum-Bruerc, and P.J.S. Vieg, *ECS Transactions* **2014**, 58(48): p. 145-171.
57. X.D. Chen and X. Peng, *Drying Technology* **2005**, 23(1-2): p. 83-103.
58. V. Yufit, P. Shearing, R.W. Hamilton, P.D. Lee, M. Wu, and N.P. Brandon, *Electrochemistry Communications* **2011**, 13(6): p. 608-610.
59. H.-S. Bus, S.Z.D. Cheng, and B. Wunderlich, *Die Makromolekulare Chemie, Rapid Communications* **1988**, 9: p. 75-77.
60. S. Picard, D.T. Burns, and P. Roger, *Metrologia* **2007**, 44(5): p. 294-302.
61. T.E. Pochapsky, *Acta Metallurgica* **1953**, 1: p. 747-751.
62. M. Pyda, R.C. Bopp, and B. Wunderlich, *The Journal of Chemical Thermodynamics* **2004**, 36(9): p. 731-742.
63. G.K. White and S.J. Collocott, *Journal of Physical and Chemical Reference Data* **1984**, 13(4): p. 1251-1257.
64. Y. Chernyak and J.H. Clements, *Journal of Chemical and Engineering Data* **2004**, 49: p. 1180-1184.
65. P. Auerkari, K. Tirronen, Editor. **1996**, Technical Research Centre of Finland: Espoo. p. 26.
66. P. Gotcu-Freis, D.M. Cupid, M. Rohde, and H.J. Seifert, *The Journal of Chemical Thermodynamics* **2015**, 84: p. 118-127.
67. J.J. Valencia and P.N. Quested, *ASM Handbook* **2013**, 15: p. 468-481.
68. V. Pokorný, V. Štejfa, M. Fulem, C. Červinka, and K. Růžička, *Journal of Chemical & Engineering Data* **2017**, 62(10): p. 3206-3215.
69. N.E. Galushkin, N.N. Yazvinskaya, and D.N. Galushkin, *Journal of The Electrochemical Society* **2018**, 165(7): p. A1303-A1308.

70. J. Lunt, *Polymer Degradation and Stability* **1998**, 59(1-3): p. 145-152.

7. CONCLUSIONS AND FUTURE DIRECTIONS

7.1 Conclusions

The growth of EVs and other energy-dense applications is bound to expand beyond imagination and along with that of LIBs. On the trends of Moore's Law, the energy-storing capabilities have increased significantly over the past few decades, however, they fall short of the expectations, leaving the scope of improvements.[1] This thesis has attempted to address many of these shortcomings through novel material development, discovering a novel configuration to LIBs, and an internal temperature monitoring method. Silicon-carbon composite developed, delivered a high capacity of 500 mAh g^{-1} at 500 mA g^{-1} current density over 100 cycles. Through in situ ETEM, we witnessed the evolution of composite with temperature and through operando calorimetry experiments, the thermal signature of full-cells was elucidated. With the development of high-capacity anode material, there is an ardent need for a high-capacity cathode. However, cathodes such as vanadium pentoxide, sulfur, etc., which do possess inherent high capacities, are devoid of lithium-ions in their crystal lattice. Through the novel architecture of reserve lithium-ion batteries, in situ lithiation was achieved and realization of MCMB vs. V_2O_5 full-cell was made. The first cycle charge capacity achieved was 264 mAh g^{-1}. RLIB is a lucrative system for in situ lithiation of lithium-free cathodes, for compensating SEI layer formation Li^+ ions losses, effectively balancing the positive and negative electrodes, and refuel Li^+ ions after the capacity fade.

Separators can change the effective ionic conductivity of electrolytes by 15–20% and develop issues of concentration polarization, overpotentials, etc.[2] Aramid nanofibers synthesized through critical point drying method outperforms the mainstay of the industry i.e., polyolefin separator in aspects of mechanical strength, wettability, electrochemical performance, and thermal safety. After being exposed to temperatures from room temperature to 300 °C, the CPD-ANF separator retains its structural integrity. For Li-S batteries, a modified microporous separator comprising of PP separator covered with polydopamine and a thin coat of graphene acted as a barricade for polysulfides from shuttling across. Tailored separator achieves *trifecta* (enhances the conductivity of sulfur cathode, suppresses polysulfide shuttling, and mitigates lithium dendrite growth).

Incidents of thermal runaway, battery fires, or explosion affect the perception of the people towards the technology, and indirectly affecting the businesses to a greater extend. Detecting, predicting, and mitigating these incidents are essential for the safe functioning of the appliances. The utilization of an internal RTD sensor had detecting capabilities (t_{90}) ~14 faster than external temperature measurement. The temperature difference of 9 ℃ and 20 ℃ was detected for external short-circuit and overcharge tests, respectively. The future advanced battery management systems would benefit from the output of such internal temperature sensing devices.

7.2 Future Directions

7.2.1 Silicon Anodes

As silicon is the choice of material for next-generation LIBs, an astonishingly high amount of progress has been made towards the practical realization of silicon anodes have been made. On account of their poor ICE, the development of electrolytes with enhanced additives that would help build effective SEI across the surface is critical. In situ lithiation through RLIBs could be explored to help recover this loss. Crystalline silicon nanoparticles are known to crack, fracture, and pulverize during the first cycle,[3] novel materials with amorphous silicon should be developed for a high-performance anode. Silicon reacts with Li to form lithium silicide, however, $Li_{21}Si_5$ (~4200 mAh g^{-1}) could be formed only at elevated temperatures compared to $Li_{15}Si_4$ (~3579 mAh g^{-1}), formed at room temperature. More efforts can be diverted towards gaining more insights into these formations and developing rational methods to plausibly unlock extra capacity at lower temperatures.

7.2.2 Reserve Lithium-ion Batteries

For conventional LIBs, after the formation of the SEI layer on the anode surface, the cathode cannot return to its fully lithiated state.[4] There are empty voids, which are left inside the cathode crystal structure from the losses of Li^+. With the help of RLIBs, various scientific studies may be conducted for an even higher understanding of electrochemical processes occurring inside the batteries. They are as follows: **A:** When the SEI layer is formed on the anode surface through the reservoir, the cathode remains in its pristine condition. The formation of the cathodic

electrolyte interface (CEI) may be different compared to the conventional system. Through XPS, XAFS, and other surface characterizations techniques, this could be revealed. **B:** After the change of mode from the reservoir to full-cell mode, there is a change in voltage characteristics, with more resemblance to half-cell behavior. This strikingly remarkable difference in the voltage characteristics can be deconvoluted through modeling simulations. **C:** As the cathode does not lose any Li^+ ions during initial cycling, at higher voltages (>4.2 V) the performance of the cathode may be different, and this can be observed through the changes in the ratio of the c/a axis using in situ XRD. **D:** The diffusion behavior of lithium-ion becomes sluggish in the few vacancies of Li-layered cathode. This could be different for RLIBs, as there are no vacancies due to no Li^+ ion losses. Using molecular dynamics simulation, the transport of lithium-ions into the cathode can be understood effectively. **E:** Due to the presence of the porous current collector, lithium-ions can travel through the materials (especially in the direct–mode). Transport studies can be carried out to understand the motion of Li^+ ions across the electrode, the tortuous pathway, and the concentration gradient that may result. **F:** Long-term cycling may result in the breakdown of SEI and reconstruction of SEI follows. Various other side reactions occur leading to loss of Li^+ ions. The RLIB reservoir electrode has provision to boost the faded capacity. However, the boost that was seen at the laboratory scale was marginal. The industrial scale-build RLIB may help in elucidating if boost would truly work, and if not in identifying the causes of fade i.e., if it is the exhaustion of electrolyte, degradation of the cathode, or the loss of lithium-ions that is the major contributing factor. **G:** Through rigorous detailed mass and energy balance calculations, the questions about how practical this system would be can be obtained. Also, the optimum thickness of the reservoir for the supplement, SEI loss recovery, and boosting can be derived. **H:** Based on the understanding of the Direct–mode in RLIBs, it may be possible to use a single reservoir for multi-layered pouch cells or cylindrical configuration cells. Mechanical designing iterations would help develop, the ideal location of the reservoir inside the larger configuration batteries. **I:** Most importantly, when RLIB are operating as conventional batteries, the reservoir remains electrochemically isolated. Using DFT and MD simulations, the study of the stability of reservoir electrode would be an interesting topic!

7.2.3 Separators

Aramid nanofibers separators are relatively recent separator systems that have been developed for LIBs. The studies that have been conducted on polyolefin separators may well be applied for ANF separators too. During cycling, active material, Li-metal, SEI can deposit on the surface of separators and apply compressive stress on them, cause localized heating or other interactions. Thus, it becomes critical to observe the impact of separators on the transport of Li^+ ions. Tortuosity, permeability, Gurley value are some unexplored territories for CPD-ANF separator as well as the tailored separator for Li-S batteries. Using FIB-SEM and X-ray phase tomography parameters viz., porosity, tortuosity, pore dimensions can be extracted. Various studies explain the effective transport of Li+ ions across the separators, however, the interactions of Li^+ ions with the separator surface are not completely understood. There are different interactions (polar, ionic, van der Waals, hydrophobic) between the surface of electrolyte and electrolyte molecules (ions and solvent molecules), which can impact electrolyte viscosity and thereby influencing transference number (t_+) and conductivity (σ). Interfacial interactions can be understood from contact angle and surface tension (γ), Hanson solubility parameter. Also, Flory-Higgins thermodynamic interaction parameter (χ) can help explain the swelling of polymer chains of a separator after interaction with different solvents. These fundamental analyses can broaden our understanding of the inactive components of the batteries.

7.2.4 Thermal Sensors

The promising results from the coin-cells suggest the exploration into a larger configuration like multi-layered pouch cells and cylindrical cells. The cost-to-benefit ratio calculations could be a useful criterion when developing it for practical applications. Development and integration of RTD with battery management systems are yet to be explored. The feasibility of the incorporation of RTD in every cell needs to be determined. Impedance–based method, which is non-invasive and sensor less technology needs significant development and would be more desired for its obvious advantages compared to other techniques. It is envisioned that there would be a single chip with multiple sensors embedded in it for different purposes and the art of incorporation developed through this project would come useful in the future.

7.3 References

1. F. Schlachter, *Proc Natl Acad Sci U S A* **2013**, 110(14): p. 5273.
2. M.F. Lagadec, R. Zahn, and V. Wood, *Nature Energy* **2018**, 4(1): p. 16-25.
3. M.T. McDowell, S.W. Lee, W.D. Nix, and Y. Cui, *Advanced Materials* **2013**, 25(36): p. 4966-4985.
4. T. Li, X.-Z. Yuan, L. Zhang, D. Song, K. Shi, and C. Bock, *Electrochemical Energy Reviews* **2019**, 3(1): p. 43-80.

APPENDIX A. CHAPTER 2: SUPPORTING INFORMATION

A.1 In situ Electron Microscopy Analysis

The baking of precursor at 600 °C for 2 hours is performed in order to transition the highly disordered starch into a homogeneous amorphous structure following the expected pathway shown in equation 1, along with other connecting reactions between the graphite and silicon. It is this transition that is crucial to understand scientifically.

$$(C_6H_{10}O_5)_n \rightarrow C_{(s)} + H_2O_{(g)} + other \quad (1)$$

To directly observe this transition, the electron microscopy for this work was performed using Hitachi HF3300 at the University of Toronto, operating at 300kV, in the Scanning Transmission Electron Microscopy (STEM) mode. This operational setting allowed full characterization of the same for cross sectional imaging, surface imaging, and elemental analysis. Experiments were on the individual sample "ingredients", as well as the anode material to show how each component evolved over time, as well as how the components interact during heating.

The samples were delivered as a powder and were applied to the ETEM substrate through mechanical powder coating, with the final coating shown in Fig. A.1-A. The powder coating does not affect the temperature sensitive and soluble sample, resulting in a representative final sample for the experiments. The downside of this procedure is apparent however, as it heavily coats the entire substrate, not simply the central heating area. The non-localized coating does require a post-coating cleaning of the MEMS chip contacts with an organic solvent to ensure clean electrical contact and accurate heating control.

The heating profile is shown in Fig. A.1-D, with samples were first pre-heated in the ETEM to 150 °C. This preheating allowed for image capture without electron beam deposited contamination, while staying below any transition points for the sample. Following initial imaging, the sample was heated for imaging following a slow ramp up at 0.2 deg $°C^{-1}$. This rate is optimum for capturing material transformations while allowing for image capture at each 25 °C. In each case, EDS elemental mapping, along with STEM/BF/DF was performed before and after the experiments to confirm the observed elements. Energy dispersive X-ray (EDS) analysis provides an elemental map of the particles based on the characteristic X-rays emitted by the sample when

it is struck by the electron beam. STEM/BF/DF uses a combination of secondary electron detectors and transmission electron detectors to generate three images: a 3D surface image (STEM), a diffracted image of the cross section dark field (DF), and a direct image of the cross section (BF). The BF and DF images are sensitive to the elements present, and clearly show different elements with different brightness. This allows for easy identification of elements if the sample composition is known.

A.2 Heat Evolution Calculations

Chemistry	Graphite / LCO	GCSi / LCO	Units
Heat evolved*	2.41	2.81	kJ g^{-1}
Specific Capacity of Full Cell	111.69	134.45	mAh g^{-1}
Heat evolved per specific capacity of cell	**21.56**	**20.89**	kJ Ah^{-1}

*Heat evolution data includes mass of anode, cathode and electrolyte.

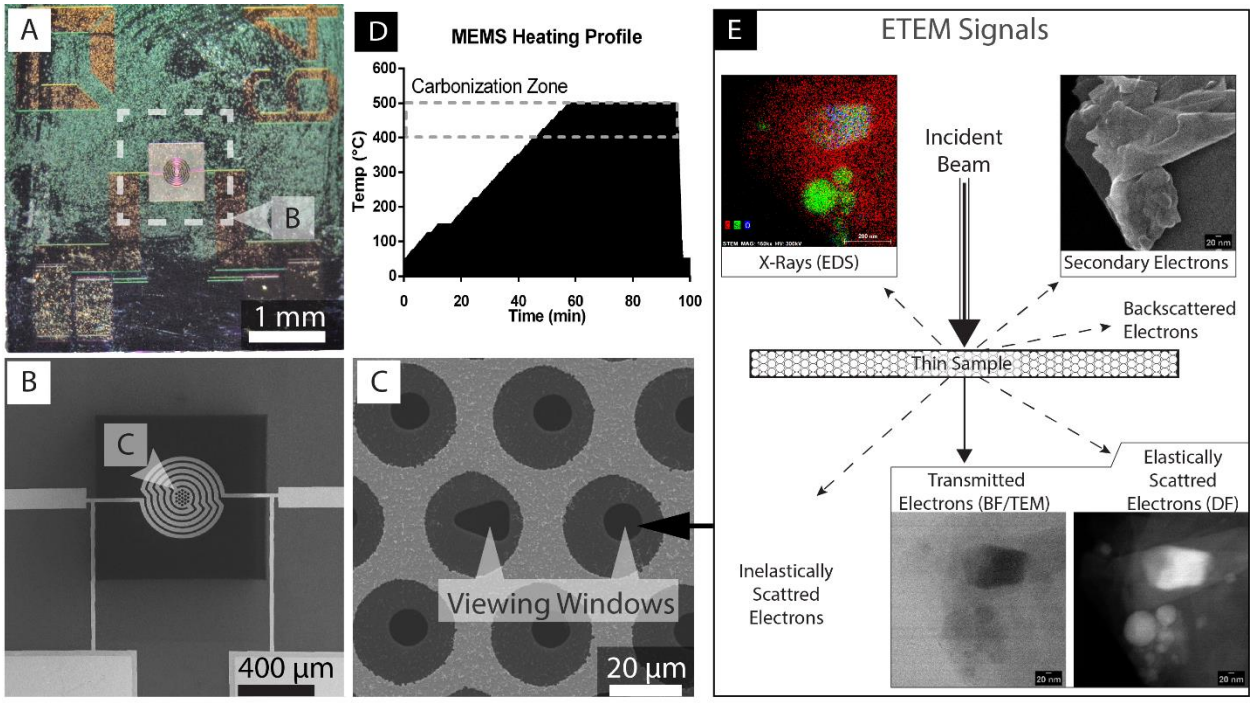

Figure 7.1: A: High Resolution ETEM MEMS substrate after mechanical powder coating. B: SEM image of central spiral heater as well as 4 probe resistance measurement contacts C: Closeup SEM of SiN viewing windows at the center of the MEMS substrate. E: Summary of all signals used for in situ ETEM characterization

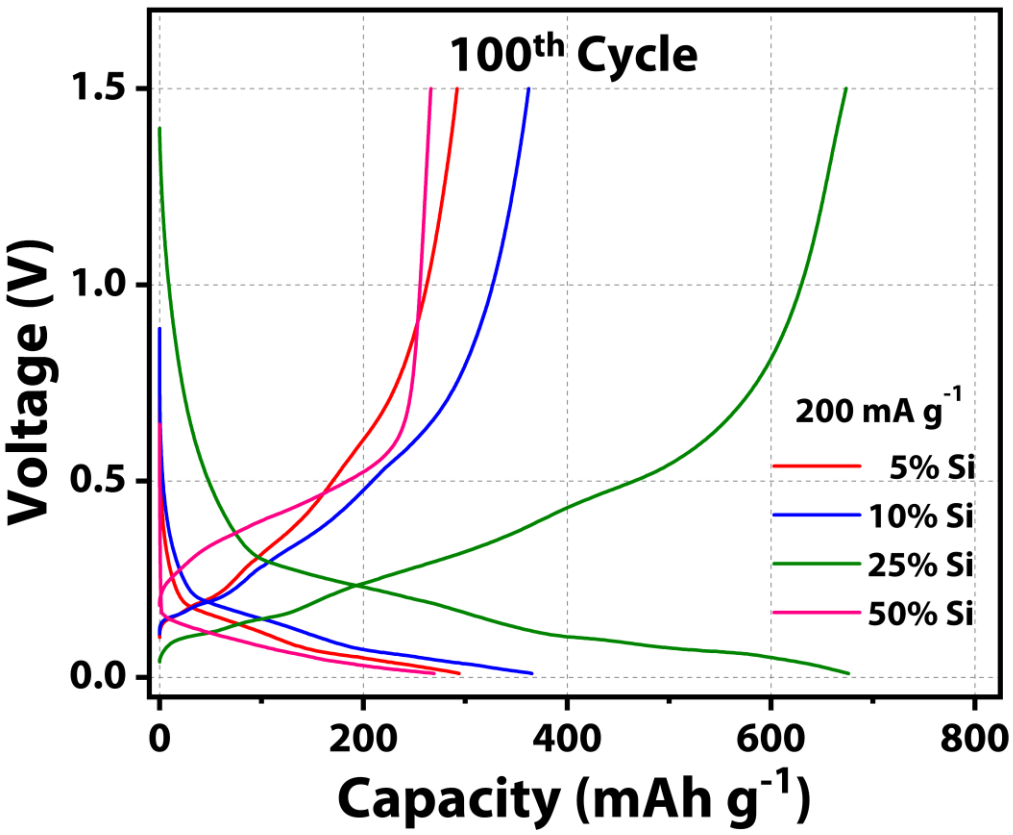

Figure 7.2: Voltage profiles of 100th cycle for composites with varying silicon content.

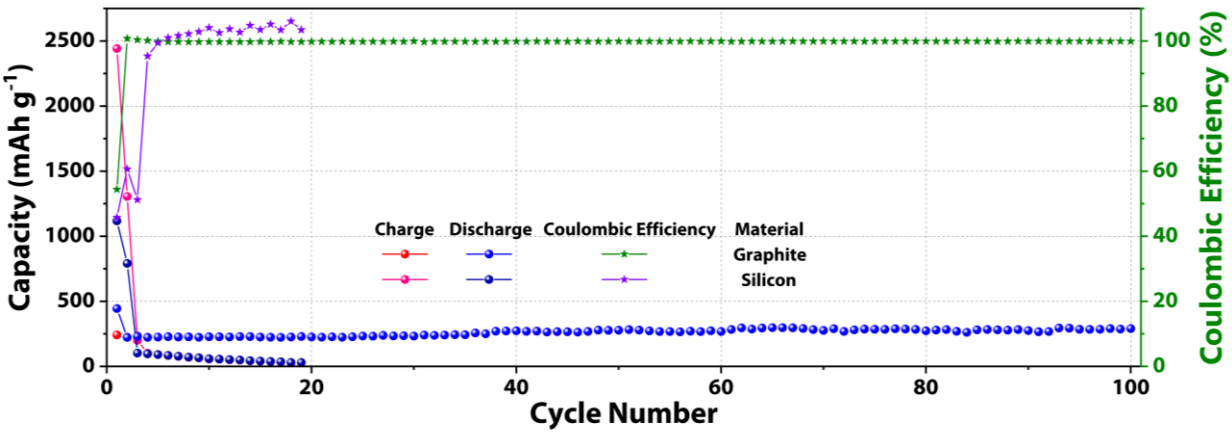

Figure 7.3: Charge–discharge cycling test of graphite and silicon electrodes at 1C rate.

APPENDIX B. CHAPTER 3: SUPPORTING INFORMATION

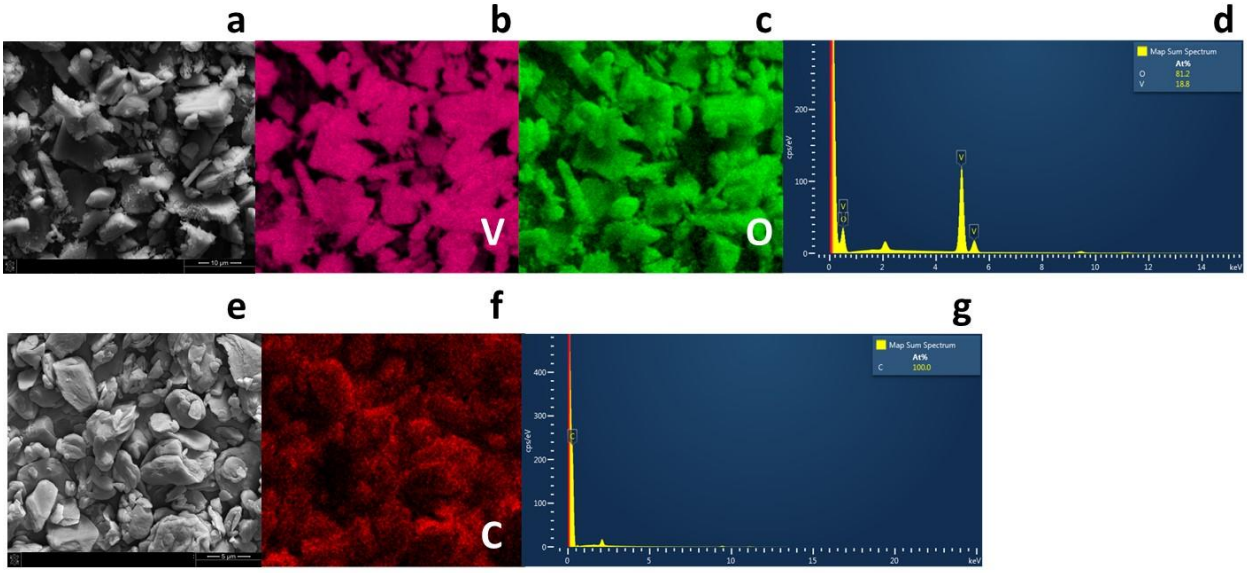

Figure 7.4: Surface morphology and elemental mapping analysis of V_2O_5 and MCMB electrode materials: A: V_2O_5 surface morphology with the corresponding elemental mapping of B: V, C: O and D: energy dispersive X-ray analysis spectrum for the presence of V, and O elements. E: Surface morphology of MCMB with the elemental mapping analysis indicates the presence of F: C and G: energy dispersive X-ray analysis of MCMB spectrum for the simultaneous deduction of C element.

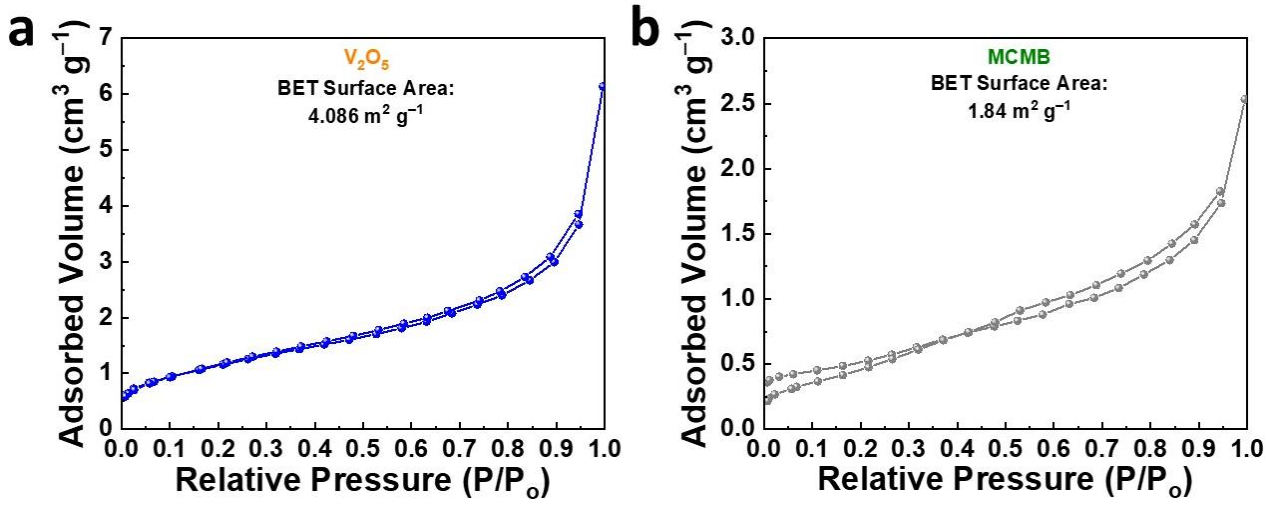

Figure 7.5: BET N_2 adsorption-desorption analysis of A: V_2O_5; and B: MCMB.

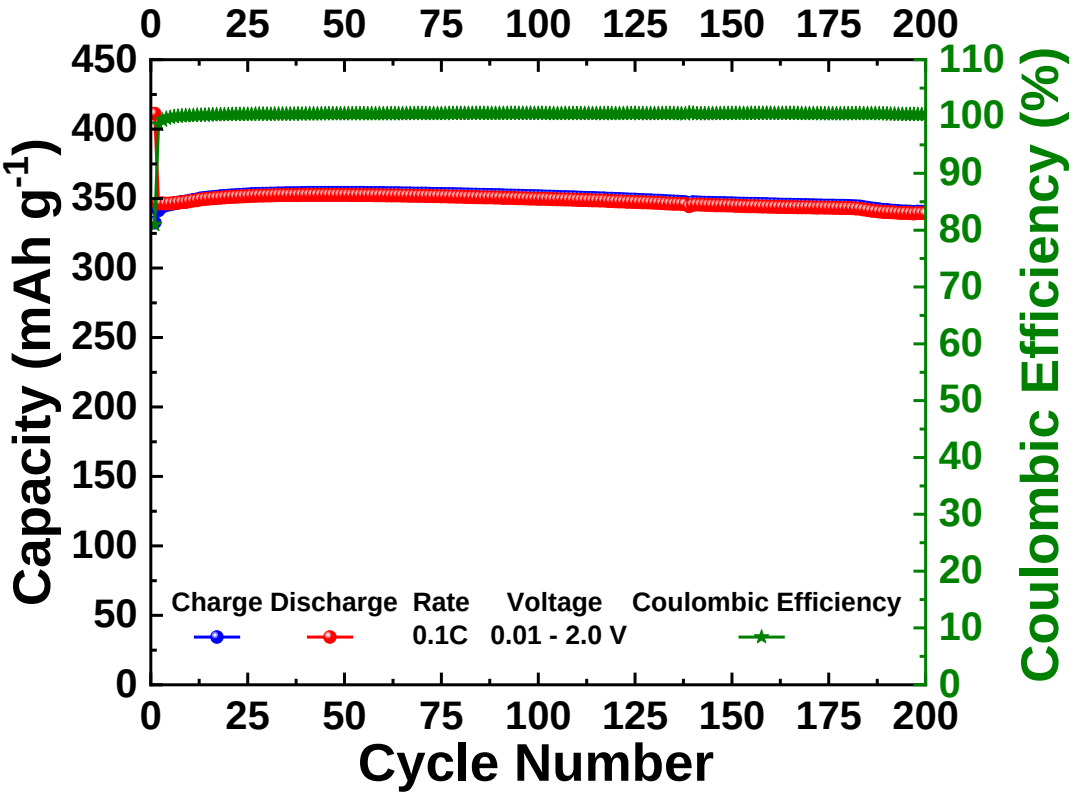

Figure 7.6: Electrochemical performance of Li/MCMB half–cell at 0.1C rate cycled between 0.01V – 2.0V.

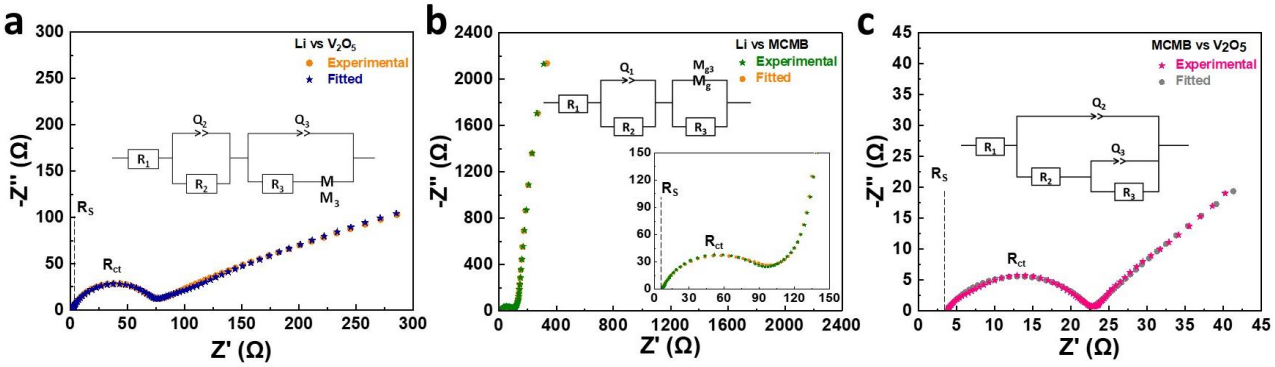

Figure 7.7: EIS of A: Li/V_2O_5 half–cell; B: Li/MCMB half–cell; and C: V_2O_5-MCMB Full–cell.

Table 7.1: Experimental and fitted electrochemical impedance results of Li/MCMB, Li/$LiFePO_4$, MCMB/V_2O_5, RLIB – Li/MCMB, MCMB/V_2O_5 and Li/V_2O_5.

#	Modes	Equivalent Circuit	Impedance components R in ohms and C in farad	Phase element (Φ)
1	Li/MCMB	$R_1 + \frac{Q_1}{R_2} + \frac{Mg_3}{R_3}$	R_1 = 6.807, R_2 = 85.51, R_3 = 150.4 R_4 = 27.92	$Q_1 = 31.86 \times 10^{-6}$, a_1 = 0.836, t_3 = 0.281, g_5 =0.82
2	Li/V_2O_5	$R_1 + \frac{Q_2}{R_2} + \frac{Q_3}{R_3 + M_3}$	R_1 = 1.966, R_2 = 66.12, R_3 = 0.148	$Q_2 = 9.9 \times 10^{-6}$, $Q_3 = 5.797 \times 10^{-3}$ a_2 = 0.858, a_3 = 0.2135, td_3 = 283.7
3	MCMB/V_2O_5	$R_1 + \frac{Q_2}{R_2 + \frac{Q_3}{R_3}}$	R_1 = 3.7, R_2 = 18.89, R_3 = 328.9	$Q_1 = 48.08 \times 10^{-6}$, Q_3 = 0.1609, a_1 = 0.679, a_3 = 0.5506
4	RLIB – Li/MCMB	$R_1 + \frac{Q_2}{R_2 + W_2} + C_3$	R_1 = 1.902, R_2 = 69.75, C_2 = 0.012	$Q_2 = 21.97 \times 10^{-6}$, s_2 = 44.21, a_2 = 0.823
5	RLIB – MCMB/V_2O_5	$R_1 + \frac{C_2}{R_2} + \frac{C_3}{R_3 + Ma_4}$	R_1 = 1.669, R_2 = 4.72, R_3 = 12.42, R_4 = 47.25 (Ma_4), $C_2 = 70.39 \times 10^{-6}$, $C_3 = 3.179 \times 10^{-6}$	t_4 = 0.251, a_4 = 0.9601
6	RLIB – Li/V_2O_5	$R_1 + \frac{C_2}{R_2 + \frac{Q_2}{R_3 + \frac{Q_4}{R_4}}}$	R_1 = 4.43, R_2 = 27.43, R_3 = 257.9, R_4 = 173.2, $C_2 = 1.3 \times 10^{-6}$	$Q_2 = 23.4 \times 10^{-6}$, $Q_4 = 7.026 \times 10^{-3}$ a_2 = 0.7884, a_4 = 0.417

APPENDIX C. CHAPTER 5: SUPPORTING INFORMATION

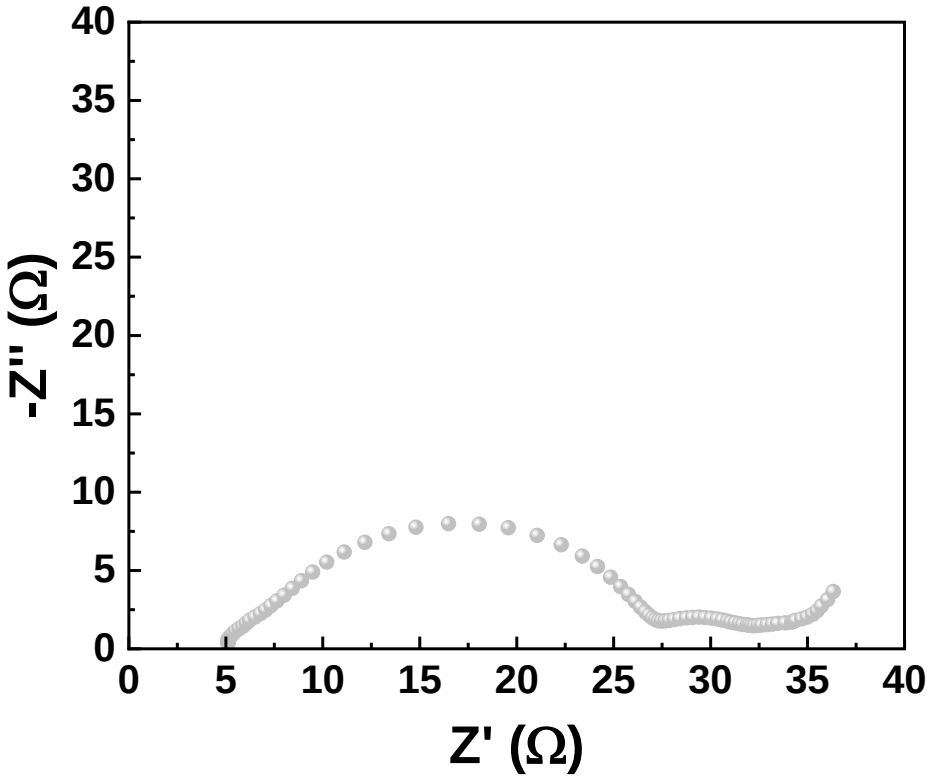

Figure 7.8: EIS of Li-S cell with conventional PP separator

APPENDIX D. CHAPTER 6: SUPPORTING INFORMATION

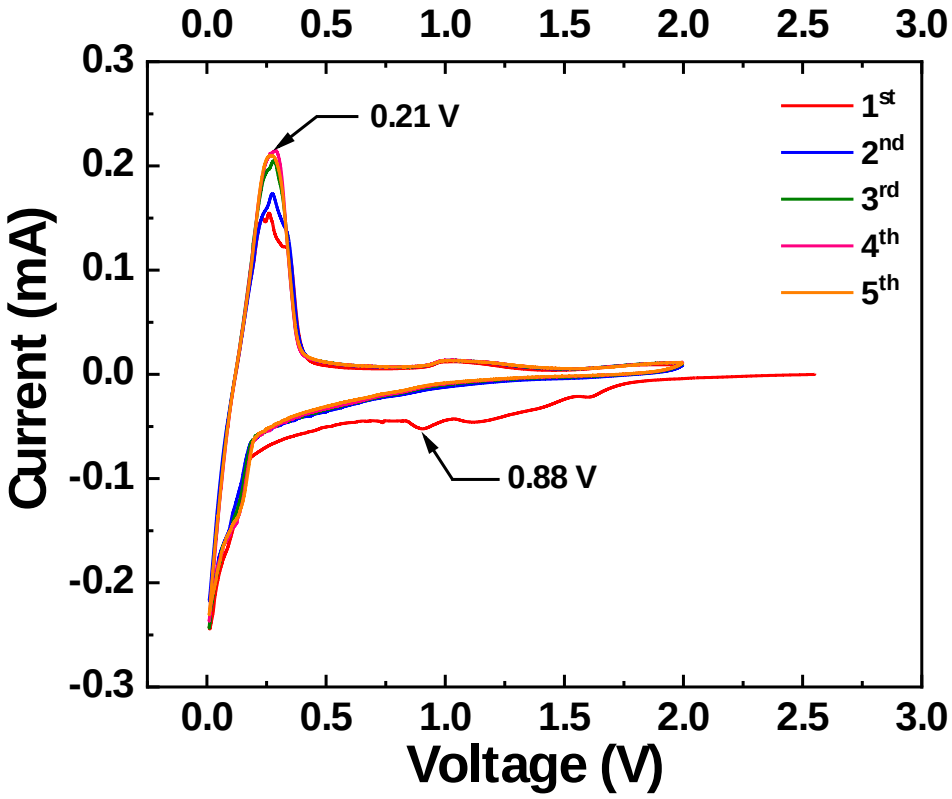

Figure 7.9: Cyclic Voltammetry of the first five cycles for MCMB-Half Cell with embedded RTD obtained at 0.1 mVs^{-1}.

Figure 7.10: Post MMC analysis images of an LCO-MCMB cell without RTD sensor.

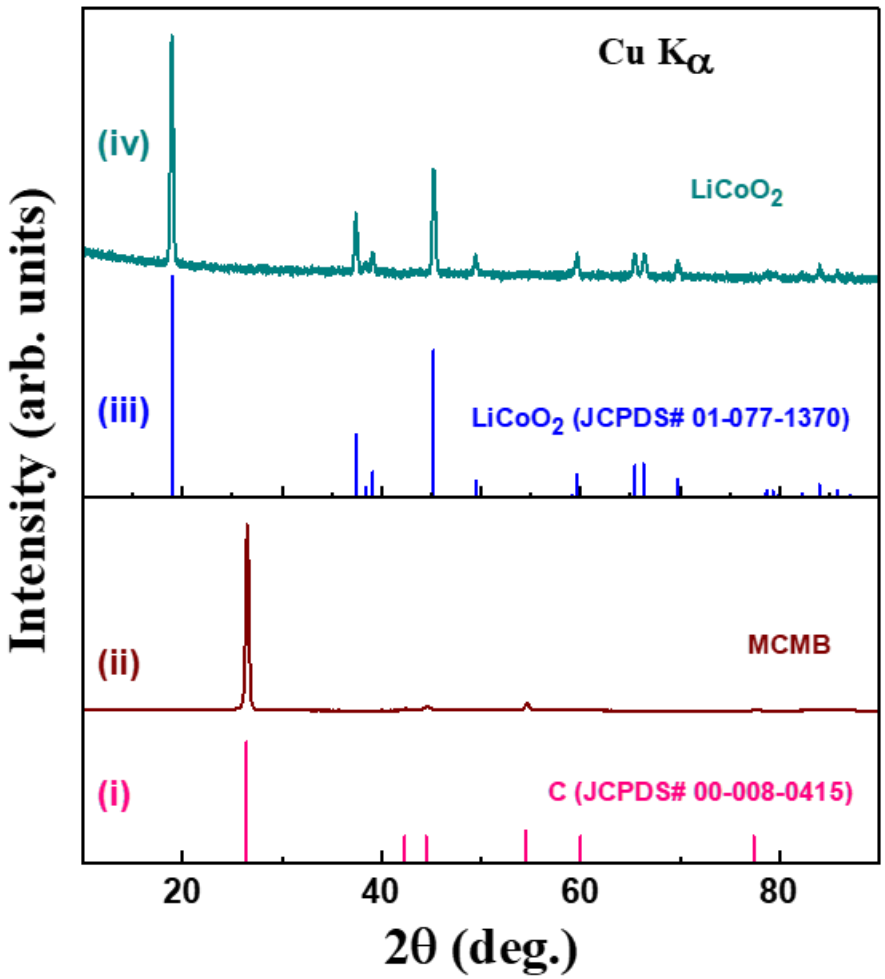

Figure 7.11: Powder X-ray diffraction pattern of electrode materials MCMB (blue) and $LiCoO_2$ (green).

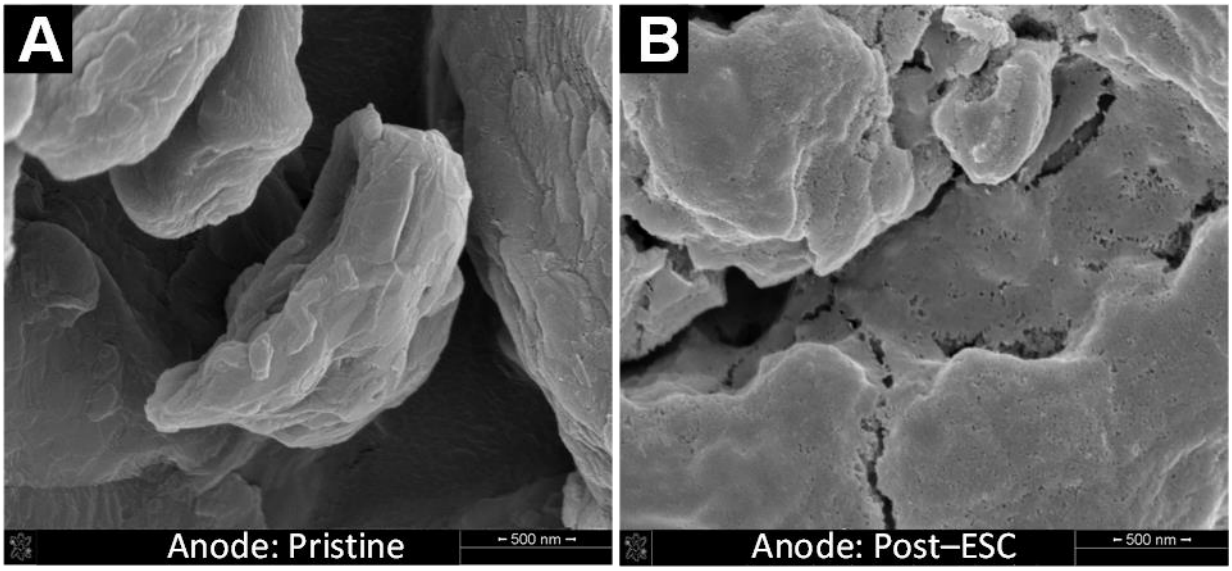

Figure 7.12: High-resolution SEM of A: Pristine MCMB Anode; and B: MCMB Anode Post–External Short Circuit Test.

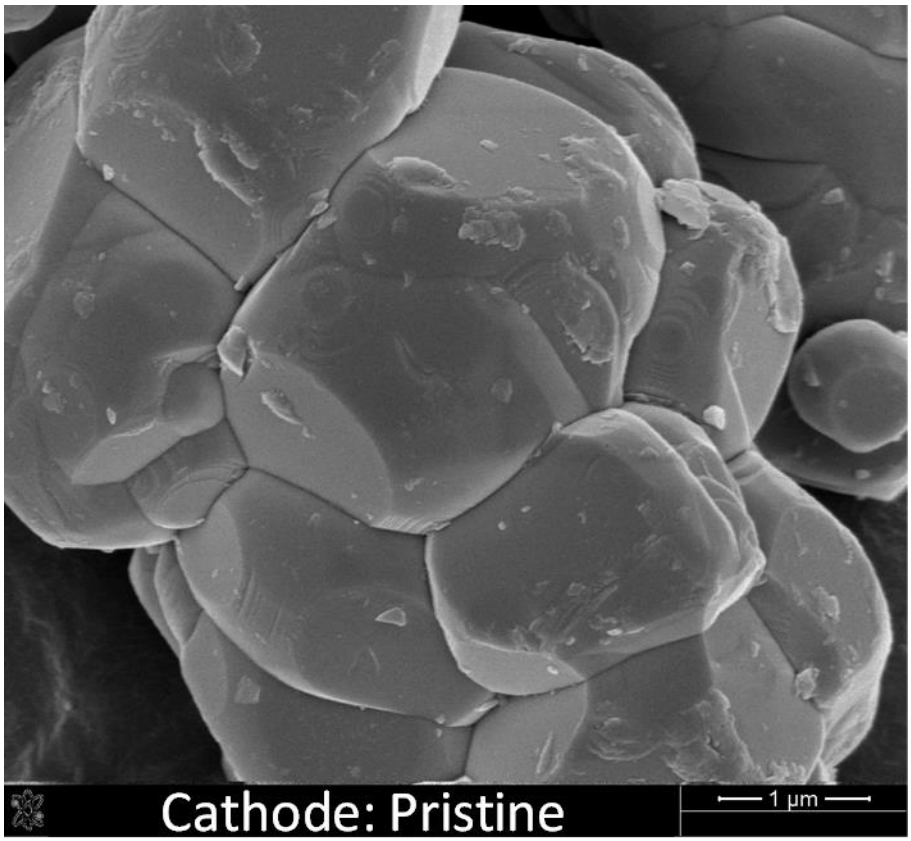

Figure 7.13: High-resolution SEM of Pristine LCO Cathode.

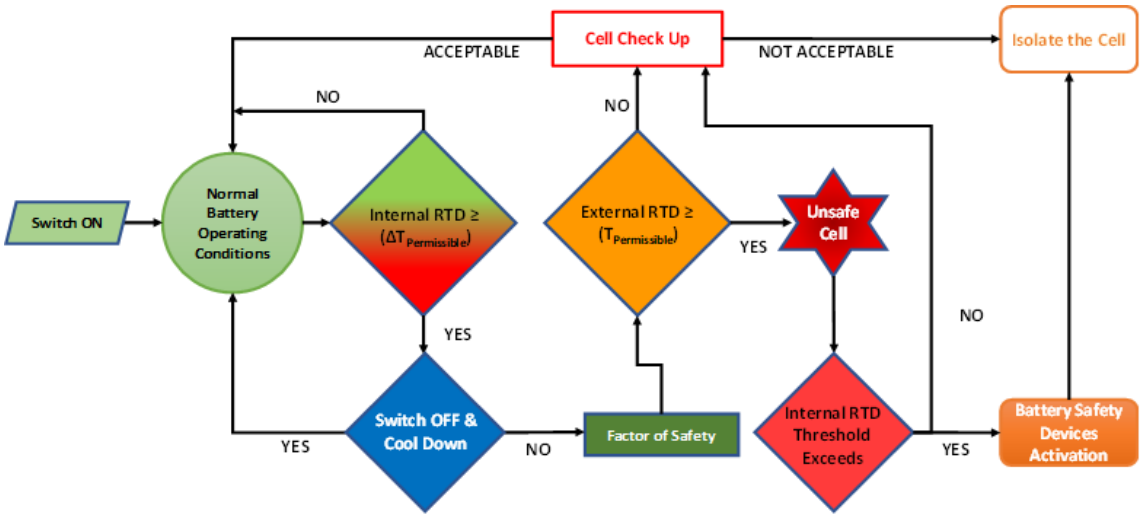

Figure 7.14: Strategy for mitigating thermal runaway event using internal RTD.

Table 7.2: Recent temperature monitoring techniques with their advantages and disadvantages

Sr. No.	Sensor	Advantages	Disadvantages	Reference
1	**Thermocouples**	Robustness, temperature range, low cost	Corrosion issues, isolation from the electrolyte, special arrangements for in situ detection	[1], [2], [3]
2	**Thermistors**	Used as protection devices, inexpensive, small size	Placed on terminals, near or on the surface of the battery, limited application	[4], [5], [6]
3	**Impedance-based**	Non-invasive and sensor less technique	Interference from electric current, aging and SoC dependencies, large charge/discharge DC currents	[7], [8], [9], [10], [11]
4	**Fiber Bragg grating**	Lightweight, high sensitivity, small size, resistance to interference from electromagnetic and radio waves	Still under development, variable temperature range due to fiber coating	[12], [13], [14],
5	**Thermal imaging- liquid crystal thermography**	Thermal map of the entire surface	Expensive, delicate and impractical	[15], [16], [17]
6	**RTDs**	Economical, lightweight, reliability, accuracy	*Capacity loss due to in situ measurements, limited extended cycling	[18], [19], [20], [21]

* Prior to the current work

D.1 References

1. M.S.K. Mutyala, J. Zhao, J. Li, H. Pan, C. Yuan, and X. Li, *Journal of Power Sources* **2014**, 260: p. 43-49.
2. N. Martiny, J. Geder, Y. Wang, W. Kraus, and A. Jossen. *Development of a Thin-Film Thermocouple Matrix for In-Situ Temperature Measurement in a Lithium Ion Pouch Cell*. in *Sensors*. 2013. Baltimore, US: IEEE.
3. G. Zhang, L. Cao, S. Ge, C.Y. Wang, C.E. Shaffer, and C.D. Rahn, *Sci Rep* **2015**, 5: p. 18237.
4. J. Cao and A. Emadi, *IEEE Industrial Electronics Magazine* **2011**, 5(1): p. 27-35.

5. M. Debert, G. Colin, G. Bloch, and Y. Chamaillard, *Control Engineering Practice* **2013**, 21(8): p. 1035-1042.
6. J. Grosch, E. Teuber, M. Jank, V. Lorentz, M. März, and L. Frey, *IEEE* **2015**.
7. L.H.J. Raijmakers, D.L. Danilov, J.P.M. van Lammeren, M.J.G. Lammers, and P.H.L. Notten, *Journal of Power Sources* **2014**, 247: p. 539-544.
8. J.P. Schmidt, S. Arnold, A. Loges, D. Werner, T. Wetzel, and E. Ivers-Tiffée, *Journal of Power Sources* **2013**, 243: p. 110-117.
9. R. Srinivasan, *Journal of Power Sources* **2012**, 198: p. 351-358.
10. K.S. Champlin. **2001**: United States of America.
11. R.R. Richardson, P.T. Ireland, and D.A. Howey, *Journal of Power Sources* **2014**, 265: p. 254-261.
12. G. Yang, C. Leitão, Y. Li, J. Pinto, and X. Jiang, *Measurement* **2013**, 46(9): p. 3166-3172.
13. T. Amietszajew, E. McTurk, J. Fleming, and R. Bhagat, *Electrochimica Acta* **2018**, 263: p. 346-352.
14. S. Novais, M. Nascimento, L. Grande, M.F. Domingues, P. Antunes, N. Alberto, C. Leitao, R. Oliveira, S. Koch, G.T. Kim, S. Passerini, and J. Pinto, *Sensors (Basel)* **2016**, 16(9).
15. X. Du, Q. Wu, Y.-N. Wang, T.-S. Pan, Y.-M. Wei, H.-S. Chen, W.-L. Song, and D.-N. Fang, *Journal of Power Sources* **2020**, 446.
16. M.R. Giuliano, S.G. Advani, and A.K. Prasad, *Journal of Power Sources* **2011**, 196(15): p. 6517-6524.
17. V.U. Kakade, G.D. Lock, M. Wilson, J.M. Owen, and J.E. Mayhew, *International Journal of Heat and Fluid Flow* **2009**, 30(5): p. 939-949.
18. S. Zhu, J. Han, H.-Y. An, T.-S. Pan, Y.-M. Wei, W.-L. Song, H.-S. Chen, and D. Fang, *Journal of Power Sources* **2020**, 456.
19. P. Wang, X. Zhang, L. Yang, X. Zhang, M. Yang, H. Chen, and D. Fang, *Extreme Mechanics Letters* **2016**, 9: p. 459-466.
20. C.Y. Lee, S.J. Lee, M.S. Tang, and P.C. Chen, *Sensors (Basel)* **2011**, 11(10): p. 9942-50.
21. B. Li, M.H. Parekh, R.A. Adams, T.E. Adams, C.T. Love, V.G. Pol, and V. Tomar, *Sci Rep* **2019**, 9(1): p. 13255.

PUBLICATIONS

1. M. H. Parekh, A. D. Sediako, A. Naseri, M. J. Thomson, V. G. Pol, *Adv. Energy Mater*. 1902799, 2019, 1903690.
2. M. Palanisamy, M. H. Parekh, V. G. Pol, *Adv. Functional Mater*. 2003668 2020.
3. M. H. Parekh, V. P. Parikh, P. J. Kim, S. Misra, Z. Qi, H. Wang, V. G. Pol, *Carbon*, 2019, 148, 36-43.
4. M. H. Parekh, B. Li, M. Palanisamy, T. E. Adams, V. Tomar, V. G. Pol, *ACS Appl. Energy Mater*. 2020, 3, 8, 7997-8008.
5. B. Li, M. H. Parekh, R. A. Adams, T. E. Adams, C. Love, V. G. Pol, V. Tomar, *Scientific Reports*, 2019, 9, 13255., 2019, 1903690.
6. V. P. Parikh, A. Ahmadi, M. H Parekh, F. Sadeghi, V. G. Pol, *Environ. Sci. Technol*., 2019, 53, 3757−3763.
7. M. Palanisamy, V. P. Parikh, M. H. Parekh, V. G. Pol, *Energy Technology*, 2020, 2000094.
8. M. N. Carter, M. H. Parekh*, V. Tomar, E. Dietz, V. G. Pol, *Applied Clay Science*, 208, 2021, 106111.
9. B. Li, M. H. Parekh, T. E. Adams, J. Fleetwood, V. G. Pol, V. Tomar, "In-situ Examination of Electrode Temperature during Overcharge and Thermal Runway of High Capacity Pouch Cell", Energy Technology (*In Production*)

Submitted

10. A.R. Shekhar, M.H. Parekh*, V.G. Pol*, "Worldwide Ubiquitous Utilization of Lithium-ion Batteries: What we have Done, are Doing and could Do Safely once they Die?"
11. M. H. Parekh, M. Palanisamy, V. G. Pol, "Reserve Lithium-ion Batteries: Deciphering in situ lithiation of Lithium-ion free Vanadium Pentoxide Cathode with Graphitic Anode"

In Preparation

12. M.H. Parekh, D.A. Jokhakar, V.P. Parikh, M. Palanisamy, V.G. Pol, "Lithium-Sulfur Batteries for Extreme Conditions."

13. M.H.Parekh, S. Oka, J. Lutekhaus, V.G. Pol, “Critical-point Dried, Porous and Safer Aramid Nanofiber Separator for High-Performance Durable Lithium-ion Batteries”
14. H. Rao, M.H. Parekh, D. Jokhakar, V.G. Pol, “Heteroatoms Embedded Carbon Anode for Sodium-ion Batteries at Elevated Temperature”
15. J. Li, M.H. Parekh, D. Puthuserri, V.G. Pol, S. Kenneth, “Silicon-Carbon Composite Anodes using Papilionoidea’s Neuroptera Templates”
16. C. Fear, Z. Hanwei, M.H. Parekh, J. Fleetwood, V.G. Pol, P. Mukherjee, “Elucidation of different separator systems via Accelerated Rate Calorimetry.”

A * signifies corresponding author